THERMOPLASTIC ADDITIVE MANUFACTURING FOR COMPOSITES AND MOLDS

A Dissertation Presented for the

Doctor of Philosophy

Degree

The University of Tennessee Knoxville

Pritesh S. Yeole

December 2020

DEDICATION

I dedicate my dissertation work to my professors and friends who made this journey unforgettable. A special feeling of gratitude to my loving parents Sudhakar Yeole and Asha Yeole for their unconditional love, and motivation. To my beloved wife, Jayshree, for her support and encouragement. I am very grateful to my brother, Prashant Yeole and sister, Snehal Nerkar, for their comfort.

ACKONWLEDGEMENTS

First and foremost, I would like to express my sincere and heartfelt gratitude to Dr. Uday Vaidya for his guidance, advice, encouragement and patience throughout my time at University of Alabama Birmingham and University of Tennessee Knoxville. Prof. Vaidya supported me in dissertation and helped me to develop personally and professionally. Further, I would like to thank for my co-mentor, Dr. Ahmed Hassen, for his valuable guidance these years. Working with him on several projects helped me to grow as a researcher. I am very thankful to my committee members Dr. Chad Duty and Dr. Claudia Rawn for their valuable insights and suggestions.

Next, I would like to thank Vlastimil Kunc, Seokpum Kim, John Lindahl, Vipin Singh, Tyler Smith and David Nuttall from Manufacturing Demonstration Facility, ORNL for all the help provided in additive manufacturing. I would also like to thank Alan Franc from Techmer PM, LLC and Robert Stratton from Stratton Composites for helpful discussions and feedback on CF-PPS pellets and CF-BMI prepreg, respectively.

This dissertation would not have been possible without the help and support of the members of the Fibers and Composites Manufacturing Facility, UTK. Special thanks to Stephen Sheriff and Vanina Ghossein for all the administrative support. I am very thankful for all the past and present graduate students and friends, especially: Hicham Ghossein, Shailesh Alwekar, Vidya Hiremath, Nitilaksha Hiremath, Ryan Spencer, Krishnan Veluswamy, Alex Stiles, David McConnell, Surbhi Kore, Kaustubh Mungale, Jared Hughes, Saurabh Pethe, Clayton Maner, Joe Gausphol, Mohammed Zahid for all the helpful discussions during the PhD tenure. I also appreciate all the help in sample preparation and characterization from Cliffton Herring, Jonathan Bigelow, Brandon Haggerty, Daniel Colborn.

I gratefully acknowledge U.S. Department of Energy, Office of Energy Efficiency and Renewable Energy, IACMI- The Composites Institute, Manufacturing Demonstration Facility for sponsoring my research thesis.

Finally, I am very thankful to the Almighty for providing me the strength and encouragement.

ABSTRACT

Recent inventions in the ability of additive manufacturing (AM) to use carbon fiber (CF) reinforced pellets as a feedstock material to manufacture components has complemented its purpose from prototypes to structural load-bearing parts. In the first part of this research, we investigated the processability, microstructure, and mechanical performance of twin-screw compounded short CF reinforced polyphenylene sulfide (PPS) pellets as a feedstock material for extrusion deposition fabrication-additive manufacturing (EDF-AM) using big area AM (BAAM). The performance of the BAAM components was compared to that of traditional processing methods, namely injection molding (IM) and extrusion-compression molding (ECM). It was found that the AM composites exhibited 118% lower tensile strength and 55% lower tensile modulus when compared to traditional injection molding composite specimens; however, AM composites exhibited comparable properties to ECM composites.

In BAAM, CFs are usually aligned along the deposition direction, which result in anisotropic thermal properties as heat transfer and warpage. In this study, three male molds with different infill patterns were produced via the EDF-AM process. These include (a) 0°: infill pattern along the printing direction; (b) 90°: infill pattern perpendicular to the printing direction; (c) 0°/90°: alternate layers along and perpendicular directions. It was observed that the thermal conductivity had a direct relationship with the CF orientation, as the average top surface temperature for 0° > 0°/90° > 90° and inverse relation with warpage.

The third part of this work focuses on improvement of durability of AM composite molds. A new material system called hybrid tooling was developed, such that a thin layer of Invar working surface and composite supporting structure. The high cost and density of Invar makes it a challenging material for tooling applications. Therefore, in this research, a mold substrate of CF-

PPS was prepared using AM, and a 0.1 mm layer of CF-BMI prepreg was attached as a skin layer. Durability of the mold was demonstrated from manufacturing seven (7) carbon fiber- epoxy hand lay-up parts using the mold. Also, it was observed that the mold held vacuum very precisely and no air leakage was observed.

Keywords: Extrusion deposition fabrication-additive manufacturing (EDF-AM), big area additive manufacturing (BAAM), X-ray photoelectron spectroscopy (XPS), porosity, mechanical characterization, tooling, extrusion compression molding (ECM), finite element analysis (FEA), 3D scanning, Geomagic control-X software.

TABLE OF CONTENTS

1 CHAPTER 1

1.1 MOTIVATION 2

1.2 DISCONTINUOUS FIBER COMPOSITES (DFCs) 4

1.3 PROCESSING METHODOLOGY FOR DFCs 8

1.4 RESEARCH OBJECTIVES 16

2 CHAPTER 22

2.1 INTRODUCTION 24

2.2 EXPERIMENTAL 28

2.2.1 Materials and Processing 28

2.2.2 Testing and Analysis 29

2.3 RESULTS AND DISCUSSION 33

2.3.1 Spectroscopic Analysis 33

2.3.2 Thermal Analysis 37

2.3.3 Porosity Measurement 42

2.3.4 Mechanical and Microscopic Analysis 47

2.4 CONCLUSIONS 54

3 CHAPTER 60

3.1 Introduction 62

3.2 Materials and Sample Preparation 64

3.3 Experimental Setup 69

3.4 Results and Discussion 72

3.4.1 Mechanical Tests: 72

3.4.1 Heat conduction and warpage: 72

3.5 Extrusion Compression Molding (ECM) with the 0°/90° infill mold 80

3.5.1 Mold Mounting: 80

3.5.2 Parts Fabrication: 82

3.5.3 Mold Degradation: 84

3.6 FINITE ELEMENT ANALYSIS (FEA) 87

3.7 Conclusions: 94

4 CHAPTER 101

4.1 INTRODUCTION 103

4.2 MATERIALS AND METHODS 105

4.3 RESULTS AND DISCUSSIONS 107

4.4 CONTACT ANGLE 109

4.5 *Phase II Studies* - PROCESS OPTIMZATION TO IMPROVE BONDING BETWEEN CF-BMI AND 50CF-PPS 113

4.6 AUTOCLAVE BONDING TRIALS 120

4.7 MOLD DEGRADATION EVALUATION 123

4.8 COST ANALYSIS 127

4.9 SUMMARY 129

VITA 135

LIST OF TABLES

Table 1.1: CTE and density of various materials [5, 6] 3

Table 2.1: Number of test specimens and dimensions 32

Table 2.2: FLD of Pellets, EDF-AM, ECM, and IM 43

Table 2.3: Mechanical properties of EDF-AM, ECM, and IM 49

Table 3.1: Tensile properties of 50CF-PPS at room temperature and high-temperature (100 °C and 180 °C) 74

Table 3.2: Average top mold surface temperature and total average deflection for different infill patterns. 74

Table 3.3: Coefficients used in the thermal simulation [40] 89

Table 4.1: Mechanical test data for baseline specimens 111

Table 4.2: Summary of transverse tensile strength of 50CF-PPS and CF-BMI bonding optimization trials 119

Table 4.3: Cost breakdown of hybrid 50CF-PPS and CF-BMI mold 128

LIST OF FIGURES

Figure 1.1: Classification of TRC based on the fiber length – continuous and chopped, intermediate forms and techniques for fabrication of finished products. 5

Figure 1.2: (a) The change of tensile stress and interfacial shear stress with respect to fiber aspect ratio ($\boldsymbol{ld}$) (b) Dependence of composite mechanical properties and processability based on its fiber length. The composite materials having length less than 12.7 mm (0.5”) are considered as DFCs. (adapted from [13]) 7

Figure 1.3: Schematic of the IM process. Pellets inserted through feed section are melted along the progress in the screw and injected in the closed mold through nozzle under high pressure. 9

Figure 1.4: Schematic of the ECM process. Pellets inserted in the extruder to obtain a charge. Charge then transferred to the mold and part is created under pressure. 11

Figure 1.5: Schematic of AM process. Pellets undergoes through extrusion screw and nozzle to create bead and parts are fabricated by depositing layers/beads in Z-direction. 12

Figure 1.6: BAAM set up (working area: 6 m × 2.4 m × 1.8 m), Manufacturing Demonstration Facility, ORNL. The extrusion screw is mounted on a gantry system. (a) extruder screw (b) nozzle. Photo Courtesy of ORNL, US Department of Energy. 14

Figure 1.7: Single screw polymer extrusion deposition head of BAAM [35]. Screw has four heating zones to melt the pellets. Pellets undergoes from different sections as feed, transition and metering before coming out from extruder. 15

Figure 2.1: Chemical structure of PPS [18] 26

Figure 2.2: Schematic for testing coupons directions; (a) EDF-AM hexagon edge (304.8 × 304.8 mm²). Bead: Each successive layer deposited by the extruder, and (b) ECM plaque (152.4 × 152.4 mm²). Charge: Location of the charge placed in the mold 31

Figure 2.3: Samples locations for FLD calculations; (a) ECM, and (b) IM 35

Figure 2.4: XPS Spectra of; (1) Fiber Surface: (a) Overall Spectra, (b) C1s, (c) O1s; and..... 36

Figure 2.5: XPS Spectra CF-PPS Composite; (a) Overall spectra, and (b) C1s..... 38

Figure 2.6: Overlapping spectra for CF and CF-PPS; (a) C 1s, and (b) O 1s..... 39

Figure 2.7: Thermal analysis results; (a) DSC of 50CF-PPS pellets: heat-cool-heat cycle from room temperature to 350 °C, and (b) TGA analysis of PPS matrix and 50CF-PPS pellets in oxidative conditions from room temperature to 800 °C 41

Figure 2.8: Probability distribution of CF length (a) Pellets (b) AM (c) ECM (d) IM..... 44

Figure 2.9: Illustration of macro-void formation during the AM process. 45

Figure 2.10: (a) X-CT image of FDE-AM specimen (b) Relative frequency distribution as a function of equivalent diameter of void. EFD-AM contain a total of 15.5 volume % voids. 46

Figure 2.11: (a) X-CT image of ECM specimen. All pores in ECM are present in the top and bottom surface only and contain a total of 4.30 volume % voids. (b) X-CT image of IM specimen. IM contain a total of 0.007 volume % voids..... 48

Figure 2.12: Mechanicle properties for EDF-AM, ECM and IM; (a) Tensile strength versus tensile modulus, and (b) Flexure strength versus flexure modulus 50

Figure 2.13: SEM micrographs of a fracture surface of tensile specimen; (a) EDF-AM: Most of the fibers are aligned in printing direction, also contain voids; (b) ECM: Fibers are well

distributed in all directions and (c) IM: Fibers are well aligned in flow directions. All samples showed fiber pullout..... 52

Figure 3.1: Schematic of AM extruder with fiber orientation profile inside the deposited bead. Fibers are aligned along the edge while randomly oriented inside the bead [22]..... 65

Figure 3.2: Design of 50CF-PPS printed dome-shaped mold (a) Male mold (b) Female mold. The molds were printed using BAAM with bead width 13.97 mm (0.55”), and bead height: 5.08 mm (0.2”)..... 67

Figure 3.3: Infill pattern (a) 0° (b) 90° (c) 0°/90°. The bead width: 13.97 mm (0.55”) and bead height: 5.08 mm (0.2”)..... 68

Figure 3.4: Hexagon with 304.8 mm x 304.8 mm x 22 mm dimension. X-direction: along the bead deposition, Z-direction: transverse to the bead deposition..... 70

Figure 3.5: Mold placed on the platen (200 °C) and heated through conduction for 5 hours. Position of thermocouples (position 1 to 10) represent the locations where the temperature was recorded. 71

Figure 3.6: Tensile behavior of 50CF-PPS samples with increase in temperature (a) tensile modulus (b) tensile strength..... 73

Figure 3.7: Aligned image of mold at room temperature and elevated temperature. All three molds showed similar pattern as warped along the Z-direction. Amount of warpage was different for each mold..... 77

Figure 3.8: 3D deviation analysis of molds at room temperature and after keeping on heated (200 °C) platen for 5 hours. Total average deflection for (a) 0°: 0.314 mm; (b) 90°: 0.363 mm; (c) 0°/90°: 0.329 mm 79

Figure 3.9: Failure mechanism of AM specimens under compression loading (a) Vertical direction (0°); (b) Horizontal direction (90°) (adapted from [33]) 81

Figure 3.10: Failure (crack) in the 50CF-PPS additive manufactured mold due to application of pressure on heated warped mold (a) Male mold (b) Female mold 83

Figure 3.11: (a) Location of charge placed in the BAAM printed mold (b) the representative consolidated part of 40CF-PA6. The unfilled region on the consolidated part due to the limitation of the plasticator to generate a bigger charge (Maximum charge length produced by plasticator was 304.8 mm). 85

Figure 3.12: Deviation analysis of the two scans before and after 20 parts fabrications. Maximum deformation was observed at the 1096 epoxy region (blue area). 86

Figure 3.13: Boundary conditions for service load simulation (thermal simulation). Bottom temperature: 160 °C and ambient temperature: 30°C. 90

Figure 3.14: Temperature profile of the top surface of the three molds. (a) Mold with 0° infill, (b) Mold with 90° infill, (c) Mold with 0°/90° infill 92

Figure 3.15: Surface of interest/part molding area (shaded area) and the location of peak temperature (purple circle). Average surface temperature for each mold was measured in the shaded area. 93

Figure 3.16: Temperature profile of the top surface of 50CF-PPS AM mold (a) 3 perimeters (b) 1 perimeter 95

Figure 4.1: 50CF-PPS: 355.6 mm × 355.6 mm × 203.2 mm (14” × 14” × 8”) mold substrate, printed with the BAAM system with 0/90 infill pattern. Printing parameters:- bead width: 13.97 mm, bead height: 5.08 mm. 106

Figure 4.2: (a) Flat 50CF-PPS BAAM plaque, (b) CF-BMI prepreg bonded on the 50CF-PPS substrate using hydraulic compression press (model number: 3895.41E1000). Processing conditions: temperature – 190 °C, pressure – 552 kPa, dwell time – 2 hours. 108

Figure 4.3: Failed baseline specimen of 50CF-PPS and CF-BMI flat plaque (a) Through thickness transverse tensile test - resin did not flow inside the gaps between the beads, (b) Fracture toughness - failure started at the intersection between AM and prepreg; however, propagated through AM Z-interlayers. 110

Figure 4.4: Dynamic contact angle measurement set up (adapted from [24]). The specimen immersed (5 mm) into the liquid (water) with constant speed (20 µm/s). The proceeding and receding contact angles were recorded using control system. 114

Figure 4.5: Dynamic contact angle plots of CF-BMI prepreg with respect to immersion depth (advancing angle: 95°, receding angle: 63°) and 50CF-PPS (advancing angle: 80°, receding angle: 42°). 115

Figure 4.6: Optical microscopic images of failed transverse tensile test specimens (a) increased temperature: BMI resin flowed inside the beads (b) dry epoxy: 0.1 mm thick layer of 1096 epoxy (c) wet epoxy-no filler: 1096 epoxy resin squeezed out from top of the bead due to 552 kPa pressure (d) wet epoxy-micro-balloon fillers: 1096 epoxy did not squeezed out due to increased viscosity 118

Figure 4.7: Step – 1: 50CF-PPS BAAM substrate; Step – 2: Thin layer (0.1 mm) of 1096 epoxy + 40% micro-balloon applied on substrate; Step – 3: Draping of CF-BMI prepreg on the substrate molding area and sides; Step – 4: Hybrid structure (AM substrate and prepreg) vacuum bagged; Step – 5: Mold plumbed and placed in the autoclave (processing conditions – 190 °C temperature, 552 kPa pressure for 2 hours) 121

Figure 4.8: Hybrid mold with CF-BMI prepreg after the autoclave trial. The CF-BMI prepreg showed proper draping without any wrinkles. However, the top curvature surface had print through of the beads from the 50CF-PPS BAAM substrate. 122

Figure 4.9: (a) Schematic of the Hand Lay-up process (b) Representative consolidated CF-huntsman epoxy part 124

Figure 4.10: Degradation analysis of CF-BMI mold surface after fabrication of 7 hand lay-up parts 126

1 CHAPTER

INTRODUCTION

1.1 MOTIVATION

Additive manufacturing (AM) is a process capable of creating a wide range of complex geometries from a 3-dimensional (3D) computer-aided design (CAD) model. The technology was developed in the 1980s and mainly used by designers and architects for prototyping due to its rapid and cost-effective capability. However, recent developments have contributed to increasing the mechanical performance of printed components. Therefore, it has been utilized to fabricate finished load bearing and/or functional parts. Wohler et al. predicted that about 50% of commercial products would involve AM by 2020 [1].

In the last decade alone, more than one-third of the tool and die companies have gone out of business as the US manufacturers have started producing molds overseas [2]. AM provides potential advantages over traditional tool manufacturing [3] because of several factors, such as (i) Lead time reduction: fabrication of tooling by AM can lead to 40-90 percent time saving due to fewer labor inputs, machining steps, use of digital design files, rather than 2D drawings and in-house tooling; (ii) Cost reduction: AM for tooling helps cost reduction due to decrease in material lost during fabrication, improving product yield and reducing labor inputs. (iii) Improved functionality: AM allows the manufacturing of previously unobtainable and/or unaffordable tool designs (due to complex shapes). (iv) Increased ability to customize.

The key reason to consider composite tooling is the similarity in coefficient of thermal expansion (CTE) between the composite part and the composite tool. The difference in thermal expansion has significant effect on the formation and distribution of the thermal skin-core residual stresses [4]. The CTE for composites is lower compared to CTE of metals, as shown in Table *1.1*. The composite material witnesses' thermal strains while processing under temperature and pressure in

Table 1.1: CTE and density of various materials [5, 6]

Sr. No.	Material	CTE (10^{-6} K^{-1})	Density (g/cc)
1	Steel	12	7.80
2	Aluminum	23	2.70
3	Unidirectional CF-PPS in the longitudinal fiber direction	0.56	1.44
4	Invar	1.6	8.10

metal tool(s). Therefore, it can be concluded that the mismatch of CTE between the part and tool can lead to thermal stresses, part distortion, and spring-back behavior. Only Invar metal alloy has CTE (1.6×10^{-6} K^{-1}) similar to CF composites; however, Invar is very expensive and difficult to handle due to its heavy weight (Invar density: 8.10 g/cc) [5].

1.2 DISCONTINUOUS FIBER COMPOSITES (DFCs)

The need for strong, lightweight materials for aerospace, automobile, marine, and military applications has shown considerable growth in fiber-reinforced composites (FRCs) [7, 8]. Thermoplastic reinforced composites (TRCs) offer numerous advantages such as specific strength and modulus, rapid cycle times, and longer shelf life [9]. The TRC market is proliferating and expected to reach USD 36 billion by 2024, at a 5.2% compound annual growth rate (CAGR) [10]. The overall properties of TRCs are influenced by resin system, fiber type, fiber percentage, fiber orientation, and fiber aspect ratio (i.e., length/diameter). TRCs are mainly classified as continuous reinforcement and discontinuous reinforcement based on fiber length. Fibers are the primary load-carrying constituent in the composite. Figure 1.1 shows the classification of various types of composite forms in TRC. The continuous fiber composites offer excellent mechanical performance; however, they are anisotropic in nature, expensive to produce, and hard to mold into complex-shaped parts. Discontinuous fiber composites (DFCs) can be processed using traditional plastic molding equipment and can obtain up to 90% properties of continuous counterparts [11].

The FRC material consists of high strength and modulus fibers embedded in a matrix with a distinct interface. FRCs are microscopically inhomogeneous and orthotropic [12]. Therefore, the mechanics of FRC is more complicated than conventional materials. When a tensile load is applied to the composite material, the applied stress on the matrix transfers to the fiber through an interface,

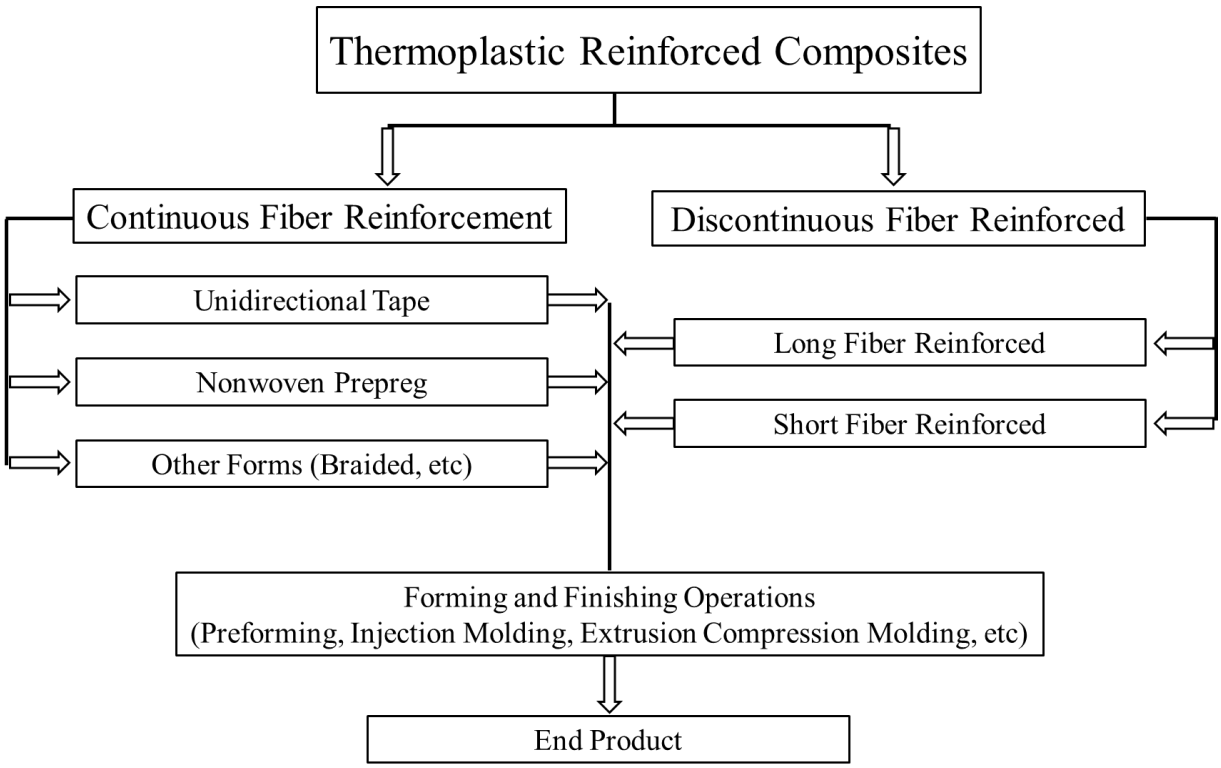

Figure 1.1: Classification of TRC based on the fiber length – continuous and chopped, intermediate forms and techniques for fabrication of finished products.

assuming perfect bonding between the fiber and polymer. Figure 1.2 illustrates the tensile and shear stress distribution along the length of a single fiber. For DFCs, the tensile stress in the fiber and shear stress at the interface is not consistent in all regions due to different elastic properties of fibers and polymers [12, 13]. Tensile stress is zero at the fiber ends and increases along the fiber length and ultimately reaches a maximum at the center, while shear stress is maximum at the fiber ends and reduces along the fiber length to almost zero at the center [12]. The strength and stiffness properties of DFCs depend on the critical length of the fiber [14]. Critical fiber length is the minimum fiber length required for the maximum fiber stress to be equal to the ultimate tensile strength of the fiber at mid-length. For a given fiber diameter, tensile stress on fiber, and fiber-matrix interfacial shear strength, a critical fiber length is calculated based on Equation 1 [15].

$$l_c = \frac{\sigma_{fu}}{2\tau_i} d_f \qquad \text{Equation 1}$$

where,

σ_{fu} – ultimate tensile strength of fiber

τ_i – interfacial shear strength

d_f – fiber diameter

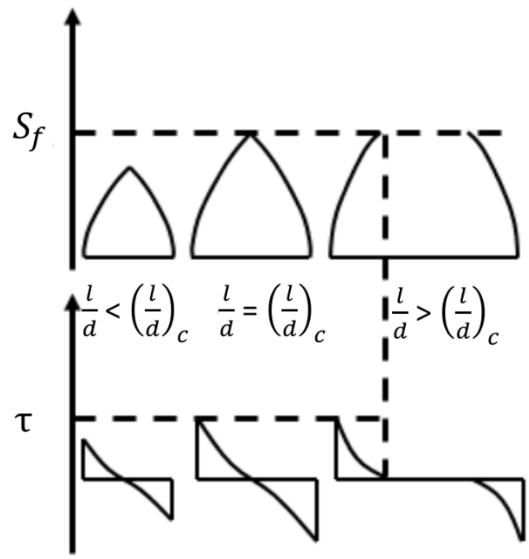

(a)

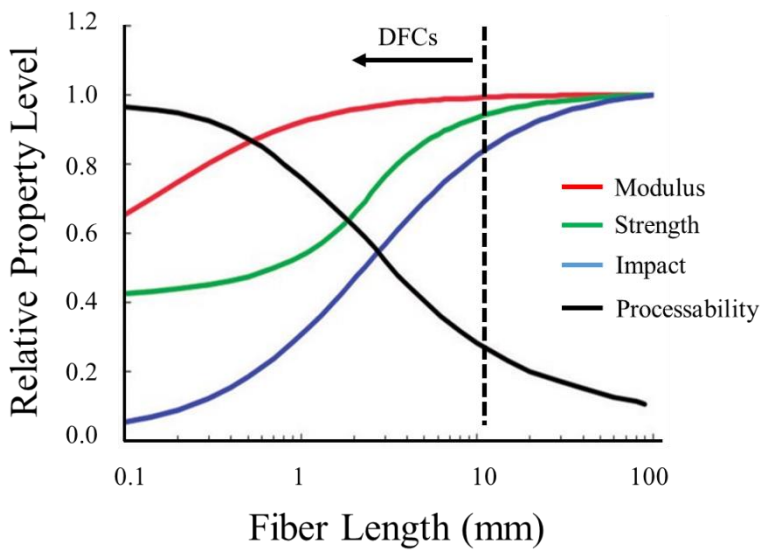

(b)

Figure 1.2: (a) The change of tensile stress and interfacial shear stress with respect to fiber aspect ratio (l/d) (b) Dependence of composite mechanical properties and processability based on its fiber length. The composite materials having length less than 12.7 mm (0.5") are considered as DFCs. (adapted from [13])

DFCs can be divided into two groups, long fiber thermoplastics (LFTs) and short fiber thermoplastics (SFTs) based on the fiber length. LFTs are a group of composite materials that include fibers of 12.7 mm – 38.1 mm (0.5” to 1.5”) length reinforced into a variety of crystalline and amorphous thermoplastic polymers. The fiber aspect ratio (l/d) distinguishes long fibers from short fibers (i.e. 0.2 mm – 10.16 mm (0.008” -0.4”)). Short fiber reinforced polymers (SFRP) are attractive because of easy fabrication and moderately improved mechanical properties over unreinforced polymers at a negligible incremental cost [16-19]. Furthermore, short fibers are more effective to improve friction and wear resistance than their continuous fiber counterparts [20]. The mechanical properties of SFRPs critically depend on the combination of fiber length distribution (FLD) and fiber orientation distribution (FOD) in composite parts [16, 17]. During any manufacturing process, fiber breakage takes place because of the interactions between fiber-polymer, fiber-fiber, fiber-equipment surface resulting in reducing fiber aspect ratio [21, 22]. Therefore, final fiber length, fiber orientation, void content of a final composite part varies according to the processing conditions, type of matrix, and/or fiber and volume fraction, which collectively influence the mechanical (and other) properties.

1.3 PROCESSING METHODOLOGY FOR DFCs

There are various techniques available to manufacture parts using chopped thermoplastic composites, i.e., extrusion compression molding, injection molding, and additive manufacturing.

Injection Molding (IM) is generally used for the processing of unreinforced polymers and SFTs, as longer fibers (> 0.5”) can clog the nozzle [19]. Manufacturing of parts using IM consist of five steps- (i) softening/melting of the material, (ii) injecting the molten material under pressure into the closed mold, (iii) maintain pressure in the mold to prevent the backflow of material, (iv) cooling

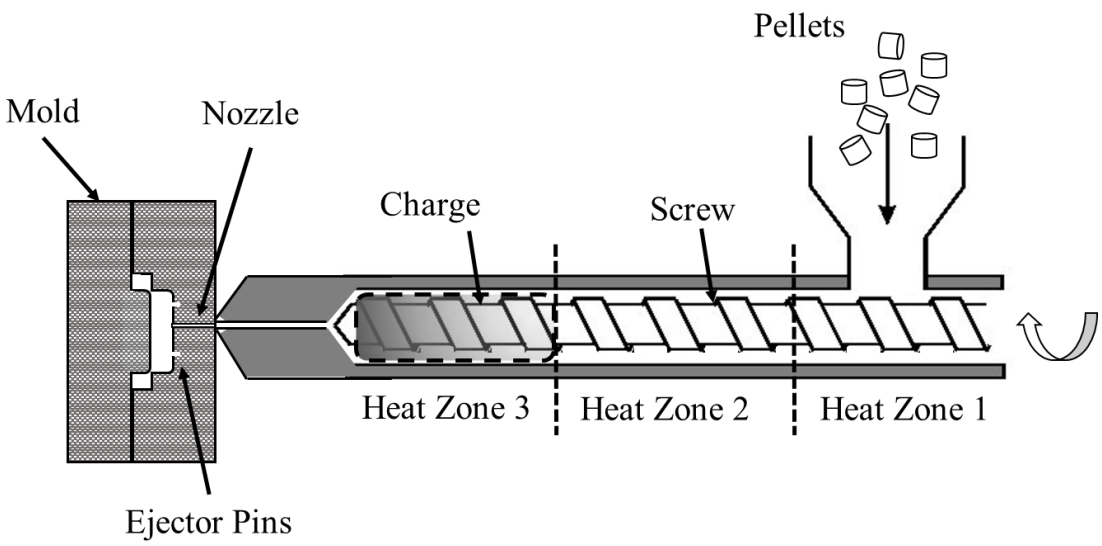

Figure 1.3: Schematic of the IM process. Pellets inserted through feed section are melted along the progress in the screw and injected in the closed mold through nozzle under high pressure.

of the molded part until it is rigid/solidified, and (v) remove the part from mold by ejection pins [23]. More details about the IM method can be found in [24-27]. The IM process is shown in Figure 1.3.

Extrusion Compression Molding (ECM) process is used for manufacturing of materials in pellet form **(**unreinforced, SFTs, LFTs). ECM process is a combination of two basic operations, namely extrusion and compression molding. The pellets are fed into the low shear extruder (plasticator) where the temperature of the plasticator is maintained above the melting point of the polymer, and a 'charge' is produced. The hot, molten charge is then transferred to the mold mounted in a fast-acting compression press. The closing of the press results in the flow of the charge within the mold cavity, to obtain the desired shape. The part is then removed from the mold after the material is subjected to determined 'dwell time' under pressure prior to its removal. Figure 1.4 illustrates the ECM process cycle. It is to be noted that the extruder used in this process is a low shear, which helps to retain maximum fiber length, ultimately resulting in maximum mechanical properties in the finished product [28].

Additive Manufacturing (AM) is a process of creating objects from the 3D model by depositing polymer-composite extrudate layer-by-layer [29], as shown in Figure 1.5. The main advantages of AM over traditional manufacturing are the shorter lead time, reduction in cost, ability to customize complex parts without expensive tooling, and localized production [30]. AM uses a wide variety of materials such as metals, ceramics, polymers (neat and fiber reinforced). The use of polymers in AM has been widely investigated for a variety of applications due to its ease of processing, and relatively low manufacturing cost [31].

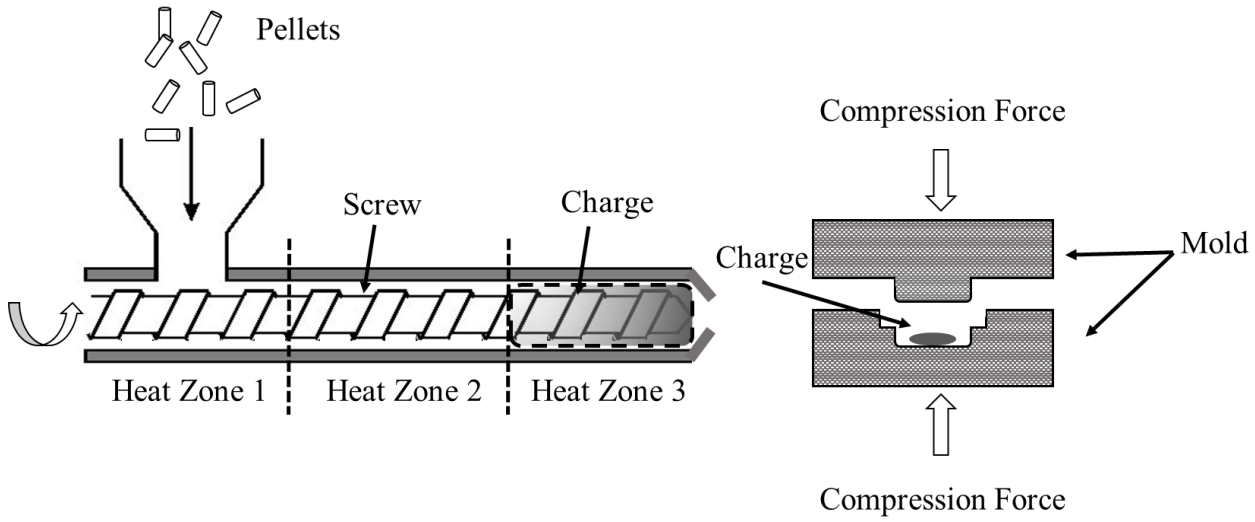

Figure 1.4: Schematic of the ECM process. Pellets inserted in the extruder to obtain a charge. Charge then transferred to the mold and part is created under pressure.

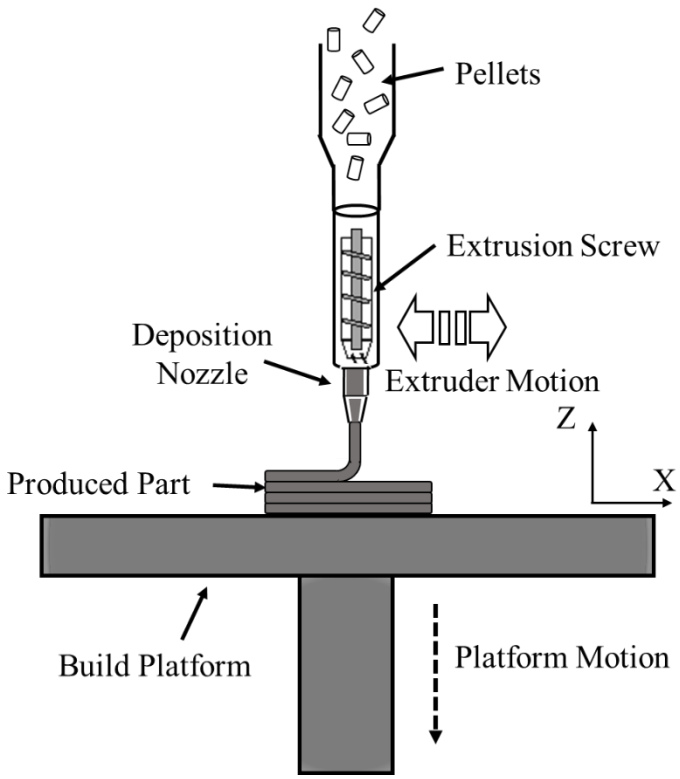

Figure 1.5: Schematic of AM process. Pellets undergoes through extrusion screw and nozzle to create bead and parts are fabricated by depositing layers/beads in Z-direction.

Extrusion Deposition Fabrication-Additive Manufacturing (EDF-AM), also referred to as fused deposition modeling (FDM) or fused filament fabrication (FFF)**,** is the most widely used AM process for engineering plastics and composites [32-34].

The growth in AM over the last two decades has made great strides in the development of composite tooling; however, there are barriers such as low print speed and less developed materials for AM in terms of mechanical and thermal properties. Recent developments in polymer extrusion deposition have helped expand the use of composites in mold production. Cincinnati Incorporated (CI) and Oak Ridge National Laboratory (ORNL) have created a large-scale big area additive manufacturing (BAAM) system (6 m × 2.4 m × 1.8 m) (Figure 1.6) to manufacture AM parts which can deposit material at a rate of 50 kg/hr. The BAAM uses a single screw extruder mounted on a gantry system. The schematic of the BAAM screw design is given in Figure 1.7 [35]. The feedstock materials for BAAM are pellets (instead of wires/filaments), similar to that used in injection molding [36, 37]. This broadens the supply chain of available materials for BAAM and significantly reduces the cost of feed material in comparison to filaments. The pellets are dried before they are fed to the extruder. The BAAM extruder rotates in a barrel, which has four heating zones to melt the polymer. The resulting physical states of the pellets migrate through different sections of the screw, i.e. from the feed section to transition section. The molten material is then transferred to the metering section and is forced out of the screw through the deposition nozzle under pressure. The large-scale parts are fabricated by depositing material on a heated bed. The components made from BAAM find applications in aerospace, automotive, energy, and tooling.

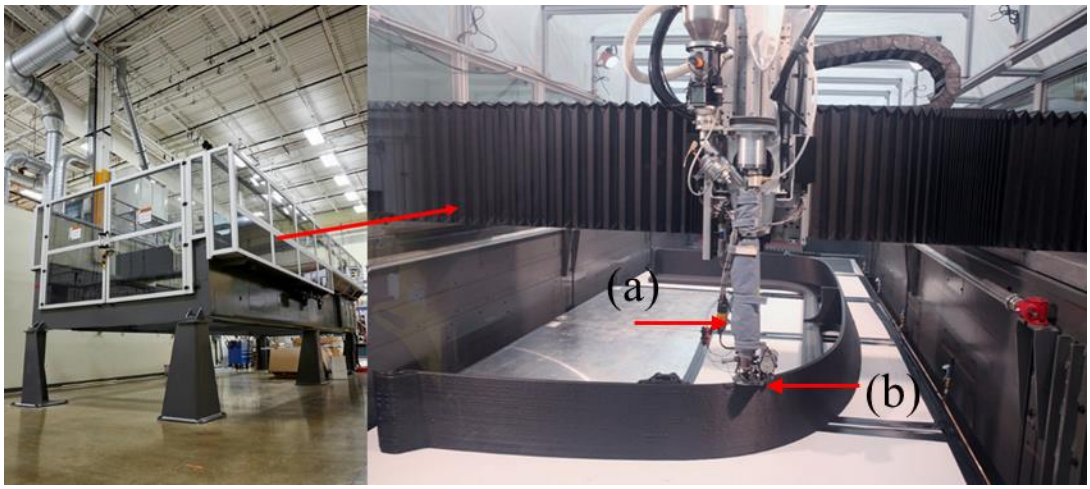

Figure 1.6: BAAM set up (working area: 6 m × 2.4 m × 1.8 m), Manufacturing Demonstration Facility, ORNL. The extrusion screw is mounted on a gantry system. (a) extruder screw (b) nozzle. Photo Courtesy of ORNL, US Department of Energy.

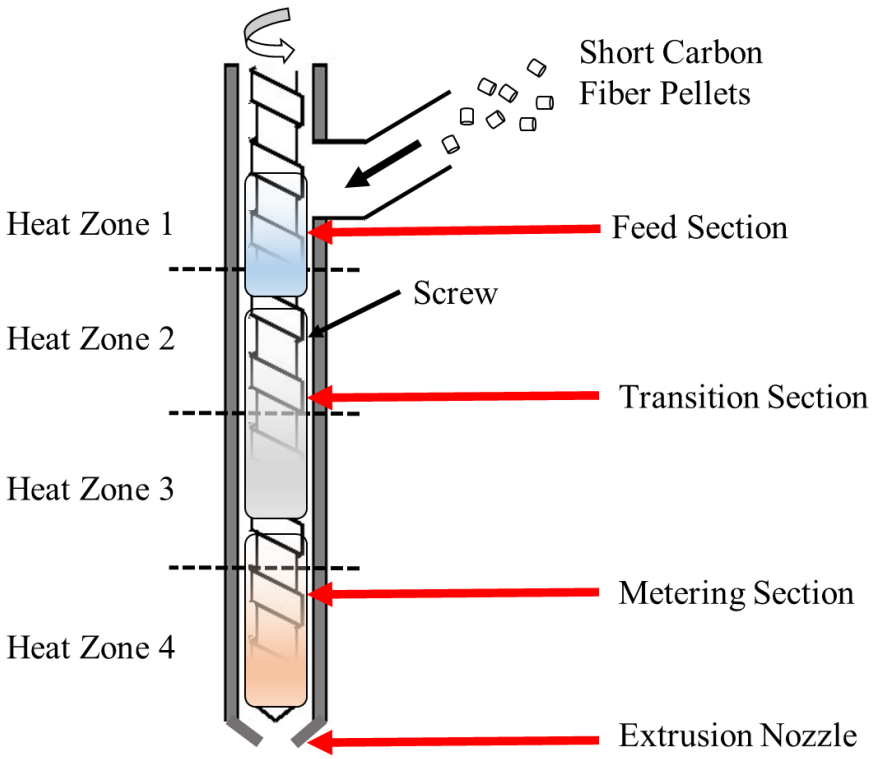

Figure 1.7: Single screw polymer extrusion deposition head of BAAM [35]. Screw has four heating zones to melt the pellets. Pellets undergoes from different sections as feed, transition and metering before coming out from extruder.

1.4 RESEARCH OBJECTIVES

The work has been divided in three objectives.

OBJECTIVE 1: INVESTIGATE THE EDF-AM PROCESS TO COMPARE TO TRADITIONAL ECM AND IM PROCESS

Recent inventions in the ability of AM to use carbon fiber (CF) reinforced pellets as a feedstock to manufacture components has changed its purpose from prototypes to structural load-bearing parts. However, compared to traditional manufacturing techniques, the mechanical properties of AM materials and their resulting components are not well understood. This work characterized the twin-screw compounded short CF-PPS pellets as feedstock material for EDF-AM. Spectroscopic and thermal characterization were performed on these pellets to understand the bonding and thermal properties. The mechanical behavior of CF-PPS for extrusion deposition BAAM was compared with traditional processing methods, namely- IM and ECM.

OBJECTIVE 2: OPTIMIZING THE INFILL PATTERN OF ADDITIVELY MANUFACTURED COMPRESSION MOLDS

In this objective, attention of the research progress towards structural application (tooling) of EDF-AM process. AM offers potential advantages over traditional tool manufacturing processes because of lead time and cost reduction, improved functionality, and increased ability to customize parts. The work investigates the anisotropic thermal behavior of CF for additively manufactured molds for high-temperature applications (heating up to 100 °C). Fabricated molds with different infill patterns using the EDF-AM process to understand the effect of CF orientation on thermal conductivity and deflection (warpage) of the mold. A FEA model was used to generate the toolpath (deposition path) with various print orientations, and the orientation of local material properties were imported directly to a thermal simulation powered by Abaqus 2018.

OBJECTIVE 3: IMPROVE DURABILITY AND SURFACE QUALITY OF ADDITIVELY MANUFACTURED MOLDS USING CARBON FIBER-BISMALEIMIDE (CF-BMI) PREPREG

A hybrid tool features a skin which provide desired surface quality, durability and a low-density substrate to reduce weight of the mold. This work focusses on the alternate hybrid tool system for the autoclave process. Manufactured a hybrid mold as CF-PPS substrate using the EDF-AM process and a thin layer of CF-BMI prepreg as a skin. Investigated, optimized, and evaluated various techniques to improve the bonding and compatibility between AM surface and prepreg skin. Studied the surface degradation of hybrid mold (CF-BMI molding surface) by fabricating parts using hand lay-up process.

REFERENCES

1. Ngo, T.D., et al., *Additive manufacturing (3D printing): A review of materials, methods, applications and challenges.* 2018. **143**: p. 172-196.
2. Canis, B. *The tool and die industry: Contribution to US manufacturing and federal policy considerations*. in *CRS Report for congress*. 2012.
3. Cotteleer, M., M. Neier, and J.J.D.R. Crane, *3D opportunity in tooling: Additive manufacturing shapes the future.* 2014.
4. Parlevliet, P.P., H.E. Bersee, and A. Beukers, *Residual stresses in thermoplastic composites—A study of the literature—Part I: Formation of residual stresses.* Composites Part A: Applied Science and Manufacturing, 2006. **37**(11): p. 1847-1857.
5. Chung, D.J.A.t.e., *Materials for thermal conduction.* 2001. **21**(16): p. 1593-1605.
6. Premkumar, M., W. Hunt, and R.J.J. Sawtell, *Aluminum composite materials for multichip modules.* 1992. **44**(7): p. 24-28.
7. Carrillo, J., et al., *Ballistic performance of thermoplastic composite laminates made from aramid woven fabric and polypropylene matrix.* 2012. **31**(4): p. 512-519.
8. Ning, H., et al., *Design and development of thermoplastic composite roof door for mass transit bus.* 2009. **30**(4): p. 983-991.
9. Caba, A.C., *Characterization of carbon mat thermoplastic composites: flow and mechanical properties*. 2005, Virginia Tech.
10. Singh, S. *Thermoplastic Composites Market worth $36.0 billion by 2024*. 2019; Available from: https://www.marketsandmarkets.com/PressReleases/thermoplastic-composite.asp.
11. Vaidya, U., et al., *The process and microstructure modeling of long-fiber thermoplastic composites.* 2008. **60**(4): p. 43.

12. Mallick, P.K., *Fiber-reinforced composites: materials, manufacturing, and design*. 2007: CRC press.

13. Parthasarathy, K.B.T., *Processing and characterization of long fiber thermoplastics*. 2008: The University of Alabama at Birmingham.

14. Petersen, R.J.J.o.d.r., *Discontinuous fiber-reinforced composites above critical length.* 2005. **84**(4): p. 365-370.

15. Chawla, K.K., *Composite materials: science and engineering*. 2012: Springer Science & Business Media.

16. Tekinalp, H.L., et al., *Highly oriented carbon fiber–polymer composites via additive manufacturing.* 2014. **105**: p. 144-150.

17. Fu, S.-Y., et al., *Tensile properties of short-glass-fiber-and short-carbon-fiber-reinforced polypropylene composites.* 2000. **31**(10): p. 1117-1125.

18. Fu, S.-Y., B.J.C.S. Lauke, and Technology, *Effects of fiber length and fiber orientation distributions on the tensile strength of short-fiber-reinforced polymers.* 1996. **56**(10): p. 1179-1190.

19. Hassan, A., et al., *Tensile, impact and fiber length properties of injection-molded short and long glass fiber-reinforced polyamide 6, 6 composites.* 2004. **23**(9): p. 969-986.

20. Voss, H. and K.J.W.o.M. Friedrich, *The wear behavior of short-fiber reinforced thermoplastics sliding against smooth steel surfaces.* 1985: p. 742.

21. Bijsterbosch, H. and R.J.P.c. Gaymans, *Polyamide 6—long glass fiber injection moldings.* 1995. **16**(5): p. 363-369.

22. Denault, J., T. Vu-Khanh, and B.J.P.c. Foster, *Tensile properties of injection molded long fiber thermoplastic composites.* 1989. **10**(5): p. 313-321.

23. Rosato, D.V. and M.G. Rosato, *Injection molding handbook*. 2012: Springer Science & Business Media.

24. Thi, T.B.N., et al., *Measurement of fiber orientation distribution in injection-molded short-glass-fiber composites using X-ray computed tomography.* 2015. **219**: p. 1-9.

25. Tseng, H.-C., et al., *Numerical prediction of fiber orientation and mechanical performance for short/long glass and carbon fiber-reinforced composites.* 2017. **144**: p. 51-56.

26. Subasinghe, A., et al., *Fiber dispersion during compounding/injection molding of PP/kenaf composites: Flammability and mechanical properties.* 2015. **86**: p. 500-507.

27. Vaidya, U., *Composites for automotive, truck and mass transit: materials, design, manufacturing*. 2011: DEStech Publications, Inc.

28. Vaidya, U., et al., *Long fiber thermoplastic thin-walled aeroshells for missile applications and methods of manufacture*. 2018, Google Patents.

29. Cotteleer, M. and J.J.D.R. Joyce, *3D opportunity: Additive manufacturing paths to performance, innovation, and growth.* 2014. **14**: p. 5-19.

30. Wong, K.V. and A. Hernandez, *A review of additive manufacturing.* ISRN Mechanical Engineering, 2012. **2012**.

31. Prajapati, H., et al., *Improvement in build-direction thermal conductivity in extrusion-based polymer additive manufacturing through thermal annealing.* Additive Manufacturing, 2019. **26**: p. 242-249.

32. Favaloro, A.J., et al., *Simulation of polymeric composites additive manufacturing using Abaqus.* Science in the Age of Experience, 2017: p. 103-114.

33. Gardan, J., *Additive manufacturing technologies: state of the art and trends.* International Journal of Production Research, 2016. **54**(10): p. 3118-3132.

34. Araya-Calvo, M., et al., *Evaluation of compressive and flexural properties of continuous fiber fabrication additive manufacturing technology*. Additive Manufacturing, 2018. **22**: p. 157-164.

35. Chesser, P., et al., *Extrusion control for high quality printing on Big Area Additive Manufacturing (BAAM) systems.* 2019. **28**: p. 445-455.

36. Kishore, V., et al., *Additive manufacturing of high performance semicrystalline thermoplastics and their composites*. 2016, Oak Ridge National Lab.(ORNL), Oak Ridge, TN (United States).

37. Duty, C.E., et al., *Structure and mechanical behavior of Big Area Additive Manufacturing (BAAM) materials.* 2017. **23**(1): p. 181-189.

2 CHAPTER

MECHANICAL CHARACTERIZATION OF HIGH-TEMPERATURE CARBON FIBER-POLYPHENYLENE SULFIDE COMPOSITES FOR LARGE AREA EXTRUSION DEPOSITION ADDITIVE MANUFACTURING

ABSTRACT

Additive manufacturing (AM) is evolving from rapid prototyping to production of structural components. The widespread application of AM demands a high level of mechanical performance from these components, and it is therefore essential to improve feedstock material in order to meet these mechanical expectations. However, compared to traditional manufacturing techniques, the mechanical properties of AM materials and their resulting components are not well understood. In this study, we investigated the processability, microstructure, and mechanical performance of twin-screw compounded short carbon fiber reinforced polyphenylene sulfide (PPS) pellets as a feedstock material for AM. The performance of the AM components was compared to that of traditional processing methods, namely injection molding (IM) and extrusion-compression molding (ECM). It was found that the AM composites exhibited 118% lower tensile strength and 55% lower tensile modulus when compared to traditional injection molding composite specimens; however, AM composites exhibited comparable properties to ECM composites. This response was attributed to highly aligned fibers in IM and AM samples. However, the AM composites contained porosity (15.5% volume), which reduced their mechanical properties in comparison to ECM composites. The IM process showed the maximum amount of fiber attrition with minimum porosity (0.007% volume), while the ECM process exhibited the least fiber attrition with 4.3% volume porosity.

Keywords: Extrusion Deposition Modeling, Additive Manufacturing, Extrusion Compression Molding, Injection Molding, Mechanical characterization

2.1 INTRODUCTION

Fused Filament Fabrication (FFF) is a modern polymer additive manufacturing (AM) technique, in which a part can be manufactured based on a computer-aided design (CAD) [1]. Traditionally, the primary use for polymer AM has been in prototyping; however, a transition to functional load-bearing parts is possible if the mechanical properties of the parts can be improved [2]. In general, polymers have poor mechanical properties, but reinforcing polymers with carbon fiber (CF) provides strength and stiffness [3, 4]. For example, Love et al. [5] showed that AM parts using CF composites have less distortion than those produced with neat polymers because CF reduces the coefficient of thermal expansion and increases thermal conductivity. The high specific modulus and self-lubricating nature of CF help to lower the coefficient of friction and improve wear resistance [6].

There are several studies on the fabrication of fiber-reinforced composite parts using FFF. Zhong et al. [7] studied the processability of acrylonitrile butadiene styrene (ABS) composites reinforced with different contents of glass fiber and observed that glass fibers significantly improved the tensile strength, but compromised the flexibility of the ABS filament. Ning et al. [8] added CF (different lengths and contents) to ABS and investigated the effect on parts fabricated with FFF. They noted that 5% by weight (wt.) addition of CF increased tensile and flexure strength by 22.5% and 11.82%, respectively. Ning et al. also observed that the 150 µm length samples of CF resulted in higher strength and modulus as compared to the 100 µm CF samples. Shofner et al. [9] presented ABS reinforced with single-walled carbon nanotubes as an FFF feedstock and noted that, when neat ABS was loaded with 10% wt carbon nanotubes, an improvement of 40% tensile strength and 60% tensile modulus was realized. Tekinalp et al. [1] compared the tensile properties of composites manufactured by FFF and compression molding using CF-reinforced ABS. Their

results showed that, although fibers were highly oriented in the FFF specimens, tensile properties were lower compared to the compression-molded samples, due to a higher porosity in the FFF specimens.

The above investigations employed ABS as a matrix material. However, there is another material, polyphenylene sulfide (PPS), that has also been used in AM specifically when elevated temperature applications are needed. PPS is an engineering high-temperature thermoplastic polymer with a backbone of alternating aromatic rings and sulphur atoms, as shown in Figure 2.1. PPS represents an excellent combination of properties such as thermal stability, chemical, flame, and wear resistance, processability, low coefficient of thermal expansion, and superior mechanical characteristics [10]. The semi-crystallinity of PPS offers advantages such as the ability to use above-glass transition temperature without compromising modulus and creep deformation resistance [11]. To the best of our knowledge, FFF processing of CF-reinforced PPS composites has been studied only to a limited extent

Although studies on PPS in FFF are limited, there have been some previous investigations. Kishore et al. studied the rheological, thermal properties of PPS and their correlation to the FFF process, where authors successfully able to make prints [12]. Liu examined the structure-property relationships of additively manufactured CF-PPS composites based on small amplitude rheology, morphology, crystal structure, and dynamic mechanical behavior tried to find the correlation between intrinsic material properties to macroscopic AM structural properties [13]. Since PPS is a semi-crystalline polymer, Kenny et al. [14] studied the crystallization kinetics using an Avrami equation and observed increased crystallization due to the presence of CFs. Vieille et al. [15] conducted a tensile test on quasi-isotropic CF-PPS composites at room temperature and elevated temperature (120 °C). The authors observed a modest 3% and 8% reduction in tensile strength and

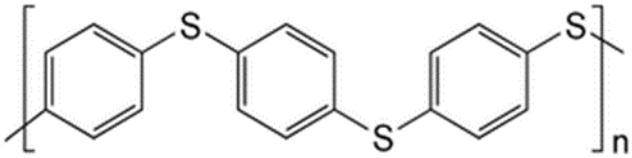

Figure 2.1: Chemical structure of PPS [16]

modulus, respectively, at 120 °C, although the glass transition temperature of PPS is 85°C. At lower temperatures (285 °C), PPS resin converts to a low melt flow polymer that can be used in injection molding, compression molding, powder spraying, free sintering, etc. [17]. Due to these excellent properties, CF-PPS finds use as a composite material in aerospace, automobile, and other high-temperature applications. Kunc et al. investigated CF-PPS composites for application in autoclave AM composite molds and observed that the mold deformed less than 0.1 mm at the composite layup area [18].

Extrusion deposition fabrication (EDF) is an AM process similar to FFF in that it uses a single screw extruder to melt pellets of a wide variety of thermoplastic materials [19]. Oak Ridge National Laboratory (ORNL), in collaboration with Cincinnati Incorporated, developed the first EDF-AM system, Big Area Additive Manufacturing (BAAM). The system is equipped with a single screw extruder that can deposit material at a rate >200× faster (up to 50 kg/h) than conventional FFF units [20, 21].

This study aimed to utilize CF-PPS 50 wt.% (50CF-PPS) pellets as a feedstock material in EDF, to further investigate the use CF-reinforced polymers as viable materials for the AM production of functional load-bearing components, and to further the understanding of the performance of CF-PPS in AM in general. X-ray photoelectron spectroscopy (XPS) was conducted to analyze the bonding characteristics between CF and PPS. The pellets were processed using EDF-AM, injection molding (IM), and extrusion compression molding (ECM) to manufacture composite plaques. The processing conditions were guided by the results from differential scanning calorimetry (DSC) and thermo-gravimetric analysis (TGA) of the CF-PPS pellets. After the samples were manufactured, detailed mechanical and microscopic investigations were carried out to study the strengths and weaknesses of the EDF-AM process, compared to the more traditional methods. Fiber length

distribution characterization was performed to understand the effect of manufacturing technique on the fiber attrition.

2.2 EXPERIMENTAL

2.2.1 Materials and Processing

The 50CF-PPS pellets, procured from Techmer PM., were dried at 100°C for 8 hours before further processing via EDF-AM, ECM, and IM, each of which was used to obtain test coupons for mechanical evaluation. The EDF-AM and ECM setup equipment were located at Manufacturing Demonstration Facility (MDF), ORNL, while IM equipment at Techmer PM, TN, USA.

For the EDF-AM sample, a BAAM system was used to print a hexagon measuring 304.8 mm × 304.8 mm × 22 mm, from which coupons were extracted. In the EDF-AM process, the CF-PPS pellets were fed into the extruder with five heating zones that were set at 305°C, 321°C, 327°C, 332°C, 338°C, while the bed temperature was 110°C. The nozzle diameter was 10.16 mm (0.4″), 105 seconds layer time and layer height were set to 2.54 mm (0.01″).

The ECM process involved a low shear extruder and a fast-acting compression press [22]. For ECM plaques, a single screw, low shear extruder (Impco B20 plasticator) and a Beckwood 100-ton hydraulic compression press were used. To prepare a hot, molten charge, the plasticator zones were set at 300 °C, 305 °C, 310 °C, 310 °C temperature and 50.8 mm (2″) diameter × 53.34 mm (2.1″) long charge size was maintained. The molten charge was placed in the mold mounted on the hydraulic press, and 152.4 mm × 152.4 mm flat plates were prepared. The mold was set at 110 °C with 12.7 MPa pressure for 120 seconds.

According to ASTM D638, dog bone-shaped samples were prepared using a 110-ton Arburg injection molding machine. The pellets were melted inside the barrel by maintaining the temperature at different zones to 343-370 °C with a back pressure of 4-8.1 MPa (580-1175 psi).

The dog bone shaped samples were prepared using a mold that was set at 177-210 °C temperature and 40-75 MPa (5800-11000 psi) pressure was applied.

2.2.2 Testing and Analysis

Using a Thermo Scientific Model K_α XPS instrument, X-ray Photoelectron Spectroscopy (XPS) was conducted on the CF, neat PPS, and compounded CF-PPS pellets to understand the interfacial bonding. The instrument used micro-focused, monochromatic Al K_α X-rays (1486.6 eV). The samples were mounted on clean glass slides, and because the glass slides were insulated, a charge compensation system was used. The system consisted of low energy Ar-ions and low energy electrons in an analysis chamber with a 2×10^{-7} mbar pressure. Qualitative and quantitative analyses were conducted using a broad energy range spectra (0-1350 eV). A narrow energy spectra was used to assess the chemical bonding of carbon, oxygen, sulphur (pass energy: 50eV, step size: 0.1 eV). Thermo Scientific Avantage XPS software (v4.61) was used to collect and analyze data.

Thermo-gravimetric analysis (TGA) was conducted on the neat PPS and 50CF-PPS pellets under oxidative environments to understand thermal stability and degradation behavior. Mettler 840 TGA was used to identify the thermal degradation from room temperature to 800°C, at a heating rate of 10 °C/min. Differential scanning calorimetry (DSC) was used to characterize the melting behavior of the 50CF-PPS pellets. The heat/cool/heat procedure was performed using a Mettler DSC821e instrument. The samples were heated from 25 °C to 350 °C at a rate of 10 °C/min to remove thermal history. The samples then cooled down to room temperature and were reheated at 10°C/min to obtain a peak melting point. DSC and TGA data helped to identify the lower and upper limit of the processing temperature.

The X-ray Computed Tomography (X-CT) scan was performed to compare the porosity content after each fabrication technique (EDF-AM, ECM, and IM). A Zeiss Xradia Versa 520 XCT

instrument with 40 kV acceleration voltage (low voltage was selected to increase contrast) at 3 W power was used. The samples were rotated along the vertical axis for 360 degrees to collect images 1601 times at equal rotational intervals. A 20X scintillator objective with attached CCD camera was used to capture a 615 µm diameter field of view. A 2×2 camera binning was used, yielding a pixel size of 0.66 µm.

Mechanical characterization included tensile, flex and interlaminar shear strength (ILSS) tests. For the EDF-AM samples, mechanical tests were done on the X-direction (aligned with printing tool path) and Z-direction (orthogonal to the bead axis). For the ECM samples, mechanical tests were done on the X-direction (along the placement of the charge) and Y-direction (transverse to charge). The direction of the test coupons for EDF-AM and ECM are schematically shown in Figure 2.2.

For each manufacturing process, a set of five tensile specimens were prepared according to the ASTM D638. EDF-AM tensile samples were milled flat to 8.03 mm thick. The average width and thickness of the ECM samples was 11.3 mm × 4.4 mm, while the average of the IM samples was 12.8 mm × 3.2 mm. The tensile tests were performed on a 100 KN load cell MTS frame and pulled at a 1 mm/min loading rate. An extensometer was attached to monitor strain.

Flexure and ILSS tests were conducted on a Test Resources, Minneapolis, MN frame with a 50 KN load cell according to ASTM D790 and ASTM D2344, respectively. The thickness of the EDF-AM samples was reduced to 11 mm for the flexure and ILSS tests. A set of five samples from

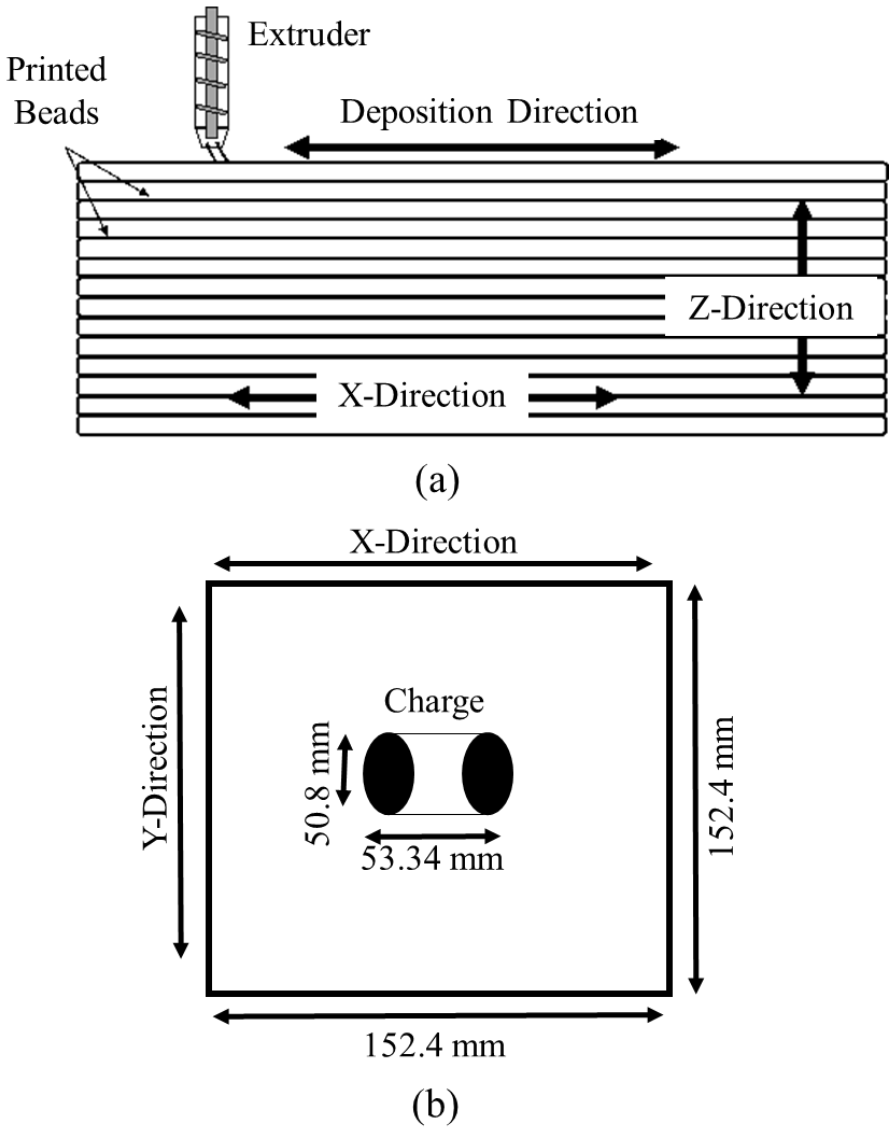

Figure 2.2: Schematic for testing coupons directions; (a) EDF-AM hexagon edge (304.8 × 304.8 mm²). Bead: Each successive layer deposited by the extruder, and (b) ECM plaque (152.4 × 152.4 mm²). Charge: Location of the charge placed in the mold

Table 2.1: Number of test specimens and dimensions

Test	ASTM Standard	Process	Average Dimensions (mm)		Number of Test Specimens
			Thickness	Width	
Tensile	D638	EDF-AM	8.03	19.16	5
		ECM	4.40	11.32	5
		IM	3.20	12.81	5
Flexure	D790	EDF-AM	11.09	12.80	5
		ECM	4.43	12.64	5
		IM	3.17	12.82	5
ILSS	D2344	EDF-AM	11.13	22.08	5
		ECM	4.26	8.41	5
		IM	3.15	6.75	5

each process was subjected to flexure tests. The EDF-AM, ECM, and IM samples were loaded at 4.7 mm/min, 1.9 mm/min and 1.4 mm/min, respectively. ILSS testing was performed at a 1 mm/min loading rate for each of a set of 5 test pieces from the EDF-AM, ECM and IM techniques. Specimen dimensions and the number of test pieces for each set of samples are summarized in Table 2.1.

The manufacturing process of EDF-AM involved the extrusion of material through a nozzle and thus created a part layer-by-layer. The process did not involve any material flow/injection. Therefore, it can be assumed that all the possible fiber length variation distribution was observed inside the extruded material only, and so the FLD calculations of EDF-AM samples were measured from a single representative location. In the ECM process, a charge was produced from a plasticator and then transferred to a hydraulic compression press which, due to the application of tonnage charge flows, filled the mold cavity. This process involved the flow of the molten material, which represents the distribution of fibers in all directions. Therefore, 5 locations were considered for FLD measurements, as shown in Figure 2.3. The manufacturing technique of IM consisted of an injection of molten material into the mold cavity through a small nozzle. Material flow also occurred in this process; therefore, FLD was analyzed at three different locations (Figure 2.3). The FLD measurement for each manufacturing technique was calculated by the code developed by Kunc et al. at ORNL [23].

2.3 RESULTS AND DISCUSSION

2.3.1 Spectroscopic Analysis

XPS analysis was conducted to evaluate the chemical composition of the fiber and polymer, as well as the chemical reaction at the fiber/matrix interface. The intensity peak at approximately 284 eV binding energy was observed in the overall XPS spectra of fiber (Figure 2.4-1a) and polymer

surfaces (Figure 2.4-2a), indicating a high content of carbon. The fiber surface exhibited a considerable amount of oxygen and a small quantity of nitrogen, as indicated by the existence of peaks at nearly 535 eV and 400 eV binding energy, respectively. The presence of nitrogen was due to residual nitrogen during the conversion of the precursor into carbon fiber [24]. High-resolution spectrums of carbon (C1s) (Figure 2.4-1b) and oxygen (O1s) (Figure 2.4-1c) were examined to identify surface composition. The C1s spectrum consisted of several overlapping peaks identified as C-sp2, C-sp3, C-N bonds, C-O bonds, and O=C-O bonds, while the O1s spectrum showed the presence of O-C and O=C features, as well as some adsorbed –OH (or H_2O). It is important to note that, during compounding, significant fiber breakage takes place due to interaction with (i) screw, barrel and wall surface, (ii) other fibers, (iii) polymer type (amorphous/ semicrystalline) [4]. However, a fiber length distribution (FLD) measurement of 50CF-PPS samples was not possible (explained in section 3.2). Therefore, to understand the effect of the fiber attrition during the different manufacturing techniques, 20% reinforced CF-ABS (20CF-ABS) pellets, procured from Techmer PM, were processed using EDF-AM, ECM and IM to prepare panels using the same procedures as described above for the CF-PPS pellets. ABS is an amorphous polymer which means it has no exact melting point. Therefore, for extrusion purposes, 230 °C was considered as a standard melting temperature [25].

The CF and PPS were compounded using a co-rotating twin-screw compounder, in which the polymer was first introduced in the heated twin screw and then, approximately halfway down the extruder, the CF was added through a side feeder. The compounded CF-PPS strands were cooled and chopped into pellets in a rotating knife pelletizer. Figure 2.5a illustrates a low-resolution

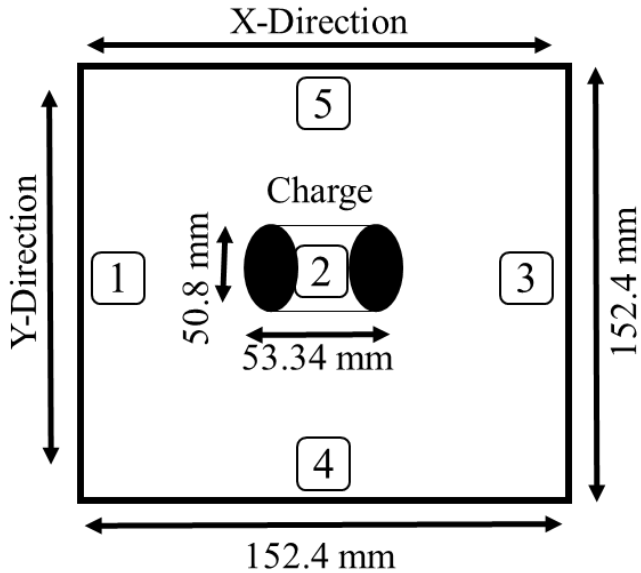

(a)

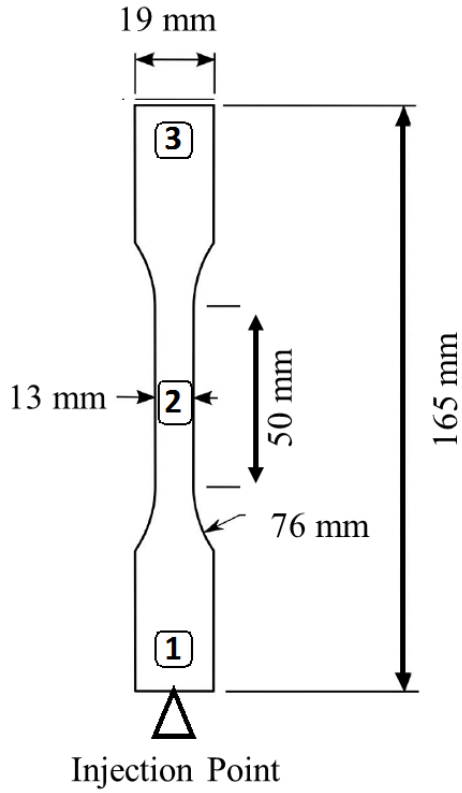

(b)

Figure 2.3: Samples locations for FLD calculations; (a) ECM, and (b) IM

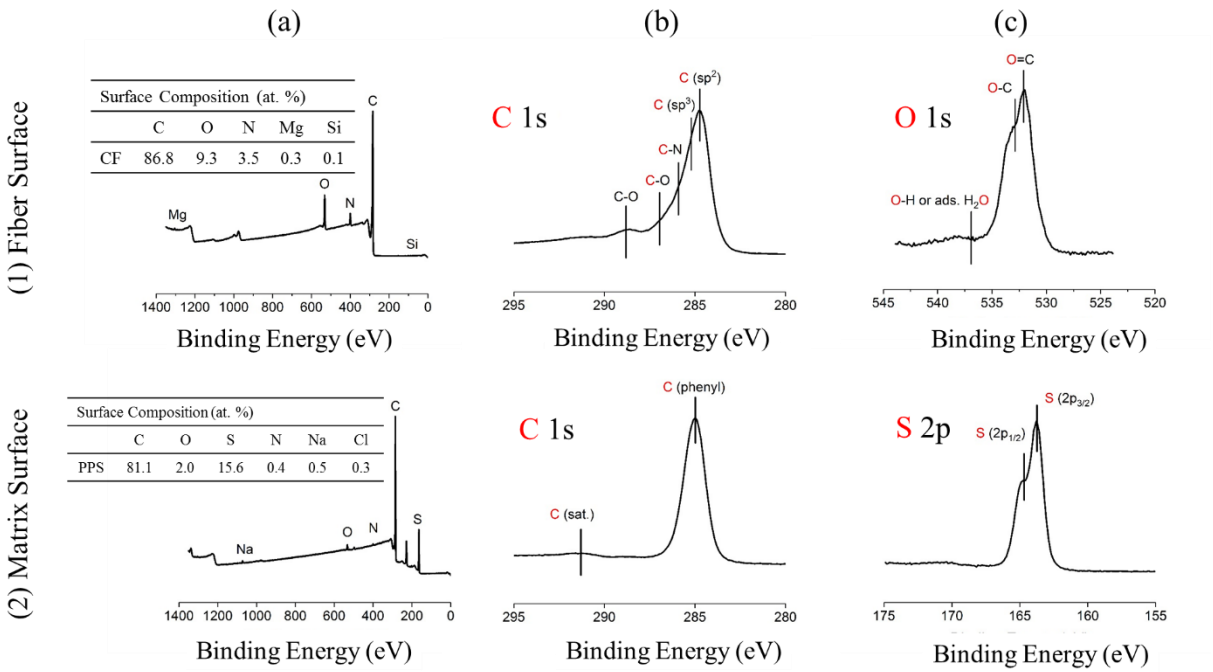

Figure 2.4: XPS Spectra of; (1) Fiber Surface: (a) Overall Spectra, (b) C1s, (c) O1s; and (2) Matrix Surface: (a) Overall Spectra, (b) C1s, (c) S2p

spectrum obtained from CF-PPS compounded pellets representing C, O, and S as the main elements. The high-resolution spectra of C1s showed a peak at 284.5 eV binding energy, which corresponded to the carbon atoms in the phenyl rings [26]. Carbon has a tendency to bond Sulphur; however, a high-resolution spectra of C1s did not show any evidence of chemical reaction formation, as shown in Figure 2.5b.

The high-resolution spectrums of C1s and O1s from CF and CF-PPS are compared in Figure 2.6. Note that the high-resolution spectra of C1s and O1s from each material were different, indicating adhesion at the fiber and polymer interface. Figure 2.6 also indicates that there was no chemical reaction (only physical bonding) contributing to the adhesion at the CF and PPS interface. Weitzsacker et al. also observed similar results, finding no significant chemical reaction between CF and PPS interface bonding [27].

2.3.2 **Thermal Analysis**

Figure 2.7 a and b show the TGA and DSC results, respectively, for the 50CF-PPS pellets. Heat-cool-heat cycle was used for the DSC. Initial heat cycle was used to remove the presence of thermal history on the PPS resin. During cooling it was noted that PPS starts recrystallization at 250°C. It can be observed from the last heating cycle of DSC curve that the glass transition temperature and melting point of 50CF-PPS was in the range of 85-90°C and 280-285°C respectively. Melting point determines the lower processing temperature limit. The TGA curve showed less than 1% weight loss up to 400°C, indicating PPS stability and the upper processing temperature limit. Therefore, the processing temperature for each manufacturing technique was maintained in the range of 285 to 400°C.

Surface Composition (at. %)						
	C	O	N	S	Na	Cl
CF/PPS	80.7	7.2	0.7	9.4	0.2	0.4

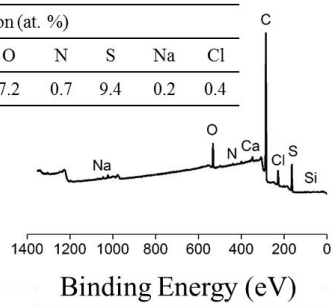

(a)

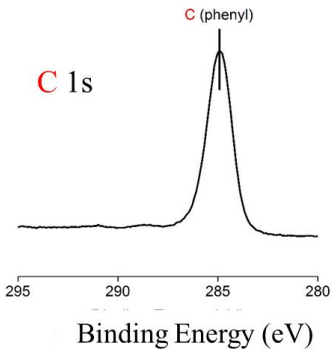

(b)

Figure 2.5: XPS Spectra CF-PPS Composite; (a) Overall spectra, and (b) C1s

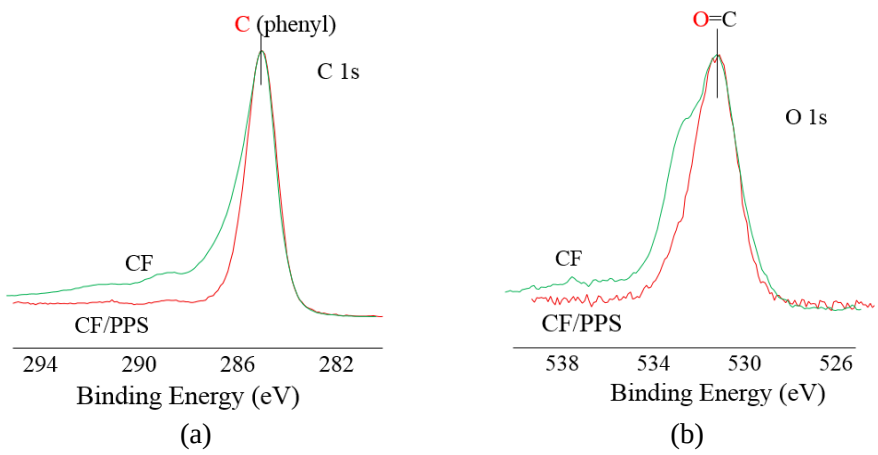

Figure 2.6: Overlapping spectra for CF and CF-PPS; (a) C 1s, and (b) O 1s

Figure 2.7b indicates the degradation behavior of neat PPS resin and 50CF-PPS at 10°C/min heating rate in air. The degradation for neat PPS was completed at 700°C. However, at that temperature, the composite material maintained 74% wt, indicating that the presence of CF leads to an increase in carbonaceous residue [28, 29]. Oxidation of CF started at 500°C, and complete degradation of 50CF-PPS was observed at 800°C. Oxidation resulted in the reduction of cross-section and weight loss of CF, as can be observed in Figure 2.7b [30, 31]. Therefore, it was impossible to burn-off/get rid of PPS without damaging the aspect ratio of CF. Also, to the best of our knowledge, no chemical is available to dissolve PPS without affecting the CF surface. Therefore, we were not able to study the effect of the different manufacturing processes (i.e. EDF-AM, ECM, IM) on the fiber length attrition for the 50CF-PPS system. As previously mentioned, an alternative material system (20CF-ABS) was used to understand the effect of different manufacturing techniques on fiber attrition.

There were more than 1500 fibers measured for each individual position within a process. The FLD of the pellets and all of the processing methods are given in Table 2.2. The average fiber length of the pellets was 0.372 mm, and it can be observed from Table 2.2 that fiber attrition took place during each manufacturing technique. On average, fiber length distribution from ECM (0.348 mm) > EDF-AM (0.330 mm) > IM (0.321 mm). In the ECM process, a molten charge was produced using a low shear extruder, which helped to retain maximum fiber length as compared to the other manufacturing processes. The IM injection molding screw design affected the fibers, resulting in a small fiber aspect ratio. The EDF-AM extrusion screw had less impact on fiber geometry compared to IM.

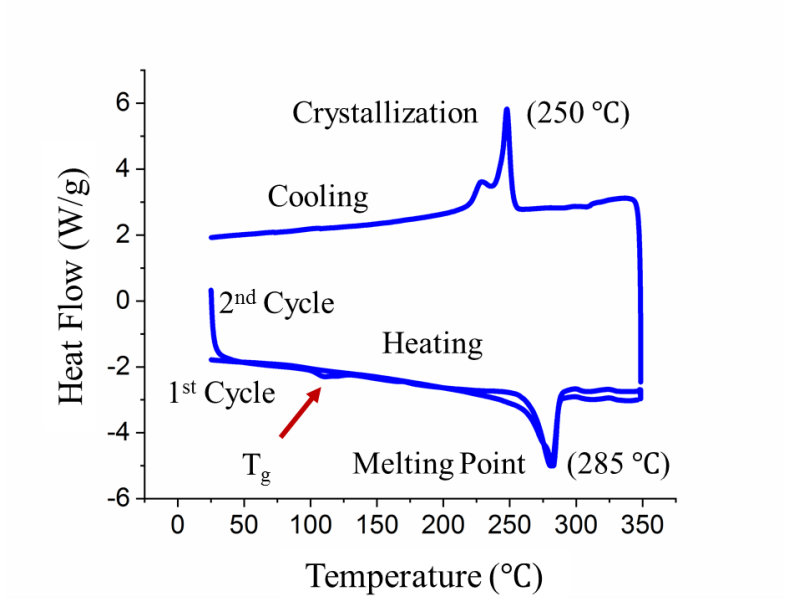

(a)

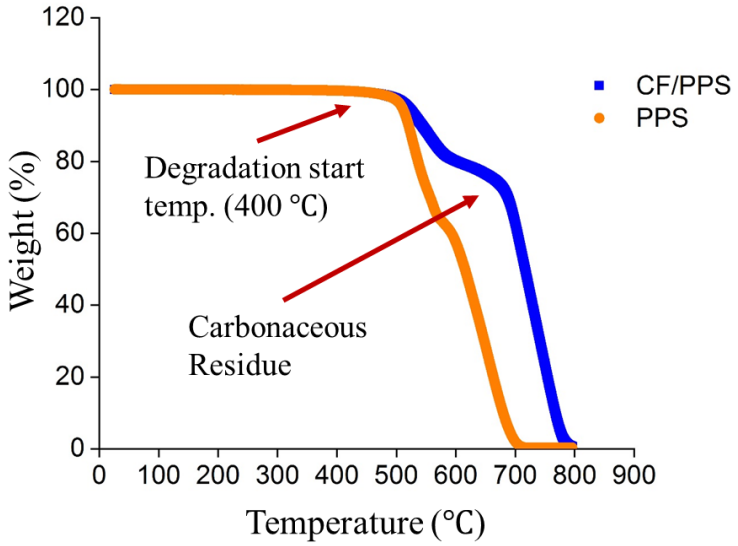

(b)

Figure 2.7: Thermal analysis results; (a) DSC of 50CF-PPS pellets: heat-cool-heat cycle from room temperature to 350 °C, and (b) TGA analysis of PPS matrix and 50CF-PPS pellets in oxidative conditions from room temperature to 800 °C

The probability function of FLD is given in Figure 2.8. From Table 2.2 and Figure 2.8 it can also be observed that local fiber length distribution for ECM and IM was different at various locations, which were due to the freezing of a skin layer. There is always a temperature gradient between the skin layer and the core material of any molten charge material. Therefore, when the charge flows, fibers get sheared and ultimately broke at the intersection between frozen skin and melt core. The chopped/short fibers stay in the skin area; however, longer fibers were transported towards the end of the flow path [33]. During the ECM process, the charge was kept at location 2, due to the way in which the force was applied and the resulting flow of material. Thus, the FLD at location 2 was the lowest, as compared to the other positions. The FLD at ECM location 5 (0.377 mm) was slightly higher than the average length distribution in the pellets (0.372 mm). The feed fiber length (pellets) was very small due to the short fibers and the low shear nature of ECM operation allowed the entire fiber length from some pellet fibers to pass unhindered. According to freeze skin layer principle all long fibers may have transferred to location 5. This was also obseved in mechanical testing as properties of ECM samples were higher in Y-direction than X-direction.

2.3.3 Porosity Measurement

The presence of porosity is detrimental to the composite structural performance. In the EDF-AM process, the structure is formed by depositing a bead on top of the next bead. When the bead is deposited, it is still soft, which causes the bottom of the bead to flatten under pressure while the top part cools down to form rounded edges. Therefore, the bead becomes elliptical even though the nozzle extrudes a circular bead. This elliptical bead formation occurred at each successive layer and caused the formation of voids aligned downwards along the printing direction, as shown in Figure 2.9. Additionally, the presence of CFs in the polymer caused the formation of inner bead voids, due to the fiber ends. Figure 2.10 (a) represent the 2D slice of EDF-AM sample obtained

Table 2.2: FLD of Pellets, EDF-AM, ECM, and IM

Sr. No.	Process/Material	Position	FLD	
			mm	Average, mm
1	Pellets	NA	0.372	0.372
2	EDF-AM	NA	0.330	0.330
3	ECM	1	0.348	0.348
		2	0.333	
		3	0.332	
		4	0.352	
		5	0.377	
4	IM	1	0.321	0.321
		2	0.317	
		3	0.326	

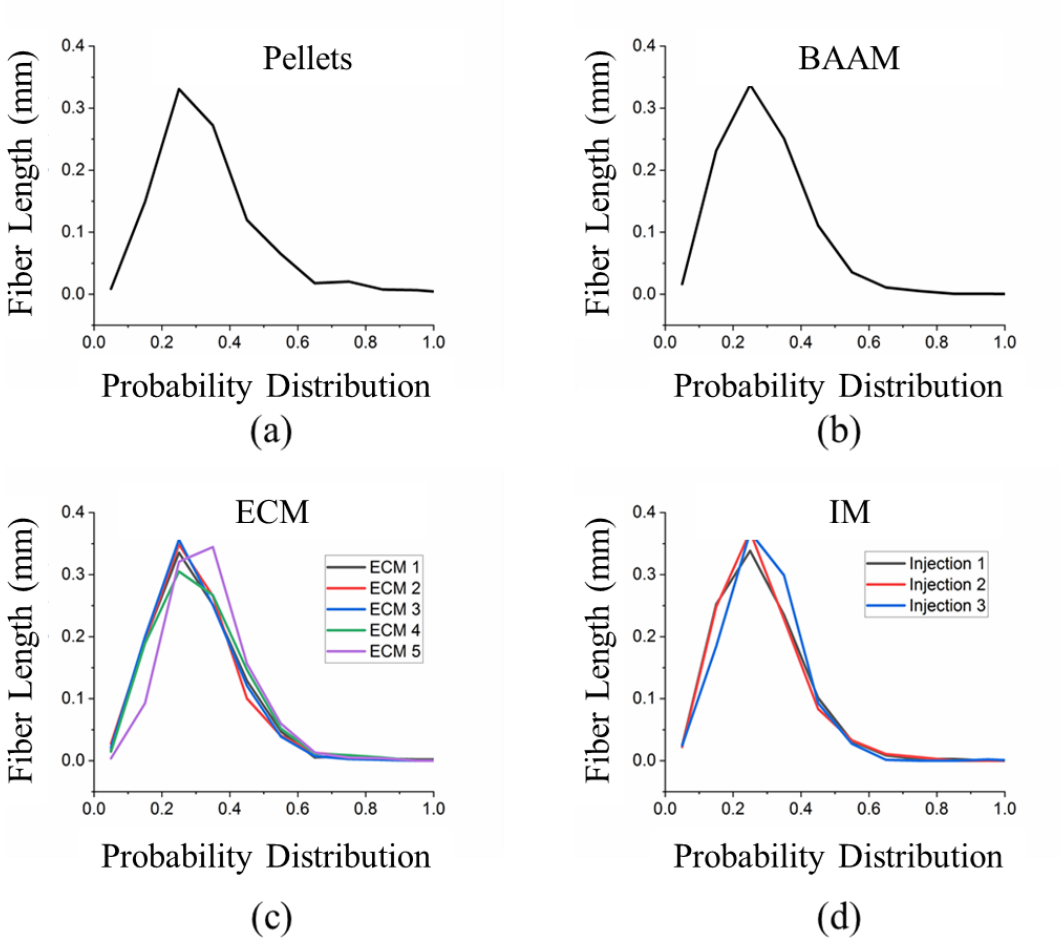

Figure 2.8: Probability distribution of CF length (a) Pellets (b) AM (c) ECM (d) IM

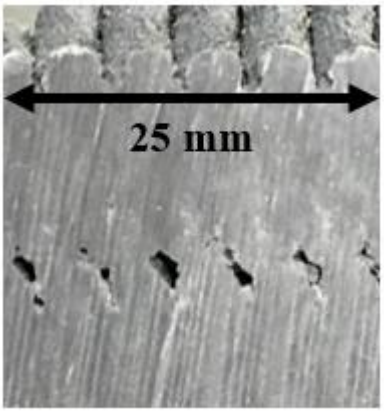

Figure 2.9: Illustration of macro-void formation during the AM process.

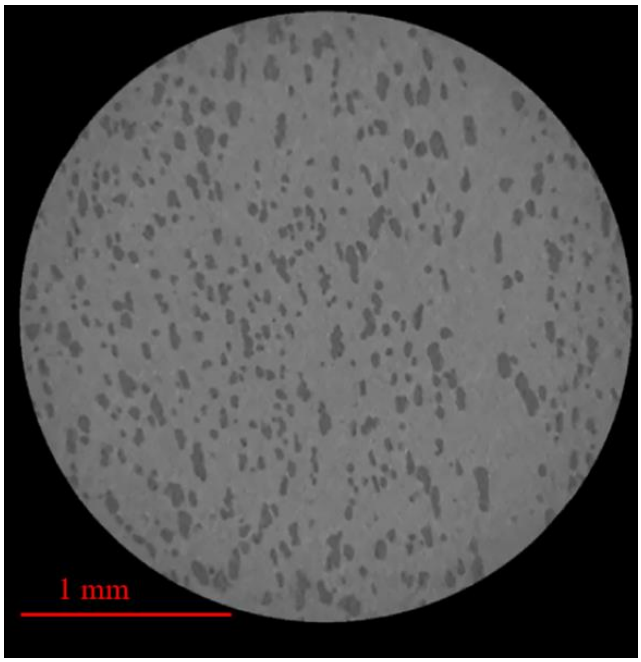

(a)

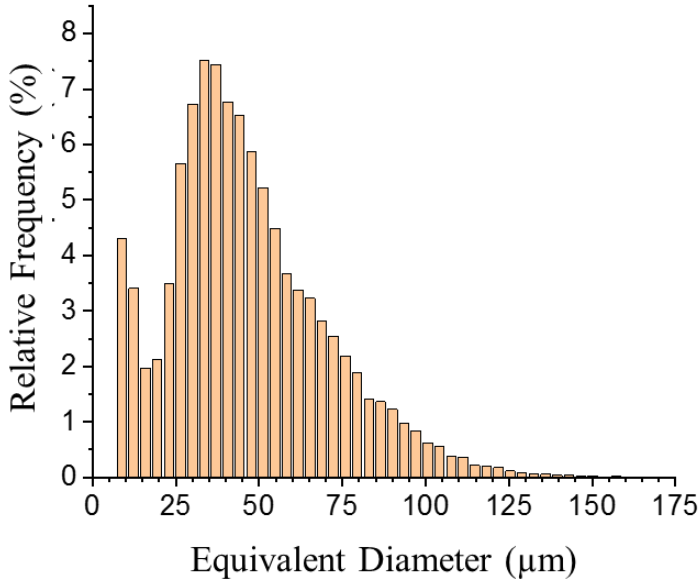

(b)

Figure 2.10: (a) X-CT image of FDE-AM specimen (b) Relative frequency distribution as a function of equivalent diameter of void. EFD-AM contain a total of 15.5 volume % voids.

from top-down views of 3D reconstruction during X-CT scanning while Figure 2.10 (b) represent the relative frequencies of the pores as a function of equivalent pore diameter (assuming pores has spherical geometry). A total porosity of 15.5% volume was observed in EDF-AM samples.

The ECM sample showed very inhomogeneous distribution of pores with a high concentration on the surfaces, as shown in Figure 2.11 (a). In ECM samples, the hot molten charge from the plasticator was placed on the relatively colder mold. Therefore, temperature of the charge which is in contact with the mold surface, dropped significantly; however, the inside material temperature was still above melting point and flowed smoothly after the application of pressure. This represents the porosity concentration mainly at the top and bottom surfaces of the ECM sample. A total of 4.3 % volume porosity was observed. A meaningfully representative size distribution could not be obtained as most of the observed pores were connected to larger single entities.

It can be observed from Figure 2.11 (b), the IM samples contain minimal porosity (0.007% by volume) as compared to other processes. This was due to the high pressure applied while injecting the material. The total number of segmented pores were not statistically significant enough for quantitative analysis.

2.3.4 Mechanical and Microscopic Analysis

The mechanical properties of EDF-AM, ECM, and IM are summarized in Table 2.3. The tensile properties of the composite are dominated by fiber orientation, void content, fiber/matrix interface [34, 35]. As noted in Table 2.3 and Figure 2.12, IM samples exhibited more tensile, flexure, and ILSS properties as compared to the EDF-AM and ECM samples, even though IM has the least average fiber length. During the IM process, fibers mainly orient in flow direction, and fiber orientation plays a vital role in mechanical characteristics [36]. This can be observed from the

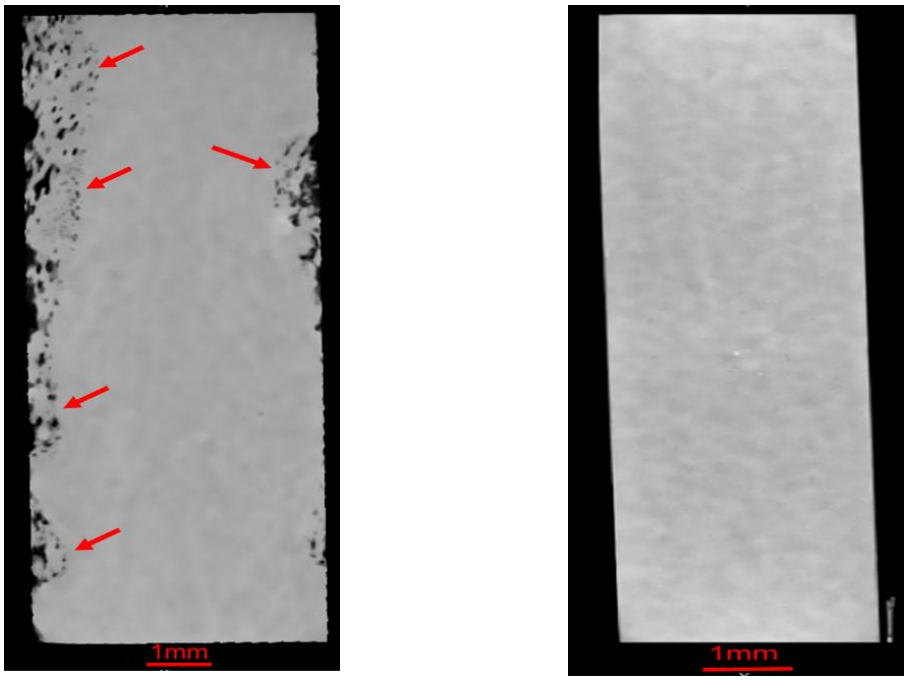

(a) (b)

Figure 2.11: (a) X-CT image of ECM specimen. All pores in ECM are present in the top and bottom surface only and contain a total of 4.30 volume % voids. (b) X-CT image of IM specimen. IM contain a total of 0.007 volume % voids

Table 2.3: Mechanical properties of EDF-AM, ECM, and IM

Sample		Tensile Test				Flexure Test				ILSS	
		Strength MPa		Modulus GPa		Strength MPa		Modulus GPa		Strength MPa	
		Mean	STD	Mean	STD	Mean	STD	Mean	STD	Mean	STD
EDF-AM	X-dir	56.02	3.13	21.56	0.56	63.23	4.51	14.35	0.92	8.34	1.04
	Z-dir	12.06	1.44	4.25	0.16	18.46	0.06	3.90	0.07	2.63	0.13
ECM	X-dir	49.61	14.6	16.35	5.55	77.33	9.55	10.77	0.91	10.29	0.38
	Y-dir	53.83	20.5	16.94	4.30	92.66	17.1	13.02	3.18	11.84	1.41
IM	Flow-dir	122.54	3.14	33.46	2.88	195.9	2.32	34.82	0.97	18.48	2.96

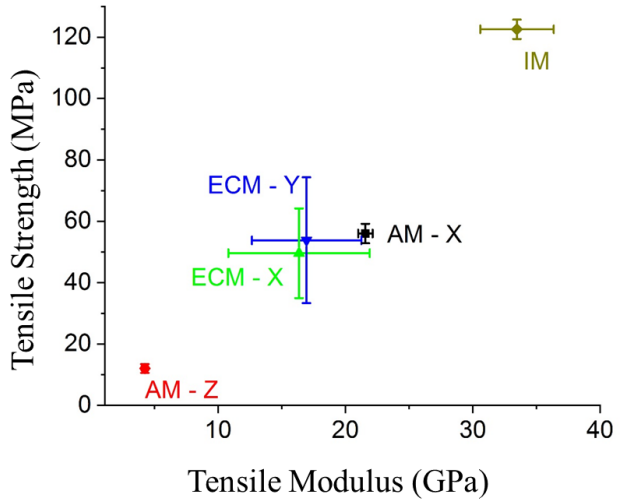

(a)

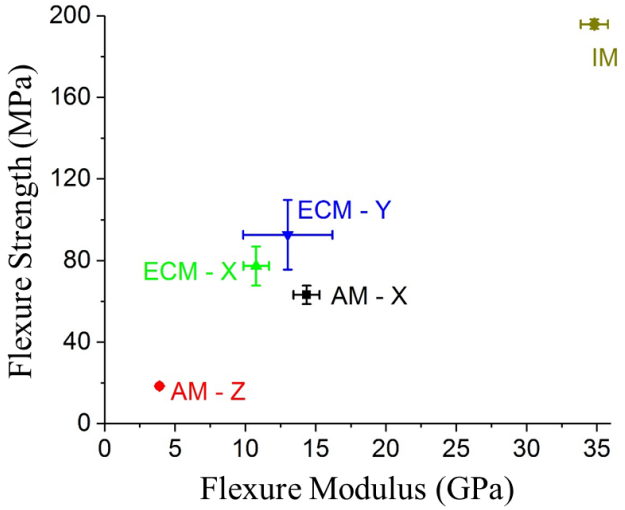

(b)

Figure 2.12: Mechanical properties for EDF-AM, ECM and IM; (a) Tensile strength versus tensile modulus, and (b) Flexure strength versus flexure modulus

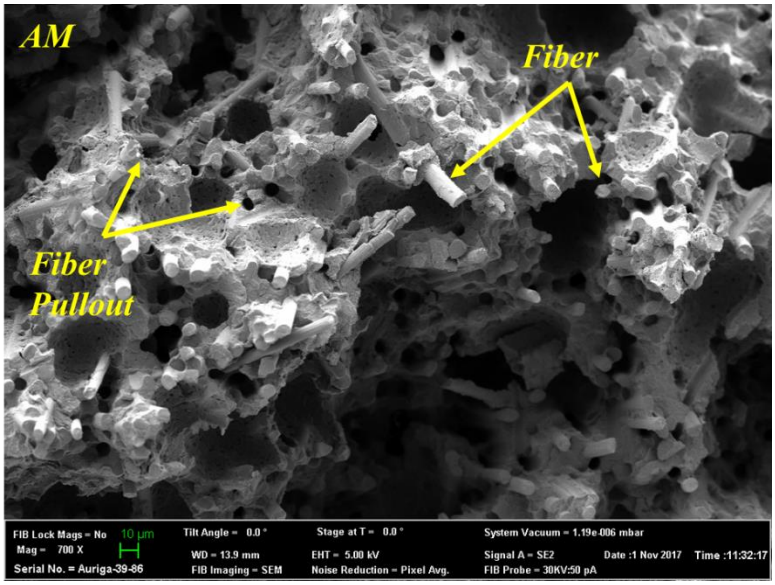

(a)

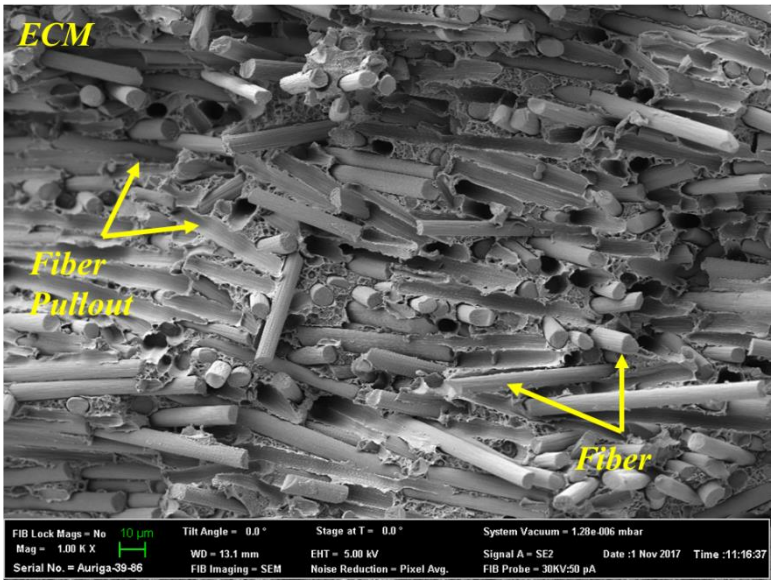

(b)

Figure 2.13: SEM micrographs of a fracture surface of tensile specimen; (a) EDF-AM: Most of the fibers are aligned in printing direction, also contain voids; (b) ECM: Fibers are well distributed in all directions

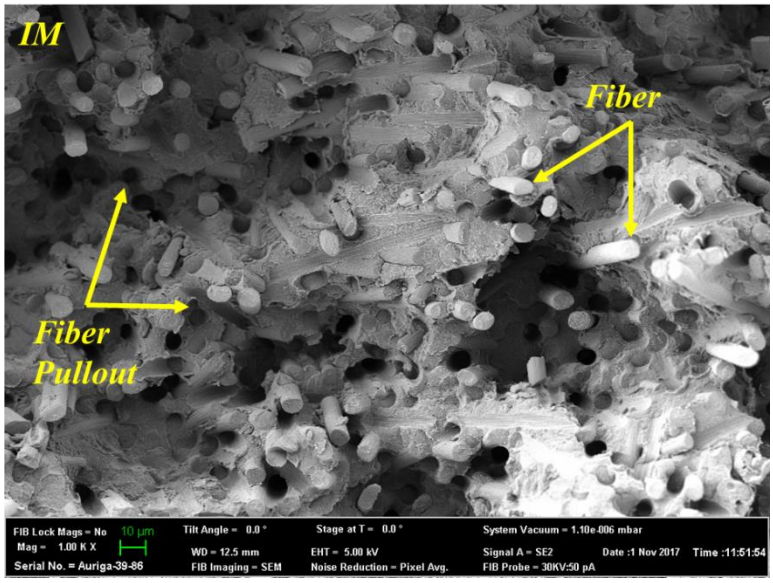

(c)

Figure 2.14: SEM micrographs of a fracture surface of tensile specimen; (c) IM: Fibers are well aligned in flow directions. All samples showed fiber pullout.

SEM image given in Figure 2.14c, in which IM fibers are mainly oriented in the flow direction. As explained in previous section the IM sample exhibit much less porosity as compared to EDF-AM and ECM samples. This collectively results in higher properties for the IM manufacturing process.

When a layer is deposited, the previous layer is already in an advanced stage of cooling, which causes weak layer-by-layer bonding. If the temperature of the substrate (previous layer) drops below the glass transition temperature (T_g) of the printing material, it causes the least amount of layer-to-layer adhesion with the next successive layer [37]. This leads to weaker Z-direction properties. Tekinalp et al. [1] explained that, during printing, fibers are aligned in the load-bearing direction, which compensates for the negative effect of voids. This can be observed from Figure 2.14 (a) where most of the fibers are oriented in one direction. Therefore, as can be observed from Table 2.3, the tensile, flexure, and ILSS strength of EDF-AM samples in the X-direction are 78%, 71%, and 68% higher, respectively, than in the Z-direction. It can also be noted that the standard deviation is not significant between the five tested samples for each set of tests in both directions.

ECM parts generally prefer planar flow patterns that distribute fibers randomly in all directions, as seen in Figure 2.14 (b). An average 20% variation is typically observed between the flow direction and transverse to the flow direction in ECM samples [36]. The random distribution of fibers leads to a high standard deviation. As explained earlier (section 3.3), the ECM manufacturing process has the most forgiving nature in terms of fiber retention as compared to other manufacturing techniques.

The tensile strength of the EDF-AM samples in the X-direction (56 MPA) was very similar to that of the ECM samples (X-direction: 50 MPa and Y-direction: 54 MPa) due to the high alignment of fibers (in EDF-AM). However, the flexure and ILSS strength of the ECM (both directions) samples

were more than 20% higher than EDF-AM (X-direction) samples. This increase in strength was due to the random distribution of longer fibers, which created cross-linking and produced more bending resistance. SEM images (See Figure 2.14) of fracture samples from all three manufacturing processes showed fiber pullout, which is consistent with the XPS results and indicates a need for improvement of the interface bonding between CFs and PPS resin.

2.4 CONCLUSIONS

Twin-screw compounded 50CF-PPS pellets were successfully used as a feedstock material to fabricate composite plaques by EDF-AM, ECM, and IM. The processing temperature for each process was maintained between 285 – 400°C, which were the melting point and degradation point temperatures, respectively, for the PPS matrix. XPS analysis showed that no chemical reaction between the fiber and matrix occurred during compounding, which was further confirmed in SEM micrographs, as the fibers were pulled out during tensile testing. The IM samples had better mechanical properties due to the aligned fibers along the injection direction. A high standard deviation in the ECM samples indicated the planar flow pattern with a random distribution of fibers. In EDF-AM printed samples, fiber orientation along the printing direction minimized voids and improved properties, compared to the ECM specimens. Measurement of the fiber length distribution in 50CF-PPS was not possible because of the oxidative nature of CF and carbonaceous residue formation at high temperatures. An alternate system of 20CF-ABS was used to observe the effect of different manufacturing techniques on the fiber attrition, which showed that IM produced the maximum reduction in the fiber aspect ratio.

In summary, this study shows that 50CF-PPS pellets are an excellent feedstock material option for additive manufacturing. The controlled orientation and excellent dispersion capabilities of the EDF-AM process has great potential for manufacturing load-bearing components. Furthermore,

there is an excellent potential to improve AM structure properties in both the X and Z directions. IM and ECM composites did not much porosity; however, their performance can be improved by increasing fiber-polymer adhesion.

REFERENCES

1. Tekinalp, H.L., et al., *Highly oriented carbon fiber–polymer composites via additive manufacturing.* Composites Science and Technology, 2014. **105**: p. 144-150.
2. Bandari, Y.K., et al. *Additive manufacture of large structures: robotic or CNC systems?* in *Proceedings of the 26th International Solid Freeform Fabrication Symposium, Austin, TX, USA*. 2015.
3. Ning, F., et al. *Additive manufacturing of CFRP composites using fused deposition modeling: effects of carbon fiber content and length*. in *ASME 2015 International Manufacturing Science and Engineering Conference*. 2015. American Society of Mechanical Engineers.
4. Fu, S.-Y., et al., *Tensile properties of short-glass-fiber-and short-carbon-fiber-reinforced polypropylene composites.* Composites Part A: Applied Science and Manufacturing, 2000. **31**(10): p. 1117-1125.
5. Love, L.J., et al., *The importance of carbon fiber to polymer additive manufacturing.* 2014. **29**(17): p. 1893-1898.
6. Luo, W., et al., *Enhanced mechanical and tribological properties in polyphenylene sulfide/polytetrafluoroethylene composites reinforced by short carbon fiber.* Composites Part B: Engineering, 2016. **91**: p. 579-588.
7. Zhong, W., et al., *Short fiber reinforced composites for fused deposition modeling.* Materials Science and Engineering: A, 2001. **301**(2): p. 125-130.
8. Ning, F., et al., *Additive manufacturing of carbon fiber reinforced thermoplastic composites using fused deposition modeling.* Composites Part B: Engineering, 2015. **80**: p. 369-378.

9. Shofner, M., et al., *Nanofiber-reinforced polymers prepared by fused deposition modeling.* Journal of applied polymer science, 2003. **89**(11): p. 3081-3090.

10. Béland, S., *High performance thermoplastic resins and their composites*. 1990: William Andrew.

11. Spruiell, J., *A review of the measurement and development of crystallinity and its relation to properties in neat poly (phenylene sulfide) and its fiber reinforced composites*. 2005, ORNL.

12. Kishore, V., et al., *Additive manufacturing of high performance semicrystalline thermoplastics and their composites*. 2016, Oak Ridge National Lab.(ORNL), Oak Ridge, TN (United States).

13. Liu, P., et al., *Rheology, crystal structure, and nanomechanical properties in large-scale additive manufacturing of polyphenylene sulfide/carbon fiber composites.* 2018. **168**: p. 263-271.

14. Kenny, J. and A. Maffezzoli, *Crystallization kinetics of poly (phenylene sulfide)(PPS) and PPS/carbon fiber composites.* Polymer Engineering & Science, 1991. **31**(8): p. 607-614.

15. Vieille, B. and L. Taleb, *About the influence of temperature and matrix ductility on the behavior of carbon woven-ply PPS or epoxy laminates: Notched and unnotched laminates.* Composites Science and Technology, 2011. **71**(7): p. 998-1007.

16. Simon, S.A., *Analysis of Fiber Attrition and Fiber-matrix Separation During Injection Molding of Long Fiber-reinforced Thermoplastic Parts*. 2016.

17. Hill, H.W. and D. Brady, *Properties, environmental stability, and molding characteristics of polyphenylene sulfide.* Polymer Engineering & Science, 1976. **16**(12): p. 831-835.

18. Kunc, V., et al. *Investigation of In-autoclave Additive Manufacturing Composite Tooling*. in *CAMX Conference, Anaheim, CA*. 2016.

19. Brenken, B., et al., *Development and validation of extrusion deposition additive manufacturing process simulations.* 2019. **25**: p. 218-226.

20. Duty, C.E., et al., *Structure and mechanical behavior of Big Area Additive Manufacturing (BAAM) materials.* 2017. **23**(1): p. 181-189.

21. Roschli, A.C., et al., *Pellet to Part Manufacturing System for CNCs*. 2018, Oak Ridge National Lab.(ORNL), Oak Ridge, TN (United States); Hybrid ….

22. Yeole, P., H. Ning, and A.A.J.J.o.T.C.M. Hassen, *Development and characterization of a polypropylene matrix composite and aluminum hybrid material.* 2019: p. 0892705719843974.

23. Kunc, V., et al., *Fiber length distribution measurement for long glass and carbon fiber reinforced injection molded thermoplastics.* 2007.

24. Viswanathan, H., et al., *X-ray photoelectron spectroscopic studies of carbon fiber surfaces. 24. Interfacial interactions between polyimide resin and electrochemically oxidized PAN-based carbon fibers.* Chemistry of materials, 2001. **13**(5): p. 1647-1655.

25. Milenius, D.L., *ABS extrusion compositions*. 1979, Google Patents.

26. Goushegir, S.M., et al., *XPS analysis of the interface between AA2024-T3/CF-PPS friction spot joints.* Surface and Interface Analysis, 2016. **48**(8): p. 706-711.

27. Weitzsacker, C.L., M. Xie, and L.T. Drzal, *Using XPS to Investigate Fiber/Matrix Chemical Interactions in Carbon-fiber-reinforced Composites.* Surface and interface analysis, 1997. **25**(2): p. 53-63.

28. Ma, C.c.M., et al., *Thermal and rheological properties of poly (phenylene sulfide) and poly (ether etherketone) resins and composites.* Polymer composites, 1987. **8**(4): p. 256-264.

29. Stoeffler, K., et al., *Polyphenylene sulfide (PPS) composites reinforced with recycled carbon fiber.* Composites Science and Technology, 2013. **84**: p. 65-71.

30. Yin, Y., et al., *The oxidation behaviour of carbon fibres.* Journal of materials science, 1994. **29**(8): p. 2250-2254.

31. Galasso, F. and J. Pinto, *Oxidation of carbon and metal coated carbon fibers.* Fibre Science and Technology, 1970. **2**(4): p. 303-315.

32. Chin, W.K., H.T. Liu, and Y.D.J.P.C. Lee, *Effects of fiber length and orientation distribution on the elastic modulus of short fiber reinforced thermoplastics.* 1988. **9**(1): p. 27-35.

33. Willems, F. and C. Bonten. *Influence of processing on the fiber length degradation in fiber reinforced plastic parts*. in *AIP Conference Proceedings*. 2016. AIP Publishing.

34. Yeole, P., et al., *The Effect of Flocculent, Dispersants, and Binder on Wet-laid Process for Recycled Glass Fiber/PA6 Composite.* Polymers & Polymer Composites, 2018. **26**(3).

35. Mallick, P.K., *Fiber-reinforced composites: materials, manufacturing, and design*. 2007: CRC press.

36. Vaidya, U., *Composites for automotive, truck and mass transit: materials, design, manufacturing*. 2011: DEStech Publications, Inc.

37. Hassen, A.A., et al. *Additive manufacturing of composite tooling using high temperature thermoplastic materials*. in *SAMPE Conference Proceedings, Long Beach, CA, May*. 2016.

3 CHAPTER

OPTIMIZING THE INFILL PATTERN OF ADDITIVELY MANUFACTURED COMPRESSION MOLDS

ABSTRACT

Carbon fiber (CF) reinforced polymer composites have been used in additive manufacturing (AM) to increase the stiffness of the parts. CF AM is being considered for tooling applications. In AM, CFs are usually aligned along the deposition direction; however, it results in anisotropic thermal properties which affect the heat transfer and warpage of the final part. In this study, three male molds with different infill patterns were produced via the extrusion deposition fabrication-additive manufacturing (EDF-AM) process. These include (a) 0°: infill pattern along the printing direction; (b) 90°: infill pattern perpendicular to the printing direction; (c) 0°/90°: alternate layers along and perpendicular directions. The effect of the infill pattern on thermal conductivity was analyzed and observed that 0° infill had the highest conductivity; however, 90° infill had the least. A multi-step approach is followed in to develop FEA model as (1) anisotropic thermal conductivity of the extruded bead (2) toolpath based on the infill pattern of the molds (determined by slicing software). FEA results showed the mechanism to increase mold surface temperature for the same infill structure. The results of this work are establishing the optimal configuration of AM tool designs for the compression molding of composites.

Keywords: thermal conductivity, infill pattern, extrusion deposition fabrication – additive manufacturing, finite element analysis

3.1 Introduction

CNC machining is the most commonly used and highly reliable manufacturing technique to produce dies and tools. However, it is time-consuming and expensive. Also, CNC machining requires highly skilled labor [1]. In the last decade alone, more than one-third of the tool and die companies have gone out of business because the US manufacturers have started to produce molds overseas due to cost considerations [2]. Additive manufacturing (AM) enables creating final parts through layer wise printing. AM offers potential advantages over traditional tool manufacturing [3] process because of the following factors- (i) Lead time reduction: Fabrication of tooling by AM can lead to 40-90 percent time saving due to fewer labor inputs, machining steps, use of digital design files rather than 2D paper drawings and in-house tooling; (ii) Cost reduction: AM for tooling helps cost reduction due to decrease in material lost during fabrication, improving product yield and reducing labor inputs. (iii) Improved functionality: AM allows the manufacturing of previously unobtainable and/or unaffordable (due to complex shapes) tool designs. (iv) Increased ability to customize parts.

The growth in AM over the last two decades has made significant changes in composite tooling; however, has limitations such as print speed, cost, material properties. Recent developments in polymer extrusion deposition created a lot of attention for composite mold production. Printing outside an oven is possible due to the introduction of low thermal expansion coefficient carbon fiber (CF) in polymer AM, which provides not only stiff structures but also high dimensional stability [4-6]. Cincinnati Incorporated and Oak Ridge National Laboratory (ORNL) have created a large-scale big area additive manufacturing (BAAM) system (6 m × 2.5 m × 1.5 m) to manufacture AM parts which can deposit material at a rate of 45 kg/hr. The feedstock materials

for BAAM are pellets, rather than wires, which significantly reduces cost and also broadens the supply chain of materials [7, 8].

Conventional manufacturing technique for CF includes melt spinning, oxidation, carbonization and graphitization, which helped to create an ordered structure similar to single crystal graphite [9]. Therefore, at elevated temperature, CF possesses a wide range of elastic modulus, thermal expansion, and thermal conductivity [10]. High-temperature thermoplastic polymers (polyphenylene sulfide (PPS), polyethersulfone (PES), polyetheretherketone (PEEK), polyimide (TPI)) retain physical properties at high temperatures and offer thermal stability when used for longer time [11-14]. Thermal conductivity and coefficient of thermal expansion (CTE) are essential material properties of CF composites when used at elevated temperature environments [9, 15-18]. CF is a highly anisotropic material with different mechanical and thermal properties along and transverse directions [19]. Pradere et al. [9] explained that the CTE of CFs along the transverse direction varies from 5×10^{-6} K^{-1} – 10×10^{-6} K^{-1}; however, along the longitudinal direction offers lower expansion as 1.6×10^{-6} K^{-1} – 2.1×10^{-6} K^{-1} based on the fiber properties. Therefore, thermal conductivity and expansion characteristics of chopped/short composites are highly influenced by the fiber orientation [20].

The extrusion deposition fabrication - additive manufacturing (EDF-AM) system consists of a single screw extruder where the screw rotates inside a heated barrel. The screw forces the material inside the barrel feed section to the transition section where it is melted and transferred to a metering section of the screw. Finally, material is squeezed out from the deposition nozzle under high pressure [21]. The flow kinematics of the fibers in the extruded bead are given in Figure 3.1. Studies by Brenken et al. [22] has shown that fibers are highly aligned along the deposition direction at the wall of the nozzle due to high shear forces; however, randomly oriented at the

center of the bead [4]. Properties of fiber reinforced polymers (FRPs) are depend on the orientation of fiber [23]; therefore, the mechanical and thermal properties of the composite material depend on the orientation of the deposited layer.

This research focuses on different infill patterns within the 3D printed substrate and the effect of fill pattern on the thermal conductivity and thermal expansion (warpage) of a composite mold manufactured by the EDF-AM process. The molds were heated through conductive mechanism. The thermal effect (warpage of the mold) was monitored by comparing non-contact 3D digital imaging of the molds before and after heating. Finite element analysis (FEA) was performed to find the effect of number of perimeters (explained in section 3.2) on the heat conduction of the mold.

3.2 Materials and Sample Preparation

50% by weight CF reinforced polyphenylene sulfide (50CF-PPS) was procured from Techmer PM. The melting point of PPS is 285 °C, it is a semi-crystalline thermoplastic polymer with a high heat deflection temperature [7]. The BAAM extrusion system with 10.16 mm (0.4 in) nozzle orifice diameter was used to print dome-shaped molds, as shown in Figure 3.2. The surface of the printed structure is beaded due to the nature of the BAAM print, which leads to an extra post-processing step to obtain good quality surface. The mold was printed slightly bigger (2.54 mm) than the target geometry using BAAM; then, machining was performed to remove excess material and achieved the exact target surface finish. The BAAM screw extruder has five heating zones, and these were set as; zone 1: 305 °C, zone 2: 321 °C, zone 3: 326 °C, zone 4: 337 °C, zone 5 (tip): 337 °C. The bead width: 13.97 mm (0.55”), and bead height: 5.08 mm (0.2”) was kept constant for all prints.

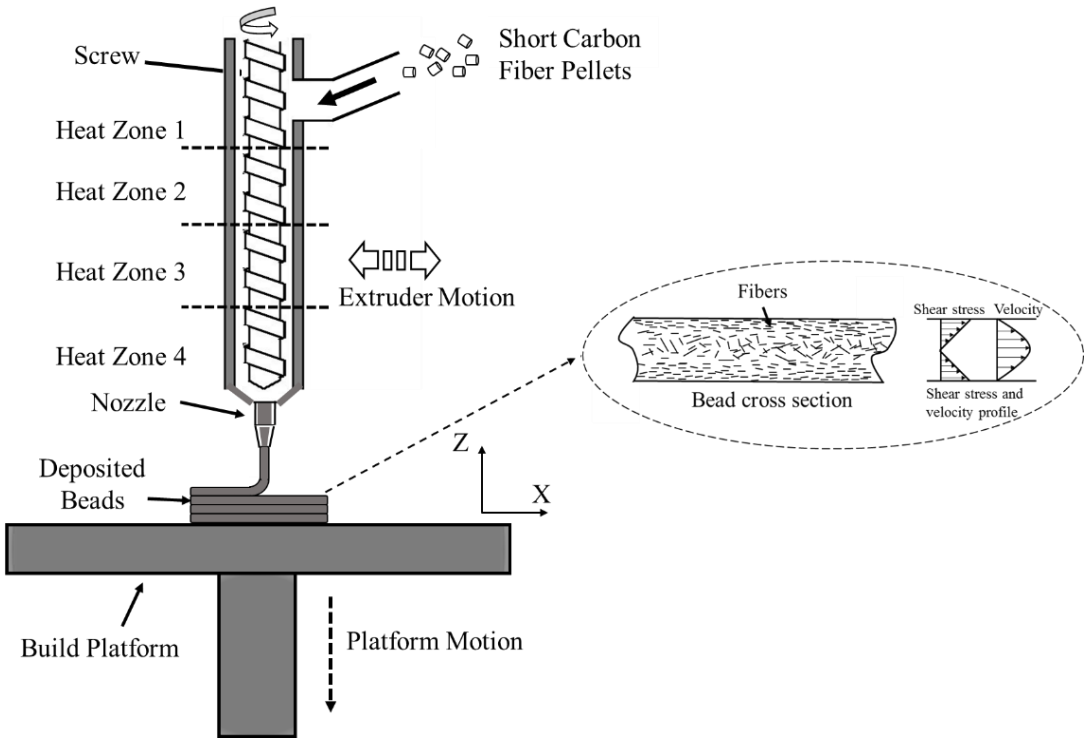

Figure 3.1: Schematic of AM extruder with fiber orientation profile inside the deposited bead. Fibers are aligned along the edge while randomly oriented inside the bead [22].

The 3D printing was conducted by using an acrylonitrile butadiene styrene (ABS) sheet to begin the print, and the bed temperature was maintained at 110 °C to adhere to the initial layer. A thermal camera (FLIR A35) was positioned to monitor the deposition temperature such that the interface temperature between the layers was always higher than the glass transition temperature (T_g) of PPS (85 °C) [24]. Printing of 50CF-PPS was performed under inert environment (argon or nitrogen) because extrusion under ambient temperature leads to significant accumulation of viscous material inside the extruder, which can degrade the polymer [7].

Perimeter also known as shell in 3D printing is an external boundary added during part building as shown in Figure 3.3. The perimeter is an essential parameter for the uniform distribution of stresses to avoid premature failure [25]. For every printed part should have at least one perimeter. Additional perimeters provide strength the part; however, also adds weight and increase print time. The infill pattern is the interior structure/geometry of the printed cross-section (inside the perimeter). Infill density and geometric patterns have a significant effect on the mechanical performance of the printed structure [26, 27]. As explained earlier (section 1), in BAAM printing, fibers are aligned along the deposition direction. Therefore, the structure of the infill pattern is hypothized to have significant influence on the fiber orientation. The fiber orientation would therefore have an effect on the thermal conductivity and the warpage of the final part [28]. Three male molds as shown in Figure 3.2 (a) were manufactured with three perimeters and different infill patterns. The three molds feature an infill pattern of 0° (along the deposition direction), 90° (transverse to the deposition direction) and 0°/90° (one layer along the deposition direction while the second transverse). The schematic of various infill patterns is shown in Figure 3.3.

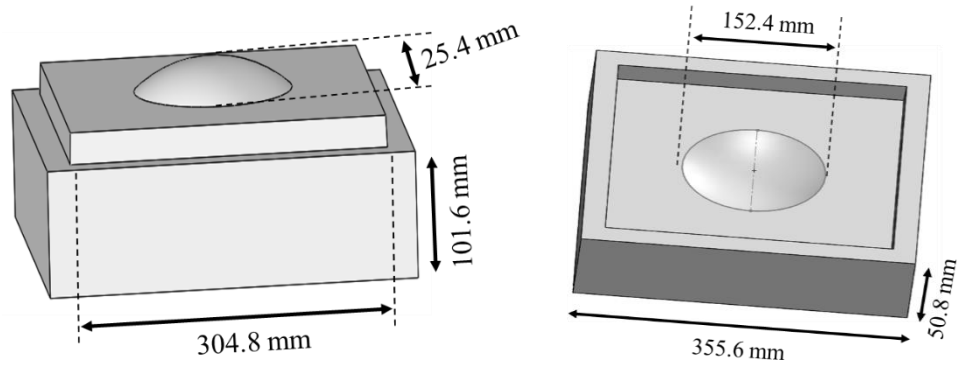

(a) (b)

Figure 3.2: Design of 50CF-PPS printed dome-shaped mold (a) Male mold (b) Female mold. The molds were printed using BAAM with bead width 13.97 mm (0.55”), and bead height: 5.08 mm (0.2”)

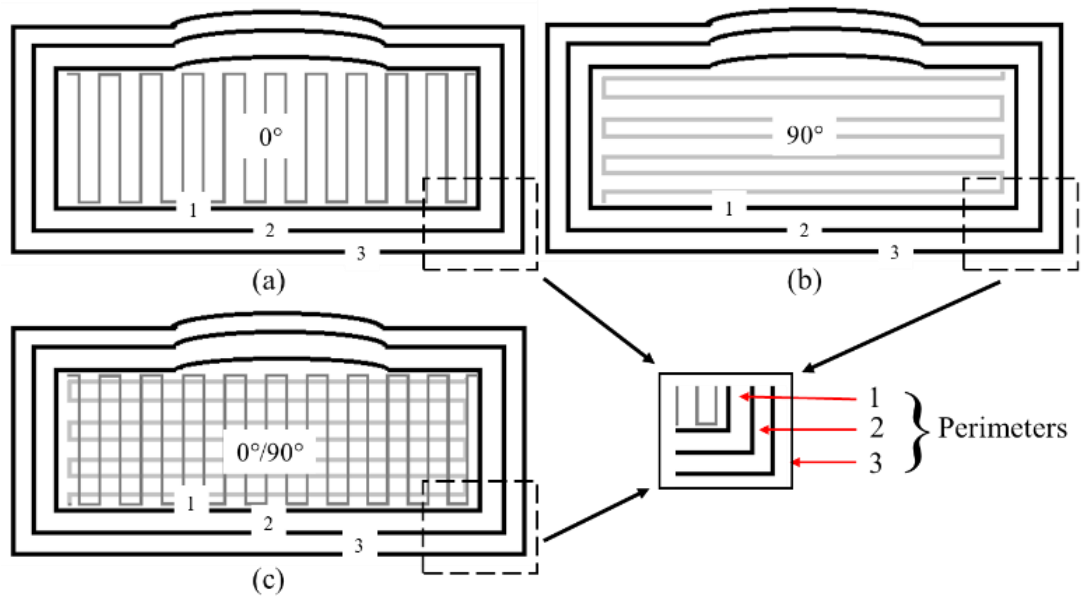

Figure 3.3: Infill pattern (a) 0° (b) 90° (c) 0°/90°. The bead width: 13.97 mm (0.55”) and bead height: 5.08 mm (0.2”)

A 304.8 mm × 304.8 mm × 22 mm width, length and thickness hexagon was prepared by EDF-AM process with 1 minute and 45 seconds layer time as shown in Figure 3.4. Test specimens were prepared to perform high-temperature tensile tests (room temperature, 100 °C, and 180 °C) according to ASTM D638. A set of 15 dog bone tensile samples of 8.03 mm thickness and 19.16 mm width (5 for each temperature) in X-direction (aligned with printing tool path) and Z-direction (orthogonal to the bead axis) respectively were prepared. MTS frame - 100 KN load cell was used to performed tensile test at a 1 mm/min loading rate.

3.3 Experimental Setup

Each male mold was placed on the platen of the hydraulic compression press (Beckwood – 100 tons) and subjected to conductive heating. Nine (9) thermocouples were placed on the mold surface and one on the platen to measure the temperature at various locations. The temperature of the platen was maintained at 200 °C (390 °F), and the temperature profile for the mold surface was continuously monitored for 5 hours. After 5 hours, the temperature reached equilibrium. A baseline scan was performed at room temperature, and the second scan was conducted at elevated temperature (after 5 hours) using high precision 3D measurement FARO arm. The arm consists of a FARO Laser Line Probe (LLP), which provides non-contact 3D scanning capabilities. The scans were compared and analyzed using Geomagic Control-X 2018 software for dimensional variation. The experimental setup is shown in Figure 3.5.

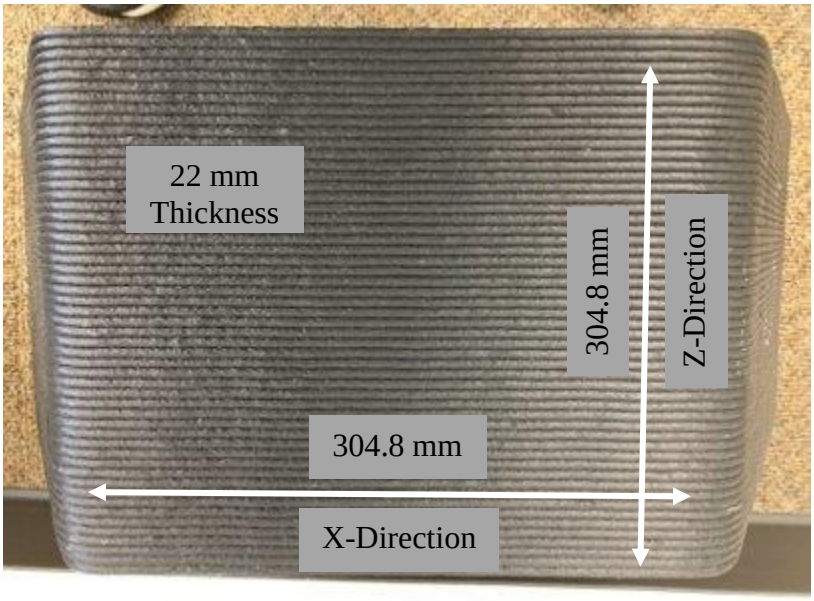

Figure 3.4: Hexagon with 304.8 mm x 304.8 mm x 22 mm dimension. X-direction: along the bead deposition, Z-direction: transverse to the bead deposition

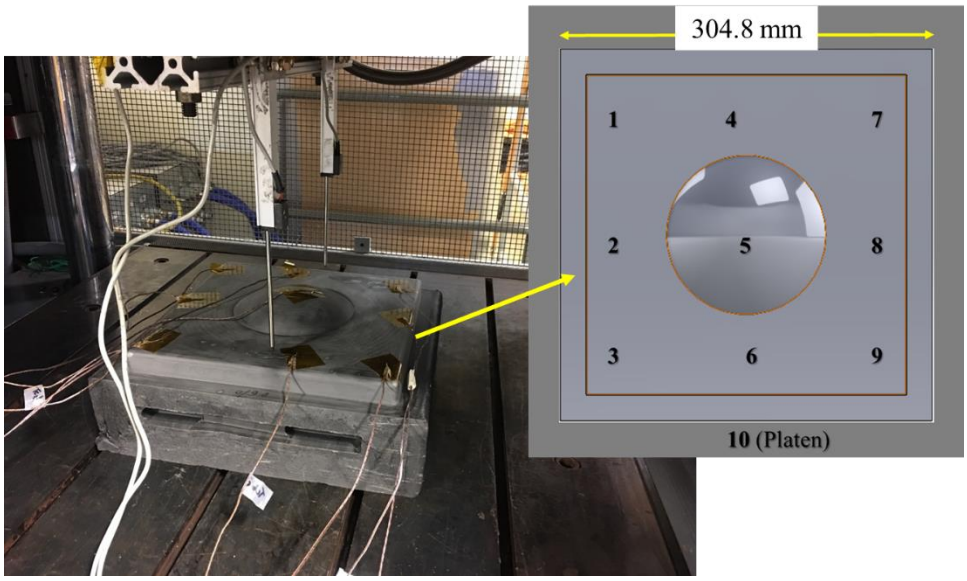

Figure 3.5: Mold placed on the platen (200 °C) and heated through conduction for 5 hours. Position of thermocouples (position 1 to 10) represent the locations where the temperature was recorded.

3.4 Results and Discussion

3.4.1 Mechanical Tests:

The tensile test data is shown in Figure 3.6 and summarized in Table 3.1. The tensile test was performed at room temperature (27 °C) and elevated temperatures (100 °C and 180 °C). These temperatures were selected because the maximum temperature noted by a thermocouple on platen was around 180 °C, and the maximum temperature recorded on the mold surface was around 100 °C (explained in section 3.4.2). These samples showed 42.4 % and 69.0 % reduction in modulus for X-direction after heating from room temperature to 100 °C and 180 °C, respectively. PPS is a semi-crystalline material i.e. contains both amorphous and crystalline structure with a T_g of 85 °C. At temperatures above T_g, the amorphous phase starts to soften causing reduction in strength. Further increase in temperature softens the crystalline structure and affects tensile properties [29].

3.4.1 Heat conduction and warpage:

In this experiment, 9 thermocouples were attached to the top surface of the mold to monitor/record temperature profile. The temperature difference between the three molds was attributed to the infill directions. An extruded material has highly aligned fibers along the deposition direction, and therefore, the conductivity along the deposition direction is expected to be higher than in other directions [30]. Heat transfer in the mold was mainly in the direction from the bottom surface of the mold to the top surface of the mold. When the infill direction was parallel to the heat transfer direction (0° infill), then due to the high conductivity along the heat transfer direction, the top surface held high temperature (i.e., 79.2 °C). When the infill direction was perpendicular to the heat transfer direction (i.e., 90° infill), then due to the low conductivity along the heat transfer

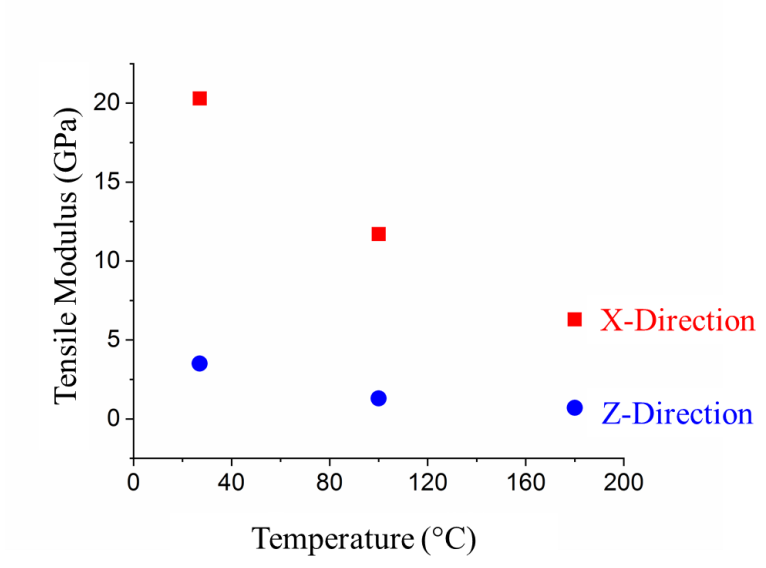

(a)

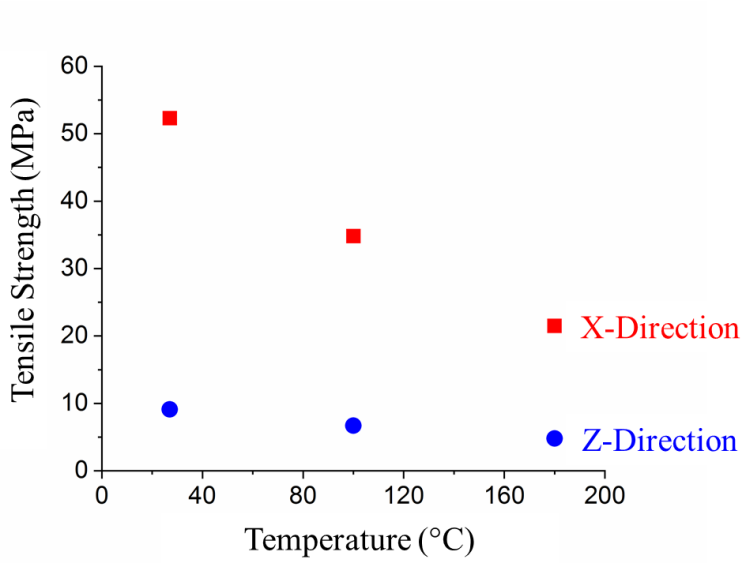

(b)

Figure 3.6: Tensile behavior of 50CF-PPS samples with increase in temperature (a) tensile modulus (b) tensile strength

Table 3.1: Tensile properties of 50CF-PPS at room temperature and high-temperature (100 °C and 180 °C)

Tensile Test	Temperature (°C)					
	Room Temperature (27)		100		180	
	X	Z	X	Z	X	Z
Strength, MPa	52.3 ± 2.97	9.1 ± 0.30	34.8 ± 0.99	6.7 ± 0.32	21.5 ± 0.80	4.8 ± 0.22
Modulus, GPa	20.3 ± 0.32	3.5 ± 0.06	11.7 ± 0.72	1.3 ± 0.08	6.3 ± 0.18	0.7 ± 0.01

Table 3.2: Average top mold surface temperature and total average deflection for different infill patterns.

Sr. No.	Infill Pattern	Avg. Top Surface Temperature (°C)	Total Average Deflection (mm)
1	0°	79.21 ± 6.48	0.314 ± 0.42
2	90°	66.45 ± 5.76	0.363 ± 0.46
3	0°/90°	73.60 ± 4.06	0.329 ± 0.42

direction, the top surface held low temperature (i.e., 66.5 °C). The average surface temperature of the 0°/90° infill pattern mold was recorded as 73.6 °C, in between 0° and 90° infill pattern molds.

The reinforcing fibers aligned along the deposition direction leads to non-uniform expansion of the printed structures [31]. Brenken et al. studied the CTE variation of 50CF-PPS samples for large scale BAAM structures in three principle directions and observed 2×10^{-6} m/(mK), 26.75×10^{-6} m/(mK) and 43.00×10^{-6} m/(mK) in X-, Y-, and Z-directions (representation of each direction is explained later in this section) respectively [32]. To understand the deflection/warpage of the mold due to heating, a 3D digital impression of the mold at room temperature and the elevated temperature was captured using a FARO arm. The scans were then accurately aligned and compared using Geomagic Control-X 2018 software.

The first layer for each mold was printed in the X-Y plane (0° infill in X-direction; 90° infill in Y-direction), and the three-dimensional mold was fabricated by depositing successive layers in Z-direction. The infill pattern in the X-Y plane holds the structure steady irrespective of the infill lines. Therefore, it was observed from Figure 3.7 that all molds were warped in Z-direction only (positive deflection at the edges: green color, and negative deflection at the center: red color).

Figure 3.9 and Table 3.2 shows the 3D deviation analysis of 0°, 90°, and 0°/90° infill pattern molds for high-temperature scan compared to room temperature scan. It was observed that average deflection was +0.385 / -0.244 mm representing total 0.314 mm for 0°, +0.445 / -0.280 mm representing overall 0.363 mm for 90° and +0.397 / -0.262 mm representing total 0.329 mm for 0°/90° molds. Since the deflection (due to heat) in all molds was carried out in Z-direction, and the different infill patterns were presented in the X-Y plane, temperature gradient (the temperature difference between the top and bottom surface of the mold) was the main driving factor for the deviation.

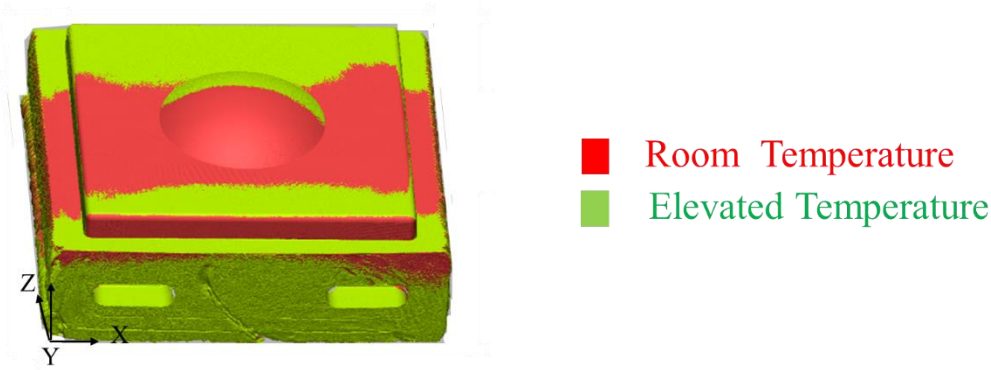

Figure 3.7: Aligned image of mold at room temperature and elevated temperature. All three molds showed similar pattern as warped along the Z-direction. Amount of warpage was different for each mold.

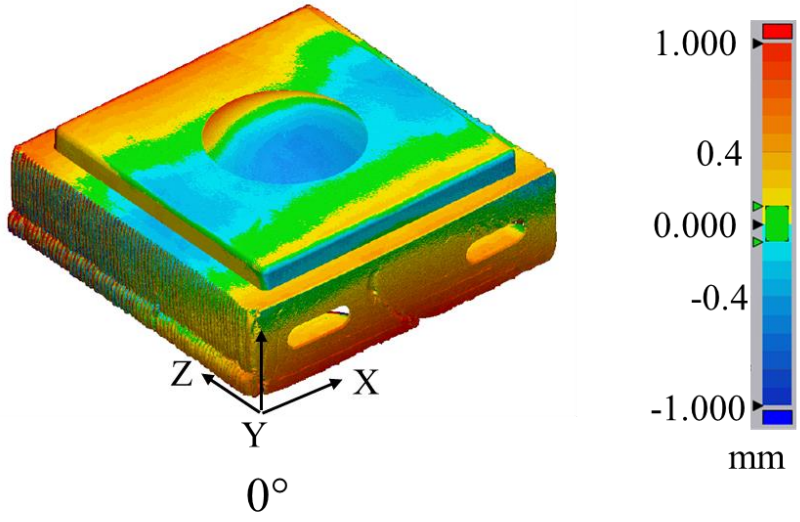

(a)

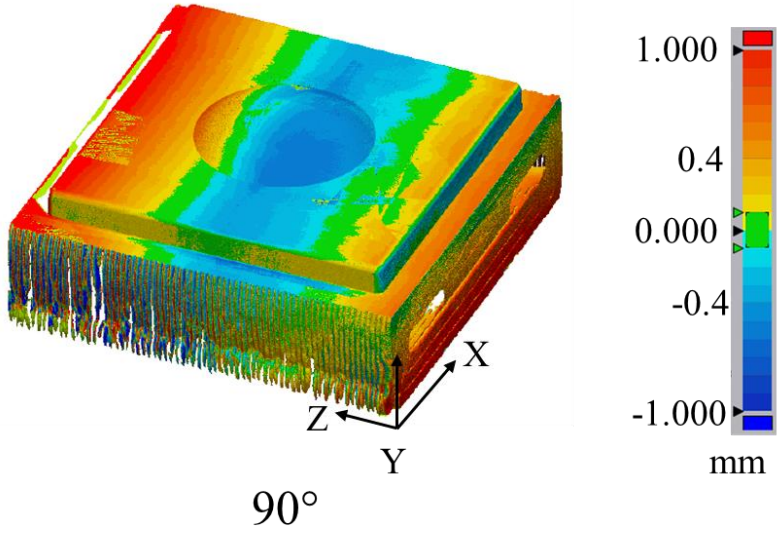

(b)

Figure 3.8: 3D deviation analysis of molds at room temperature and after keeping on heated (200 °C) platen for 5 hours. Total average deflection for (a) 0°: 0.314 mm; (b) 90°: 0.363 mm;

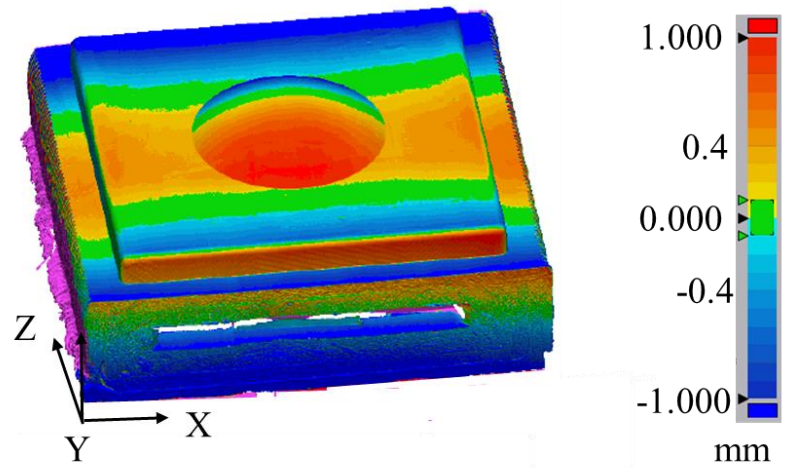

0°/90°

(c)

Figure 3.9: 3D deviation analysis of molds at room temperature and after keeping on heated (200 °C) platen for 5 hours. Total average deflection for (c) 0°/90°: 0.329 mm

The average temperature recorded at the mold top surface for 0°, 0°/90°, and 90°infill pattern mold was 79.2 °C, 73.6 °C, and 66.5 °C respectively. For each experiment, the platen temperature was kept constant (200 °C). Therefore, the temperature gradient between the bottom and top surface of the mold was highest in 90° infill followed by 0°/90° infill and least in 0° infill which correlate with the similar trend of deflection as 0° < 0°/90° < 90°.

Bagsik et al. [33] studied the compression behavior of FDM samples build in vertical (0°) and horizontal (90°) direction. The authors observed that the samples fabricated in vertical direction failed in bucking mode while horizontal direction samples failed due to interlayer shear. Similar results were observed by Motaparti et al. [34]. The failure mechanism of the two orientations is shown in Figure 3.10. Therefore, it can be assumed that a 0°/90° infill pattern has a more stable structure under compression due to alternate layers. The total deviation of 0°/90° infill mold was only 4.8% higher than 0°. Also, 0°/90° infill mold had more uniform heat distribution (standard deviation: ± 4.06) as compared to the other molds. The non-uniform distribution of temperature may result in the uneven curing of composites [35]. Therefore, further efforts were made to characterize the performance of 0°/90° infill mold. A female mold with a 0°/90° infill pattern was fabricated with the same processing conditions explained in section 3.2 and prepared for extrusion compression molding (ECM) operation.

3.5 Extrusion Compression Molding (ECM) with the 0°/90° infill mold

3.5.1 Mold Mounting:

The 0°/90° infill mold was used for the ECM process. The details about ECM are given in [36-38]. The mold was mounted on the compression press, and the platen heating was started. As shown previously (section 3.4.2), the mold warped upon heating.

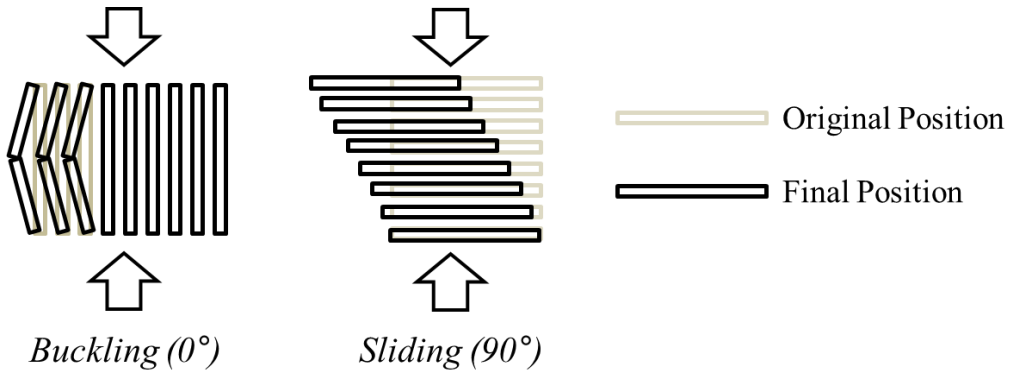

(a) (b)

Figure 3.10: Failure mechanism of AM specimens under compression loading (a) Vertical direction (0°); (b) Horizontal direction (90°) (adapted from [33])

We believe that the mounting clamps constrained free motion of the tool, and resulted in a crack at the center, as shown in Figure 3.11. To further explore the cracking and ways to eliminate it, a high-temperature epoxy 1096 obtained from FiberGlast Development Corporation was used to fill the crack. The 1096 epoxy is a thixotropic system. The two-part epoxy (1096) contains aluminum particles, and it is designed for high-temperature tooling applications. The mold (after filling crack) was mounted back on the press, and heat was applied. After 5 hours, when the temperature reached equilibrium the mold was fixed using mounting clamps. The mold did not show any crack after mounting.

3.5.2 **Parts Fabrication:**

The mold with a 0°/90° infill pattern was used to produce parts using 40% by weight CF reinforced nylon 6 (40CF-PA6) pellets from Celanese using the ECM process. The molten charge was prepared using the Impco B20 plasticator where the heating zones were set to 257 °C, 266 °C, 277 °C, 277 °C and charge size was maintained at 304.8 mm (12”) length × 50.8 mm (2”) diameter (this was the maximum charge size possible with the Impco B20 plasticator). Three layers of McLube 841 releasing agents were applied to the mold surface. The platen temperature was maintained at 121 °C (250 °F), and the temperature at the mold surface was recorded to be in between 66 °C – 71 °C (150 °F – 160 °F).

The hot charge from the plasticator was then placed on the mold, as shown in Figure 3.12 (a), and part was prepared after the application of pressure. Initially, lower pressure was applied as 0.54 MPa (5 tons) and prepared 10 parts.

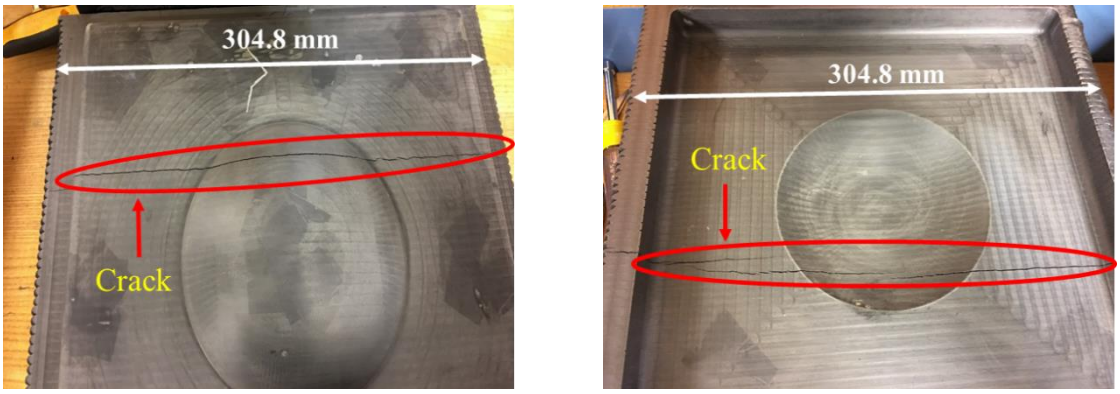

(a) (b)

Figure 3.11: Failure (crack) in the 50CF-PPS additive manufactured mold due to application of pressure on heated warped mold (a) Male mold (b) Female mold

The pressure was increased to 0.86 MPa (8 tons), 1.3 MPa (12 tons), and finally 1.6 MPa (15 tons). Two panels were fabricated using 0.86 MPa and 1.3 MPa each while 6 panels using 1.6 MPa pressure. It can be observed in Figure 3.12 (b) that there were some unfilled regions in the consolidated part. This was due to the limitation of the plasticator to generate a bigger size charge. Tensile samples were extracted according to ASTM D 3039 standard from the flat region of part; average tensile strength of 132.9 ± 11.55 MPa and modulus of 14.3 ± 0.84 GPa was noted. Ning et al. showed that 18-35 % weight of CF reinforced nylon 6 samples modulus varies from 6.5 - 14.7 GPa [39]. From this, it can be concluded that the parts fabricated using AM mold were well consolidated.

3.5.3 **Mold Degradation:**

A total of 20 parts were fabricated using the ECM process to determine the durability of the mold. A 3D digital impression of the mold was captured by a laser scanner before and after 20 parts were fabricated. The two scans were aligned and compared using Geomagic Control X-2018 software. Figure 3.13 shows that the deformation occurred in the mold due to the manufacturing of 20 parts using 40CF-PA6. The average degradation of + 0.076 mm / – 0.093 mm was recorded. It can be noticed that the maximum degradation was observed along the epoxy region (blue color). This degradation was caused due to the flow of the charge (40CF-PA6) at a high temperature, which created friction and damaged epoxy region. The rest of the mold surface showed very minimal (yellow color) or no degradation (green color). Therefore, it can be concluded that 50CF-PPS material can be a good alternative for composite tooling ECM operation.

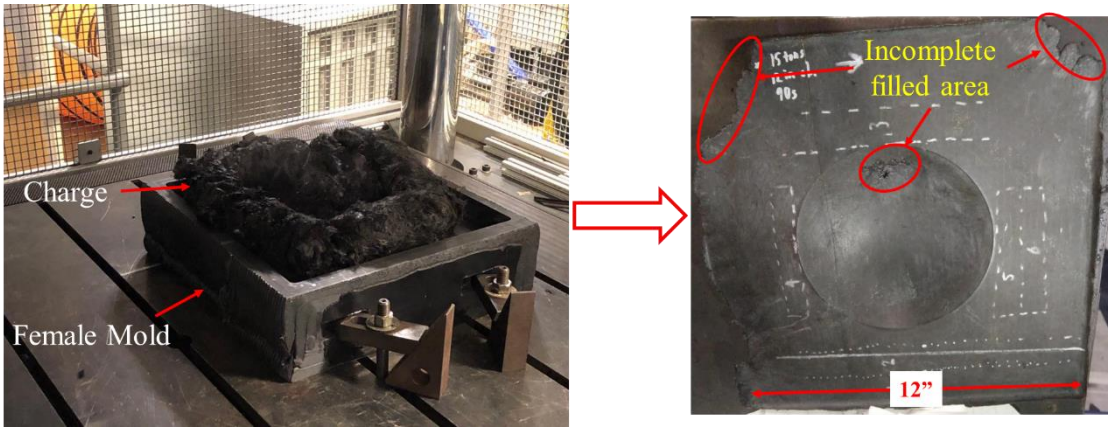

(a) (b)

Figure 3.12: (a) Location of charge placed in the BAAM printed mold (b) the representative consolidated part of 40CF-PA6. The unfilled region on the consolidated part due to the limitation of the plasticator to generate a bigger charge (Maximum charge length produced by plasticator was 304.8 mm).

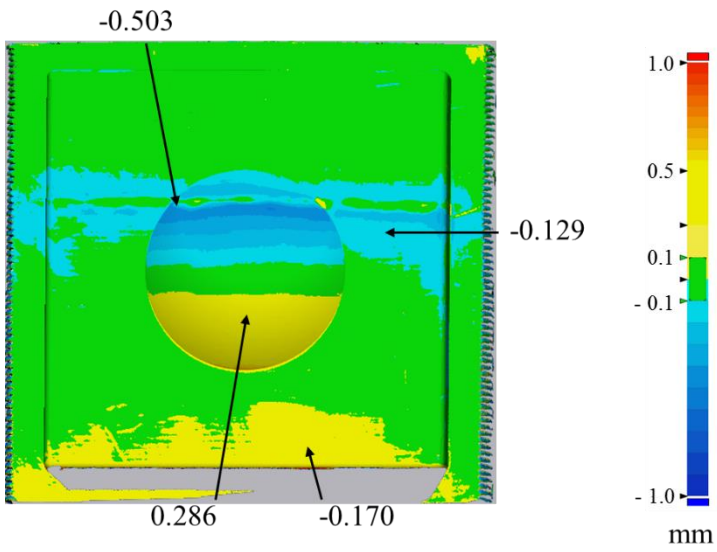

Figure 3.13: Deviation analysis of the two scans before and after 20 parts fabrications. Maximum deformation was observed at the 1096 epoxy region (blue area).

3.6 FINITE ELEMENT ANALYSIS (FEA)

FEA was performed on the male molds with three different infill geometries, as shown in Figure 3.3. A commercial FEA tool, Abaqus 2018, was used for computational thermal analysis. The geometric model is discretized into 28.6k elements, including 13.8k tetrahedron elements and 14.8k hexahedron elements. The element size in the z-direction is 5.08 mm, which is the same as the layer height (= slicing thickness) of the 3D-printed mold. The average element size in x- and y-direction is 14 mm. A linear interpolation function is used for both types of elements. The analysis is for thermal simulation without deformation simulation, and therefore, shear locking is not a concern in this study.

The analysis was performed with two steps: AM process simulation and service loading simulation. The purpose of the first step (AM process) is to assign the directionality of the anisotropic material properties in every element. The fibers in a printed bead are highly aligned along the deposition direction, and therefore, the anisotropic thermal properties and mechanical properties of the printed bead have directionality along the deposition direction. The toolpath direction varies location by location in the entire printed part, as shown in Figure 3.3. Therefore, in the FEA model, the directionality of the anisotropic material properties of each element should be assigned based on the local toolpath direction. During the AM process simulation in Abaqus, the local toolpath directions are assigned in the FEA elements. The directionality information is transferred to the next step simulation.

The second step is a service loading simulation. The printed mold was placed on a heated platen of a hydraulic compression press. The temperature of the mold was gradually increased and reach a steady state. The goal of the service loading simulation is to predict the surface temperature of the mold at a steady state. The prediction was performed via a thermal FEA simulation with the

following three constitutive relations: thermal conduction, thermal convection, and thermal radiation. For thermal conduction, the three-dimensional Fourier's law was used with the orthotropic conductivity coefficients ($\kappa_1, \kappa_2, \kappa_3$). For thermal convection, Newton's law of cooling was used with the convection coefficient (h). For thermal radiation, the Stefan-Boltzmann law was used with the emissivity coefficient (ϵ). The coefficients for heat transfer parameters are listed in Table *3.3*.

The boundary conditions are shown in Figure 3.14. The environment temperature was set to 30 °C, and the mold initially had a uniform temperature of 30 °C. During experiment, the temperature of the platen was maintained at 200 °C. However, the bottom surface temperature was set to 160 °C throughout the simulation because heat loss due to open environment and the platen has slots for mounting mold which reduces the overall heating contact area. The convection and radiation were applied to the surface of the mold except for the bottom surface. As the simulation proceeded, the temperature increased from the bottom of the mold, and the heat gradually propagated to the top surface of the mold.

It should be addressed that the current simulations have the following limitations. First, the simulation considers only the heat transfer behavior in the mold and ignores a mechanical deformation. As explained previously, the warpage of the mold creates a gap between the heated platen and the bottom surface of the mold, and the amount of the gap was different among the three molds. Due to the gap, the bottom surface of the mold had a non-uniform temperature distribution. Second, the simulation assumes an ideal case of infill printing in which the deposited beads have a perfect bonding. In actual large-scale printing, the deposited beads with high temperature (extrusion temperature of 337°C), which were initially bonded to each other, might

Table 3.3: Coefficients used in the thermal simulation [40]

Constitutive Relation	Coefficient	Value	Unit
Conduction	κ_1	1.472	W/(m·K)
	κ_2	1.287	W/(m·K)
	κ_3	0.4528	W/(m·K)
Convection	h	5.0	W/(m^2·K)
Radiation	ϵ	0.9	dimensionless

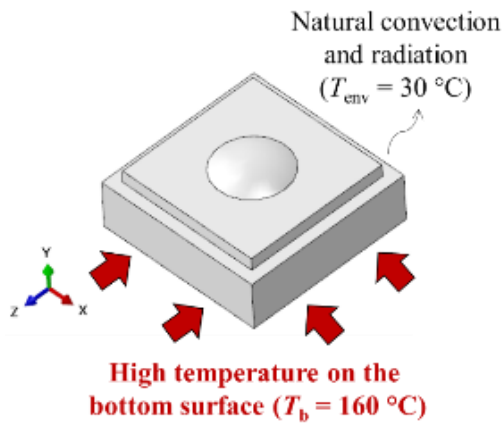

Figure 3.14: Boundary conditions for service load simulation (thermal simulation). Bottom temperature: 160 °C and ambient temperature: 30°C.

get separated as they shrink during cooling. The shrinkage of the printed beads can create a gap between infill lines, which can decrease the conductivity across the infill lines.

We have performed the thermal simulations for the three molds, as shown in Figure 3.3, and the temperature fields of the top surfaces from the three molds are shown in Figure 3.15. The high temperature near the interface circular line between the dome surface and top flat surface was recorded. The center area had high temperature because of the heat loss on the surfaces at the four sides of the mold. However, because the dome surface had longer distance from the bottom surface (heat source) (distance varies along the dome surface: 127mm - 152.4 mm) than the top flat surface of the mold from the bottom surface (127 mm), the conduction to the dome surface becomes less effective as compared to the conduction to the top flat surface. Therefore, a large area near the center has a high temperature except for the dome surface.

At the interface line between the dome surface and the top flat surface, the mold with 0° infill had the highest temperature, and the mold with 90° infill had the lowest temperature. The temperature of the mold with 0°/90° infill was in between the temperatures of 0° infill mold and 90° infill mold. The average temperatures on the surface of the interest (see Figure 3.16) were 79.3 °C, 77.7 °C, and 78.4 °C for 0° infill, 90° infill, and 0°/90° infill molds, respectively. Therefore, the overall trend for the average surface temperature was 0° > 0°/90° > 90°, was similar to the experimental results. The mold with 0°/90° infill lines has a more stable structure due to the alternate layers, as explained in section 4.2. Therefore, efforts were made to increase the thermal conductivity of the mold with a 0°/90° infill pattern. The above study (experimental as well as simulation) was performed based on the 3 perimeters as shown in Figure 3.3.

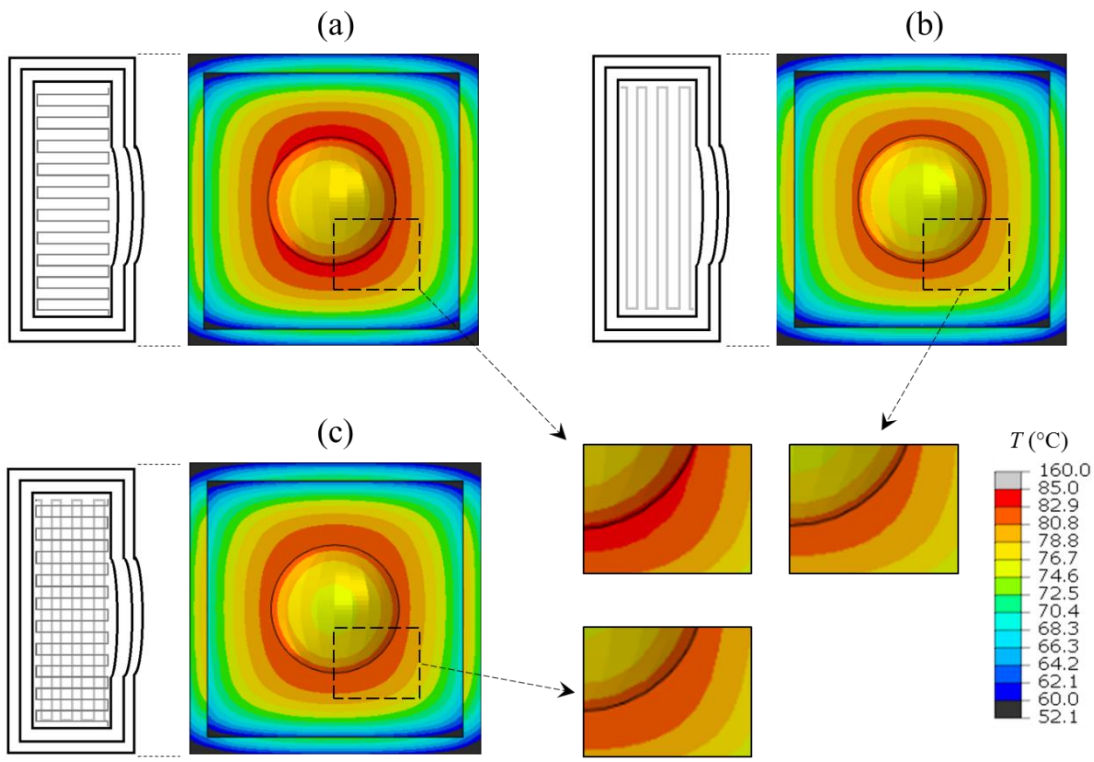

Figure 3.15: Temperature profile of the top surface of the three molds. (a) Mold with 0° infill, (b) Mold with 90° infill, (c) Mold with 0°/90° infill

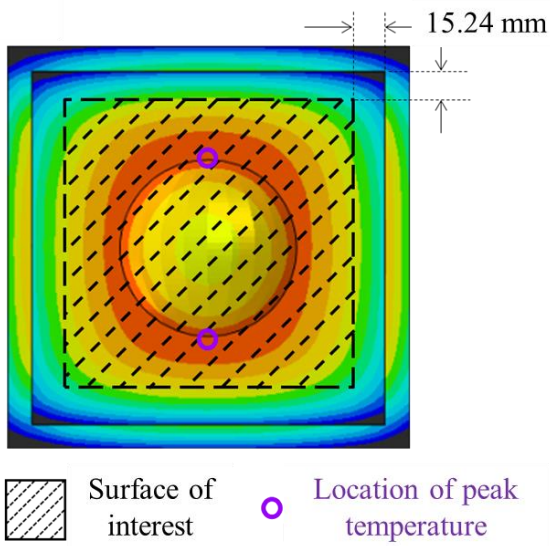

Figure 3.16: Surface of interest/part molding area (shaded area) and the location of peak temperature (purple circle). Average surface temperature for each mold was measured in the shaded area.

FEA was conducted to understand the effect of 1 perimeter on the thermal conductivity of the mold with a 0°/90° infill pattern. The difference in temperature distribution at the top surface between one and three perimeters is shown in Figure 3.17. The average temperatures on the surface of the interest (see Figure 3.16) are 78.4 °C and 79.0 °C for 3 perimeters and 1 perimeter respectively, for 0°/90° infill molds. The increase of temperature in 1 perimeter mold was due to the increase of layers parallel to the heat conduction (0° layers). The effect on the strength of the mold due to the change in the number of perimeters was out of scope for this study and will be analyzed later.

3.7 Conclusions:

EDF-AM process was used to fabricate dome-shaped male molds with different infill pattern namely; 0°, 90°, and 0°/90°. The thermal conductivity had a direct relationship with the carbon fiber orientation, which was confirmed as the average top surface temperature for 0° > 0°/90° > 90°. FEA showed that the average top surface temperature of 0°/90° infill mold could be increased by reducing the number of perimeters. The mold showed a high level of durability (average degradation: + 0.076 mm / – 0.093 mm) for the ECM process when scanned using a 3D laser scanner. The tensile strength and modulus of the 40CF-PA6 part were 132.9 MPa and 14.3 GPa, respectively, fabricated using 50CF-PPS EDF-AM mold.

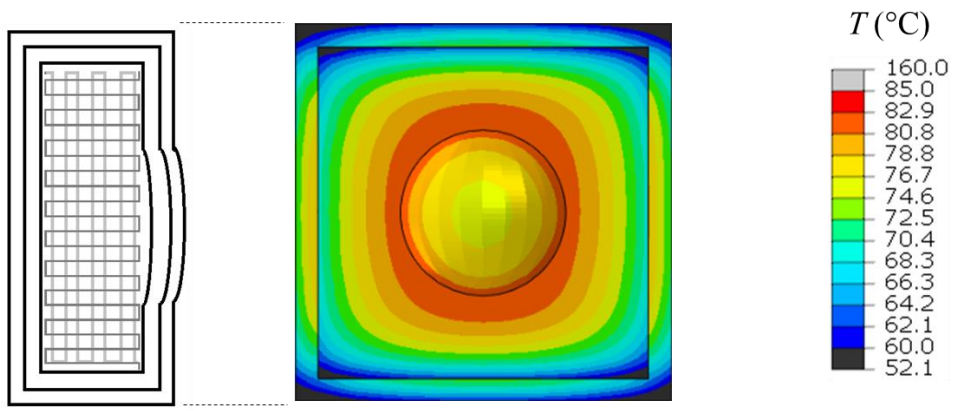

(a)

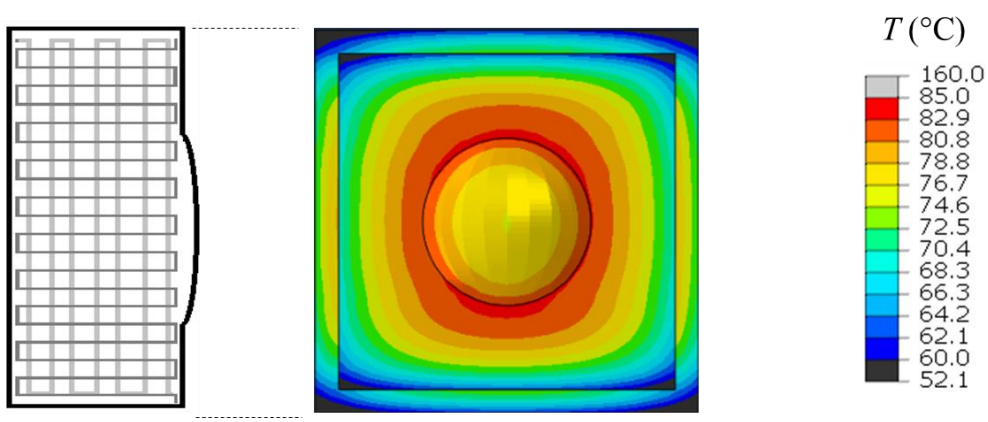

(b)

Figure 3.17: Temperature profile of the top surface of 50CF-PPS AM mold (a) 3 perimeters (b) 1 perimeter

REFERENCES

1. Lanz, R.W., S.N. Melkote, and M.A.J.J.o.M.P.T. Kotnis, *Machinability of rapid tooling composite board.* 2002. **127**(2): p. 242-245.
2. Canis, B. *The tool and die industry: Contribution to US manufacturing and federal policy considerations*. in *CRS Report for congress*. 2012.
3. Cotteleer, M., M. Neier, and J.J.D.R. Crane, *3D opportunity in tooling: Additive manufacturing shapes the future.* 2014.
4. Tekinalp, H.L., et al., *Highly oriented carbon fiber–polymer composites via additive manufacturing.* 2014. **105**: p. 144-150.
5. Love, L.J., et al., *The importance of carbon fiber to polymer additive manufacturing.* 2014. **29**(17): p. 1893-1898.
6. Richardson, B.S., et al., *Enabling Technologies for Medium Additive Manufacturing (MAAM)*. 2018, Oak Ridge National Lab.(ORNL), Oak Ridge, TN (United States).
7. Hassen, A.A., et al. *Additive manufacturing of composite tooling using high temperature thermoplastic materials*. in *SAMPE Conference Proceedings, Long Beach, CA, May*. 2016.
8. Duty, C.E., et al., *Structure and mechanical behavior of Big Area Additive Manufacturing (BAAM) materials.* 2017. **23**(1): p. 181-189.
9. Pradere, C. and C.J.C. Sauder, *Transverse and longitudinal coefficient of thermal expansion of carbon fibers at high temperatures (300–2500 K).* 2008. **46**(14): p. 1874-1884.
10. Savage, G., *Applications of Carbon-carbon composites*, in *Carbon-Carbon Composites*. 1993, Springer. p. 323-359.

11. Gabrion, X., et al., *About the thermomechanical behaviour of a carbon fibre reinforced high-temperature thermoplastic composite.* 2016. **95**: p. 386-394.

12. Vieille, B., L.J.C.S. Taleb, and Technology, *About the influence of temperature and matrix ductility on the behavior of carbon woven-ply PPS or epoxy laminates: Notched and unnotched laminates.* 2011. **71**(7): p. 998-1007.

13. Walther, B.M., *An investigation of the tensile strength and stiffness of unidirectional polymer-matrix, carbon-fiber composites under the influence of elevated temperatures*. 1998, Virginia Tech.

14. Mahieux, C., C.J.C.P.A.A.S. Scheurer, and Manufacturing, *Elevated temperature bending stress rupture behavior AS4/APC-2 and comparison with AS4/PPS literature data.* 2002. **33**(7): p. 935-938.

15. Karadeniz, Z.H. and D.J.C.S. Kumlutas, *A numerical study on the coefficients of thermal expansion of fiber reinforced composite materials.* 2007. **78**(1): p. 1-10.

16. Islam, R., S.-G. Sjölind, and A.J.J.o.c.m. Pramila, *Finite element analysis of linear thermal expansion coefficients of unidirectional cracked composites.* 2001. **35**(19): p. 1762-1776.

17. Ran, Z., et al., *Determination of thermal expansion coefficients for unidirectional fiber-reinforced composites.* 2014. **27**(5): p. 1180-1187.

18. Kulkarni, R. and O.J.J.o.C.M. Ochoa, *Transverse and longitudinal CTE measurements of carbon fibers and their impact on interfacial residual stresses in composites.* 2006. **40**(8): p. 733-754.

19. Kumar, V., et al., *Replacing Metal-Based Lightning Strike Protection Layer of CFRPS by 3D Printed Electronically Conductive Polymer Layer*. 2019, Oak Ridge National Lab.(ORNL), Oak Ridge, TN (United States).

20. Tezvergil, A., L.V. Lassila, and P.K.J.D.M. Vallittu, *The effect of fiber orientation on the thermal expansion coefficients of fiber-reinforced composites.* 2003. **19**(6): p. 471-477.

21. Chesser, P., et al., *Extrusion control for high quality printing on Big Area Additive Manufacturing (BAAM) systems.* 2019. **28**: p. 445-455.

22. Brenken, B., et al., *Fused filament fabrication of fiber-reinforced polymers: A review.* Additive Manufacturing, 2018. **21**: p. 1-16.

23. Yeole, P., et al., *Characterization of textile-grade carbon fiber polypropylene composites.* Polymers and Polymer Composites, 2020: p. 0967391120930109.

24. Wang, S., et al., *Compressive and flexural behavior of carbon fiber-reinforced PPS composites at elevated temperature.* Mechanics of Advanced Materials and Structures, 2020. **27**(4): p. 286-294.

25. Mishra, S.B. and S.S. Mahapatra. *Improvement in tensile strength of FDM built parts by parametric control*. in *Applied Mechanics and Materials*. 2014. Trans Tech Publ.

26. Vaezi, M., S.J.V. Yang, and P. Prototyping, *Extrusion-based additive manufacturing of PEEK for biomedical applications.* 2015. **10**(3): p. 123-135.

27. Popescu, D., et al., *FDM process parameters influence over the mechanical properties of polymer specimens: A review.* 2018. **69**: p. 157-166.

28. Zaldivar, R., et al., *Influence of processing and orientation print effects on the mechanical and thermal behavior of 3D-Printed ULTEM® 9085 Material.* 2017. **13**: p. 71-80.

29. Garrell, M.G., et al., *Mechanical properties of polyphenylene-sulfide (PPS) bonded Nd–Fe–B permanent magnets.* 2003. **359**(1-2): p. 375-383.

30. Ralph B. Dinwiddie, V.K., John M. Lindahl, Seokpum Kim, Pritesh Yeole, and L.J.L. Chad Duty, Ahmed Arabi Hassen, *Specific heat capacity and anisotropic thermal conductivity*

of additively manufactured carbon-fiber-reinforced thermoplastics; abs + 20% cf, pps + 50% cf and ppsu + 25% cf. . 2020: Journal of Composite Science and Technology - Under Review.

31. Yeole, P., et al., *Mechanical Characterization of High-Temperature Carbon Fiber-Polyphenylene Sulfide Composites for Large Area Extrusion Deposition Additive Manufacturing.* Additive Manufacturing, 2020: p. 101255.

32. Brenken, B., *Extrusion Deposition Additive Manufacturing of Fiber Reinforced Semi-Crystalline Polymers*. 2017, Purdue University.

33. Bagsik, A., V. Schöppner, and E. Klemp. *FDM part quality manufactured with Ultem* 9085*. in *14th international scientific conference on polymeric materials*. 2010.

34. Motaparti, K.P., *Effect of build parameters on mechanical properties of ultem 9085 parts by fused deposition modeling.* 2016.

35. Wang, Q., et al., *Design optimization of molds for autoclave process of composite manufacturing.* 2017. **36**(21): p. 1564-1576.

36. Yeole, P., H. Ning, and A.A.J.J.o.T.C.M. Hassen, *Development and characterization of a polypropylene matrix composite and aluminum hybrid material.* 2019: p. 0892705719843974.

37. Vaidya, U., *Composites for automotive, truck and mass transit: materials, design, manufacturing*. 2011: DEStech Publications, Inc.

38. Yeole, P., *Fiber metal laminate with thickness reinforcement*. 2015, The University of Alabama at Birmingham.

39. Ning, H., et al., *A review of Long fibre thermoplastic (LFT) composites.* International Materials Reviews, 2020. **65**(3): p. 164-188.

40. Seokpum Kim, P.Y., Ahmed Hassen, Vipin Kumar, Vlastimil Kunc, Uday Vaidya, *Effect of Infill Patterns on Heating for Additively Manufactured Compression Molds*, in *SAMPE Conference Proceeding*. 2020: Seattle, WA.

4 CHAPTER

IMPROVE DURABILITY AND SURFACE QUALITY OF ADDITIVELY MANUFACTURED MOLDS USING CARBON FIBER PREPREG

ABSTRACT

Hybrid tooling is an emerging concept introduced in the aerospace industries to reduce weight and cost of traditional tools. A hybrid tool features a skin which provide desired surface quality, durability and a low-density substrate to reduce weight of the mold. The Big Area Additive Manufacturing (BAAM) technology permits rapid production of thermoplastic polymer intensive large-scale structures. The present study features a carbon fiber reinforced polyphenylene sulfide (CF-PPS) substrate fabricated using Oak Ridge National Laboratory's (ORNL) BAAM system. Carbon fiber-bismaleimide (CF-BMI) prepreg skin was then bonded to the BAAM tool through high-pressure autoclave molding. Process optimization was conducted to improve the bonding between CF-PPS and CF-BMI (transverse tensile strength increased from 0.54 MPa to 4.8 MPa). Durability of the mold was demonstrated from fabricating seven (7) carbon fiber-Huntsman epoxy hand lay-up parts off the mold.

Keywords: hybrid tooling, big area additive manufacturing, autoclave molding, transverse tensile strength, mold degradation

4.1 INTRODUCTION

Autoclave processing is the preferred method to consolidate prepreg parts in aerospace applications. An autoclave is commonly used for its ability to form composites in complex geometries while maintaining low void content. Carbon fiber composites has a low coefficient of thermal expansion (CTE) about 2.9 - 3.7 µm/m°C [1, 2]. The CTE of Invar (face-centered cubic structure of iron and 36% nickel alloy) is very low, over a wide range of temperatures (0°C - 100°C: 1.5 µm/m°C [3]) [4]. The austenitic crystal structure of Invar makes it durable to withstand repeated autoclave curing cycles without creating cyclic stresses [1]. Therefore, Invar is an ideal material for composite tooling due to matched CTE and excellent durability [5]. However, Invar has low yield strength, low wear and corrosion resistance at elevated temperatures as well as high density (8.1 g/cc) [6].

Aerospace industries are considering carbon fiber (CF) tooling for autoclave processing, as an alternative option to Invar. Some of the requirements for CF tooling include lighter than Invar, sustain more than 500 autoclave cycles, and possess glass transition temperature greater than 204 °C. The tool also should be cost-effective, ultraviolet (UV) resistant, maintain a high level of dimensional integrity and stability [7].

With recent developments in polymer additive technology, it is now possible to create large, additively manufactured tools with high dimensional accuracy [8-13]. This is also referred to as Big Area Additive Manufacturing (BAAM) [14]. BAAM consists of a single screw extruder mounted on a three-axis gantry system. The BAAM system can deposit material at 45 kg/hr rate in a working area of 6 m x 2.5 m x 1.8 m [8]. The size of the polymer bead in BAAM is large (typically width 13.97 mm × height 5.08 mm [15]) which leads to grooved and/or ribbed surface topography. Therefore, the surface finish requirement is always challenging for large-scale AM

tools, without additional post-processing. There are two approaches to address this problem- (a) manufacture the mold slightly larger (2.54 mm) than the actual dimensions then through subtractive manufacturing remove the excess material to the exact part geometry. With this approach, Oak Ridge National Laboratory (ORNL), in collaboration with The Boeing Company, produced AM autoclave tools from 50 % by weight carbon fiber reinforced polyphenylene sulfide (50CF-PPS) and 25 % by weight carbon fiber reinforced polyphenylsulfone (25CF-PPSU) for autoclave processing (material: CF reinforced epoxy (CF-epoxy) prepreg, temperature: 176.6 °C, pressure: 620 kPa for 2 hours) [8]. It was observed that the deformation of the mold working area (i.e. composite lay-up area) was less than 0.1 mm for both tools. There are some drawbacks to this approach as (i) the subtractive process leads to material waste, (ii) AM components possess inter-layer and intra-layer porosity [16] which result in the possibility of exposing voids during machining; (b) alternative approach is to manufacture the mold slightly undersized and add layer(s) of coating to achieve the desired mold geometry. This research is focused on the second approach. Hybrid tooling is a new concept introduced to reduce the weight of the conventional Invar tool [7]. The hybrid tool incorporates a thin layer of Invar as a skin layer over a composite back structure (substrate). This provides the desired surface quality, takes advantage of the durability of Invar, and reduces weight due to the low-density composite substrate [17]. It was observed that the durability of a hybrid tool is better than a composite tool [7]. Janicki Industries (Sedro-Woolley, WA, USA), and Hexcel (Dublin, CA, USA)) researched carbon fiber-bismaleimide (CF-BMI) composite and observed it to be a suitable replacement for Invar. CF-BMI can withstand autoclave cycling up to 177 °C and can survive 500 cycles [18]. CF-BMI composites offer exceptional properties like fracture toughness, fatigue life, damage tolerance compared to CF-epoxy [19, 20]. CF-BMI composites find applications in space structures, military, and composite tooling where

robust and high-temperature performance is required. BMI resin has high glass transition temperature (230-380 °C), low flammability and stable electrical properties [20, 21].

In this research, 50CF-PPS pellets were used to manufacture substrate using the BAAM system, located at the Manufacturing Demonstration Facility, Oak Ridge National Laboratory. CF-BMI prepreg was procured from Raptor Resin Inc. Contact angle measurement was performed to analyze bonding capability between 50CF-PPS and CF-BMI. Various steps were followed to improve bonding between substrate and skin. An autoclave (ASC Econoclave™ Model EC2X3-200P800F) located at University of Dayton Research Institute (UDRI), Dayton, Ohio was used to bond CF-BMI prepreg on the 50CF-PPS AM mold surface. The degradation of the mold was analyzed and compared using the Faro Arm 3D imaging scanner and Geomagic Control-X 2018 software after manufacturing 7 CF-epoxy parts using hand lay-up.

4.2 MATERIALS AND METHODS

Twin screw compounded 50CF-PPS pellets were received from Techmer PM, Clinton, Tennessee. The BAAM system was used to fabricate the mold of 355.6 mm × 355.6 mm × 203.2 mm (14” × 14” × 8”) dimensions, as shown in Figure 4.1. The BAAM extruder had 5 heating zones to melt the polymer. The temperature profile for 50CF-PPS printing was zone 1: 305 °C, zone 2: 321 °C, zone 3: 326 °C, zone 4: 337 °C, and zone 5 (tip): 337 °C. The mold was printed on an acrylonitrile butadiene styrene (ABS) sheet, which was kept at 110 °C. The beads had dimension 13.97 mm width, 5.08 mm height, printed using a 10.16 mm nozzle under an inert environment. CF-BMI prepreg was received from Raptor Resins Inc.

Figure 4.1: 50CF-PPS: 355.6 mm × 355.6 mm × 203.2 mm (14” × 14” × 8”) mold substrate, printed with the BAAM system with 0/90 infill pattern. Printing parameters:- bead width: 13.97 mm, bead height: 5.08 mm.

Flat plaques were prepared to study the bonding characteristic between 50CF-PPS BAAM and CF-BMI prepreg. Before proceeding to autoclave molding, to save cost and time, a few trials were conducted with compression molding the CF-BMI prepreg skin to the 50CF-PPS AM substrate. A flat panel was manufactured by BAAM, as shown in Figure 4.2 (a), and three layers of prepreg were bonded to it using a Carver hydraulic compression press (Model number: 3895.41E1000) with the following processing conditions - compression molding at 190 °C (375 °F) for 2 hours with 552 kPa (80 psi) pressure and post cure 210 °C (410 °F) for 4 hours. A representative panel is shown in Figure 4.2 (b), from here on these samples will be referred as baseline.

Mechanical tests were performed to understand the bond strength between the prepreg skin and AM substrate. Through-the-thickness transverse tensile test was performed according to ASTM D7291 standard. Five specimens with an average diameter of 25.4 mm were mounted in 50 kN test resource frame and pulled at 0.1 mm/min loading rate. ASTM D5528 was used to performed fracture toughness, using a 50 kN load cell test resource frame. Crack initiation layer was not included in fracture toughness because it was assumed that the interface between prepreg and AM was the weakest section, and crack would propagate through the intersection [22]. Specimens of 25.3 mm width and 130 mm length were cut and loaded at 2 mm/min rate to perform fracture toughness test.

4.3 RESULTS AND DISCUSSIONS

The results and discussion are structured in two sections, called Phase I and Phase II respectively. The Phase I results provide preliminary understanding of the bond strength between the skin and the substrate.

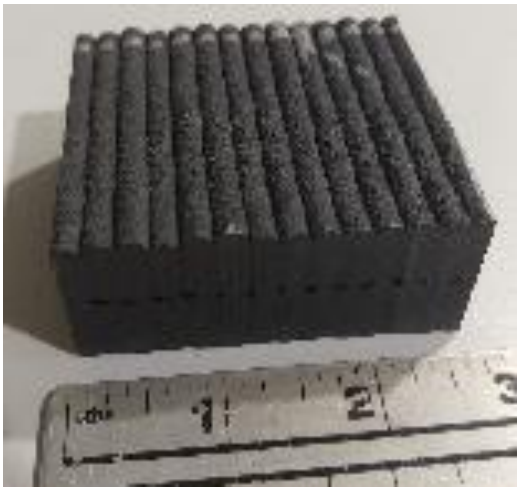

(a)

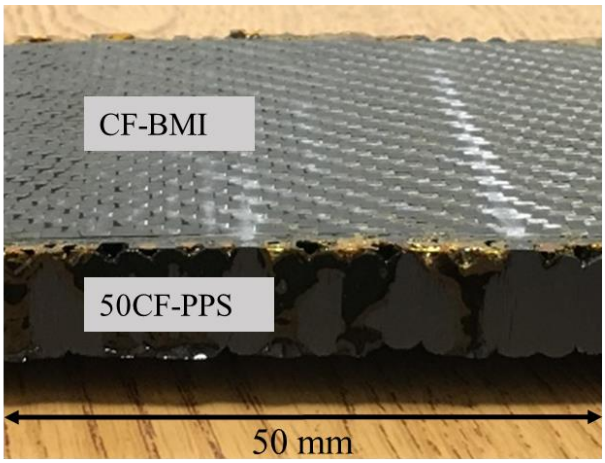

(b)

Figure 4.2: (a) Flat 50CF-PPS BAAM plaque, (b) CF-BMI prepreg bonded on the 50CF-PPS substrate using hydraulic compression press (model number: 3895.41E1000). Processing conditions: temperature – 190 °C, pressure – 552 kPa, dwell time – 2 hours.

Based on these, phase 2 focused on optimization and enhancement of the interface. *Phase I studies:* The baseline samples were analyzed for through-thickness transverse tensile, and fracture toughness tests. These results are summarized in Table 4.1. These properties directly relate to the bond strength of CF-BMI to the AM beaded substrate for the above-mentioned processing conditions. The average transverse tensile strength was 0.54 MPa before delamination occurred. It was also observed that 0.27 N/mm fracture toughness was required to initiate and propagate crack through the bond line between the CF-BMI prepreg and AM substrate. It can be observed from Figure 4.3 (b), the crack was initiated at the intersection; however, propagated through the AM section due to weak Z-strength (layer-to-layer bonding) in the AM substrate [16]. It can be concluded from Figure 4.3 (a) that the BMI resin did not flow inside the groove between the beads. Therefore, further means for improvement of the bond strength between the AM substrate and the CF-BMI skin was needed.

4.4 CONTACT ANGLE

Contact angle measurement was performed to understand the bond compatibility between CF-BMI prepreg and 50CF-PPS AM surfaces. The contact angle defines the wettability of solid surfaces i.e., hydrophobic or hydrophilic behavior of the material [23]. In this study, the Wilhelmy plate method was used to measure the contact angle of the CF-BMI and 50CF-PPS AM surfaces. The details about the Wilhemy test are given in [24]. This is a quasi-static angle measurement technique because the contact angle is measured by the force required to immerge the specimen into a liquid, as shown in Figure 4.4. Equation 1 was used to calculate the contact angle between a liquid and specimen

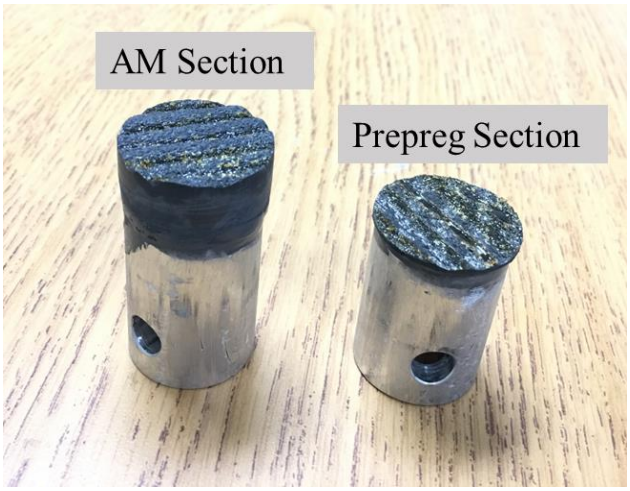

(a)

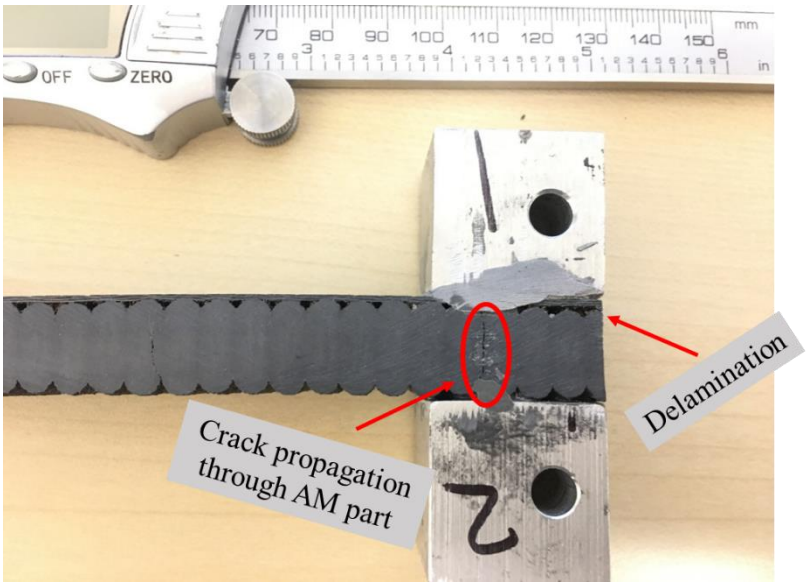

(b)

Figure 4.3: Failed baseline specimen of 50CF-PPS and CF-BMI flat plaque (a) Through thickness transverse tensile test - resin did not flow inside the gaps between the beads, (b) Fracture toughness - failure started at the intersection between AM and prepreg; however, propagated through AM Z-interlayers.

Table 4.1: Mechanical test data for baseline specimens

Test	Average	Standard Deviation
Transverse tensile test (Pa)	0.54	0.14
Fracture Toughness (N/mm)	0.27	0.03

$$cos\,\theta = {(\Delta F + V_{im}(\rho_L - \rho_{air}\mathbb{g})}/{(P_i\gamma_L^{Tot})} \qquad \text{Equation 2}$$

Where,

ΔF – Difference between weight measure in air and partially submerged in liquid, g

P_i – Perimeter of the specimen, mm

γ_L^{Tot} – Surface energy of a liquid, mm J/mm^2

ρ_L – Density of liquid, g/mm^3

ρ_{air} – Air density, g/mm^3

$\mathbb{g}$ – Gravitational force, mm/seconds^2

θ – Contact angle, º

In principle, the contact angle observed when specimen advances into the liquid (advancing angle) should be the same as during its receding (receding angle). However, Kwok et al. [25] showed that a hysteresis loop could be possible due to the physical roughness or chemical heterogeneity of the sample. Studies by Oss et al. and Volpe et al. [26, 27] suggest that advancing angle is more reliable for the surface energy measurement than receding angle.

In this work, the contact angle of representative samples as 50CF-PPS BAAM printed single bead and CF-BMI prepreg was measured. Distilled water was used as a probe liquid. Thermo Cahn instrument (WinDCA software) with DCS microbalance was used to conduct the test. The beaker containing water was kept on the balance stage, whose up-down movement was controlled using a stepper motor. The specimen was attached to the micro-balance then immersed (5 mm of depth) in the water at a speed of 20 µm/s, slow speed ensured quasi-equilibrium condition. The weight of

the specimen was continuously monitored during the advancing and receding motion of the stage. The test was performed at room temperature.

Figure 4.5 shows the hysteresis loop observed due to the difference between advancing and receding contact angle measurement for CF-BMI (blue curve) and 50CF-PPS (red curve). Hysteresis is usually considered as a positive sign because it indicates partial or complete wetting of the surface [28]. The average advancing and receding contact angles for 50CF-PPS were 80° and 42°, and for CF-BMI were 95° and 63°, respectively. As explained earlier, the advancing angle is a preferred indicator of surface wettability. The principle of contact angle states that the higher the contact angle between the liquid and solid, the lower the wettability between surfaces [29]. In the current research, the contact angle CF-BMI prepreg was 95° indicating poor wetting/bonding characteristics; however, CF-PPS showed 80° representing mild wetting properties.

The transverse tensile test confirmed these results, as the bond strength was only 0.54 MPa. Morrison et al. [30] studied the strengthening mechanism of bonding between substrate and skin for hybrid tooling. Authors observed that the 5.4 MPa bonding strength was observed between substrate (ceramic matrix composite) and skin (ceramic coating). Therefore, efforts were made to improve the bonding and following section shows the steps implemented to obtain maximum delamination strength.

4.5 *Phase II Studies* - PROCESS OPTIMZATION TO IMPROVE BONDING BETWEEN CF-BMI AND 50CF-PPS

Epoxy 1096 resin (obtained from FiberGlast Development Corporation) is a low viscosity and thixotropic system.

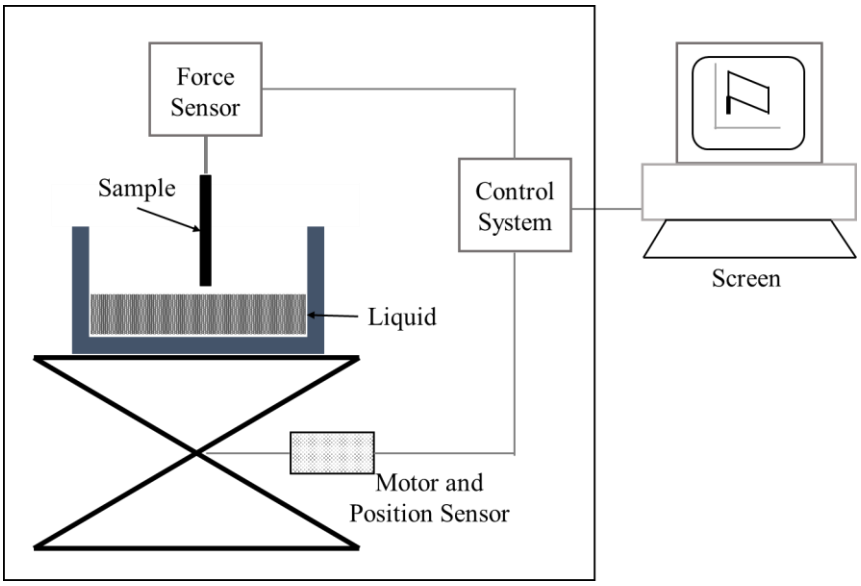

Figure 4.4: Dynamic contact angle measurement set up (adapted from [24]). The specimen immersed (5 mm) into the liquid (water) with constant speed (20 µm/s). The proceeding and receding contact angles were recorded using control system.

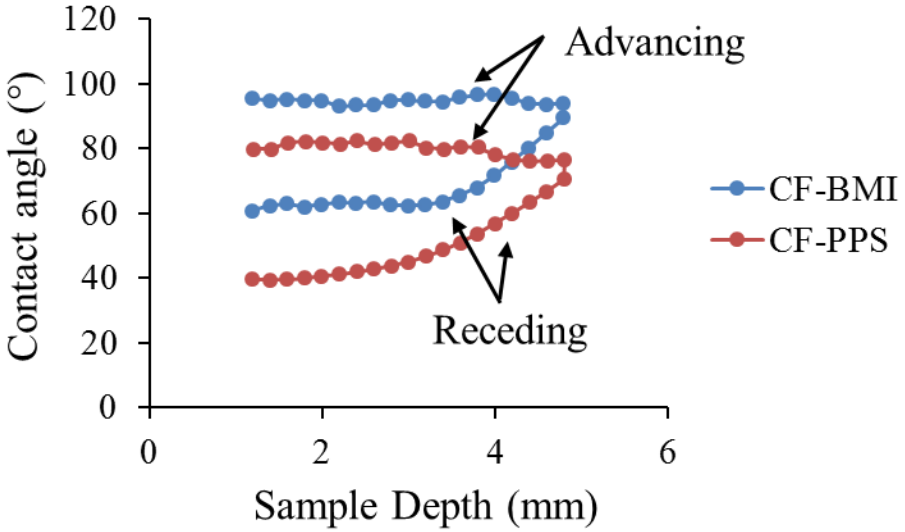

Figure 4.5: Dynamic contact angle plots of CF-BMI prepreg with respect to immersion depth (advancing angle: 95°, receding angle: 63°) and 50CF-PPS (advancing angle: 80°, receding angle: 42°).

The 1096 epoxy system is designed for intermediate/high temperature applications by adding aluminum particles. In this study, a thin layer (0.1 mm) of epoxy 1096 was applied between 50CF-PPS AM and CF-BMI surfaces. The following trials showed the systematic approach to optimize and improve bonding strength between 50CF-PPS and CF-BMI.

1) Baseline: Processing conditions were given in section 4.2.
2) Increased Temperature: The compression molding temperature was increased to 218 °C (425 °F) from 190 °C (375 °F). The rest of the parameters were kept constant. This trial was performed to observe the effect of increased temperature on the bonding characteristics.
3) Dry Epoxy: A 0.1 mm thick layer of 1096 epoxy was applied on the 50CF-PPS AM surface and allowed to cure for 24 hours. The surface was mechanically roughened using 1200 grade sandpaper to increase the surface area. Then, 3 layers of CF-BMI prepreg were attached using baseline processing conditions.
4) Wet Epoxy: A 0.1 mm thick layer of 1096 epoxy was applied on the 50CF-PPS AM surface, and before curing, CF-BMI layers were placed over it according to the processing conditions given in the section 4.2.

It can be observed from Figure 4.3 (a) that the BMI resin did not flow inside the gaps between beads, which limits the bond strength. To increase the flowability of BMI resin, samples were processed at higher temperatures (218 °C) than baseline (190 °C). Higher temperature helped the BMI resin to flow, which can be seen from Figure 4.6 (a). The transverse tensile strength improved by 285% to 2.08 MPa as compared to baseline. Careful observation of failed surface showed that there was no evidence of BMI resin on the surface of beads, representing poor bonding, confirming contact angle analysis.

Therefore, a layer of epoxy 1096 was applied on the AM surface, to act as an adhesive layer between CF-BMI prepreg and 50CF-PPS AM. The process was conducted in two steps: (a) A 0.1 mm thick of 1096 epoxy layer was applied on 50CF-PPS AM surface and allowed it to cure for 24 hours. A sand paper (1200 grade) was used to roughen the surface to increase its surface area [31]. (b) Processing conditions used in section 2 were followed to bond CF-BMI prepreg. This variable is called dry epoxy. In this trial, the bond strength increased (1.71 MPa) in comparison to the baseline (0.54 MPa). The failed specimen of the dry epoxy trial is shown in Figure 4.6 (b). In the dry epoxy experiment, the epoxy was already cured and hence did not contribute effectively increasing the bonding of 50CF-PPS substrate to CF-BMI prepreg.

The next trial was performed such that a thin layer of 1096 epoxy (0.1 mm) was applied to the 50CF-PPS AM surface, and before curing, the CF-BMI prepreg was bonded using baseline processing conditions. Here, both uncured epoxy and BMI resin exhibited good adhesion and resulted in higher bond strength (2.62 MPa) compared to dry epoxy. It can be observed from Figure 4.6 (c), the wet epoxy stayed in the gaps between beads; however, squeezed out from the bead surface after the application of pressure, due to its low viscosity (106,000 cP [32]).

A micro-balloon is a hollow microsphere filler made of low-density thermoplastic polymer. The average size of micro-balloon is less than 70 microns and the ingredients are soda lime borosilicate glass (97-100 % by weight) and synthetic amorphous crystalline free silica (0-3 % by weight) [33]. When the micro-balloons are homogeneously mixed in epoxy, it create a smooth and creamy compound [34]. The creamy compound increase the viscosity of epoxy and improve the debonding energy between the two different/dissimilar materials [35]. In this study, 1096 epoxy was mixed with 40% by weight micro-balloon uniformly and a layer (0.1 mm) of creamy paste was applied on the 50CF-PPS AM surface prior to CF-BMI prepreg bonding. Figure 4.6 (d) showed that a layer

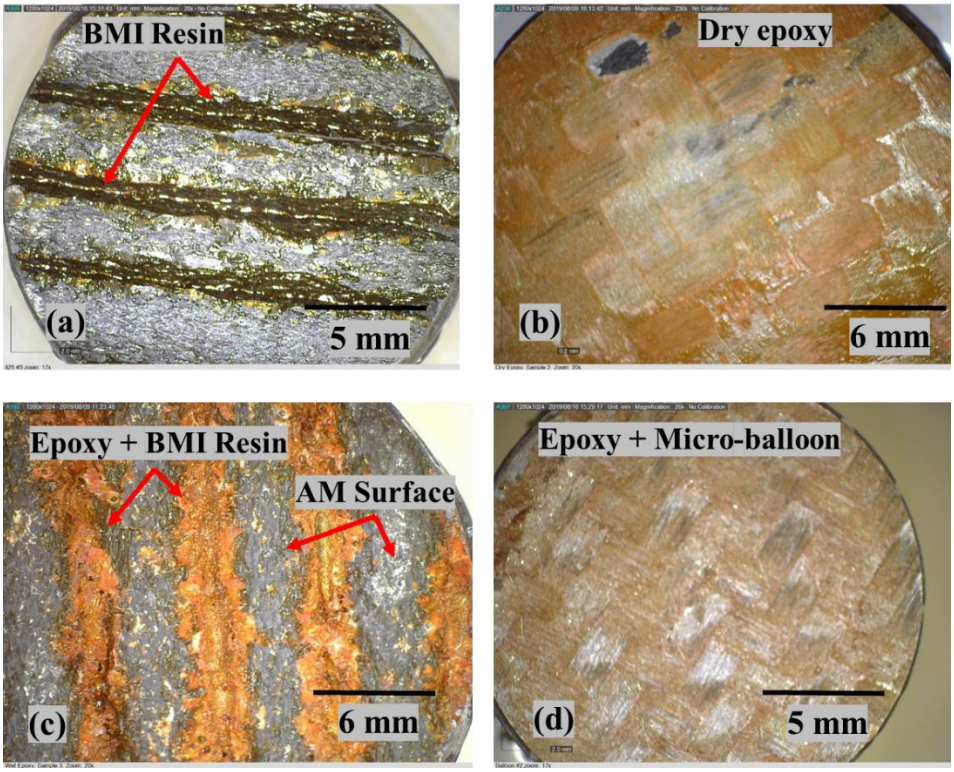

Figure 4.6: Optical microscopic images of failed transverse tensile test specimens (a) increased temperature: BMI resin flowed inside the beads (b) dry epoxy: 0.1 mm thick layer of 1096 epoxy (c) wet epoxy-no filler: 1096 epoxy resin squeezed out from top of the bead due to 552 kPa pressure (d) wet epoxy-micro-balloon fillers: 1096 epoxy did not squeezed out due to increased viscosity

Table 4.2: Summary of transverse tensile strength of 50CF-PPS and CF-BMI bonding optimization trials

Sr. No.	Sample	Transverse tensile strength (MPa)	
		avg	STDEV
1	Baseline	0.54	0.14
2	Increased Temp.	2.08	0.37
3	Dry Epoxy	1.71	0.32
4	Wet epoxy (no filler)	2.62	0.39
5	Wet epoxy (micro-balloon fillers)	4.79	1.84

avg: average; STDEV: standard deviation

of epoxy was present on the entire surface of a failed sample and transverse tensile strength was significantly improved (82.8%) as compared to epoxy when fillers were not added. Table 4.2 shows the summary of transverse tensile strength for all trials.

4.6 AUTOCLAVE BONDING TRIALS

A representative 50CF-PPS substrate mold was printed using BAAM as shown in Figure 4.1, and used without any surface treatment. This mold was to be used for bonding with the CF-BMI prepreg. The autoclave trial was performed according to the processing conditions used for wet epoxy and micro-balloon filler since that configuration resulted in the highest bond strength between the 50CF-PPS AM substrate and the CF-BMI prepreg skin. First, a layer of 1096 epoxy (0.1 mm) and 40% weight micro-balloon filler was applied on the substrate. Three layers of CF-BMI prepreg were placed on the epoxy layer, and then the mold was vacuum bagged. The mold was placed in the autoclave and processed for a two-hour cure cycle at 190 °C (375 °F) temperature and 552 KPa (80 psi) pressure. The stepwise processing of the autoclave trial is given in Figure 4.7.

Figure 4.8 shows the hybrid mold of 50CF-PPS AM surface covered with CF-BMI prepreg after autoclave processing. The CF-BMI prepreg showed good bonding with AM surface and uniform draping at the edges and corners was observed, representing excellent formability of the prepreg. At some locations, lack of proper bonding and/or porosity was noted through nondestructive evaluation - visual and tap testing [36]. This was observed due to non-uniform distribution of the epoxy layer on the AM surface, which can be seen from Figure 4.7-step 2. It was also noted that the top curvature surface had print through of the AM beads, as shown in Figure 4.8. In the autoclave process, the pressure is hydrostatic in nature. This compresses the prepreg layers inside the groove between beads, resulting in print through on the finished part.

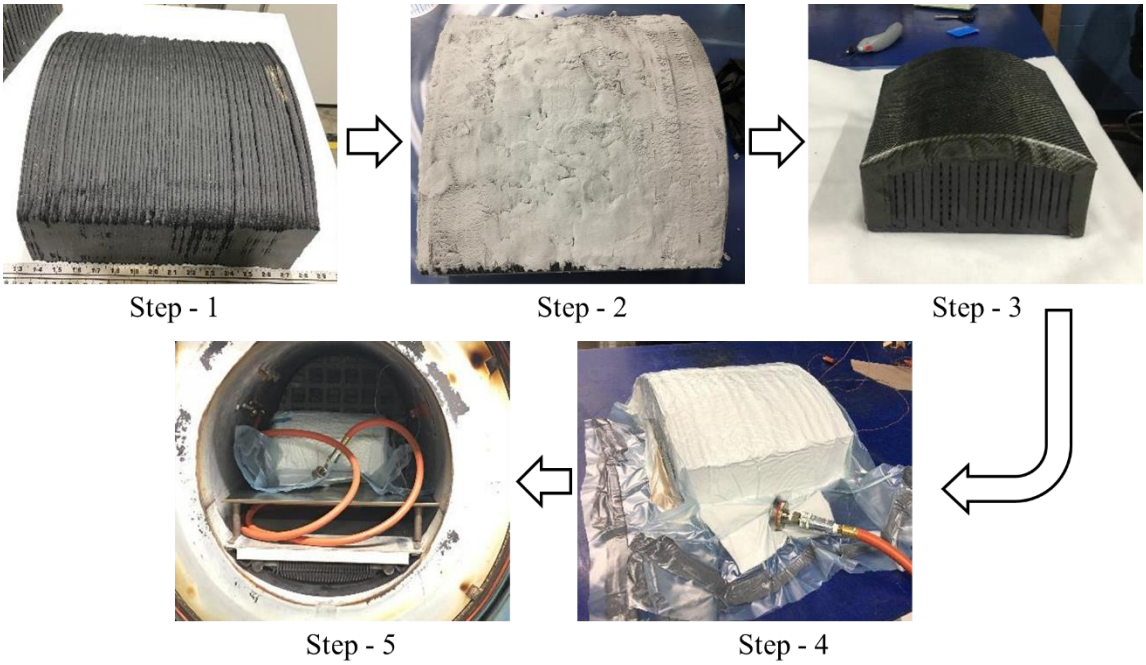

Figure 4.7: Step – 1: 50CF-PPS BAAM substrate; Step – 2: Thin layer (0.1 mm) of 1096 epoxy + 40% micro-balloon applied on substrate; Step – 3: Draping of CF-BMI prepreg on the substrate molding area and sides; Step – 4: Hybrid structure (AM substrate and prepreg) vacuum bagged; Step – 5: Mold plumbed and placed in the autoclave (processing conditions – 190 °C temperature, 552 kPa pressure for 2 hours)

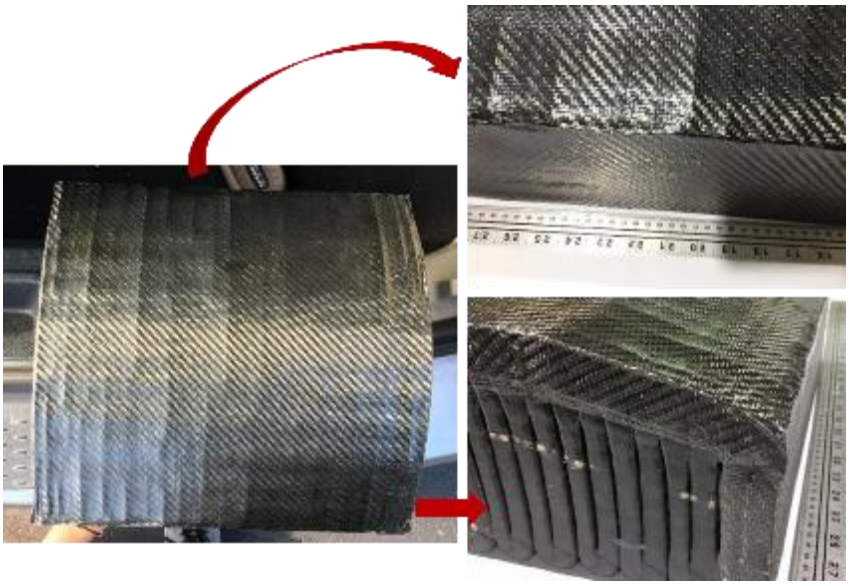

Figure 4.8: Hybrid mold with CF-BMI prepreg after the autoclave trial. The CF-BMI prepreg showed proper draping without any wrinkles. However, the top curvature surface had print through of the beads from the 50CF-PPS BAAM substrate.

4.7 MOLD DEGRADATION EVALUATION

The hybrid mold was used to fabricate woven CF-epoxy parts using hand lay-up. Hand lay-up process is commonly used in marine and corrosion industries [37]. The schematic of hand lay-up process operation is given in Figure 4.9 (a). The mold was first cleaned using acetone and three layers of release agent (Frekote 700-NC) was applied. Three plies of woven CF (Chomarat^{TM} Corporate) wet with Araldite LY 1568 and Aradur 3492 epoxy resin (Huntsman Corporation) (viscosity: 200-300 cPs at room temperature [38]) (from here on this resin will be referred as Huntsman epoxy) were stacked on the mold surface, followed by peel ply, and breather cloth. The assembly was vacuum bagged to remove entrapped air and excess Huntsman epoxy resin. It was noticed that the mold held vacuum very precisely as no air leakage. The part was cured for 24 hours. The representative part is shown in Figure 4.9 (b). The part had glossy surface finish. This process was repeated 7 times to produce 7 parts in order to determine the durability of the mold surface.

High-precision 3D digital impression of the mold was captured using portable FARO Arm equipped with Laser Line Probe (LLP). LLP provides the capability to accurately measure surface structure/form using non-contact 3D scanning. The mold was scanned twice – (1) baseline scan: before manufacturing CF-Huntsman epoxy parts (2) final scan: after fabricating 7 CF-Huntsman epoxy parts. The two scans were aligned, compared and analyzed using Geomagic Control-X 2018 software.

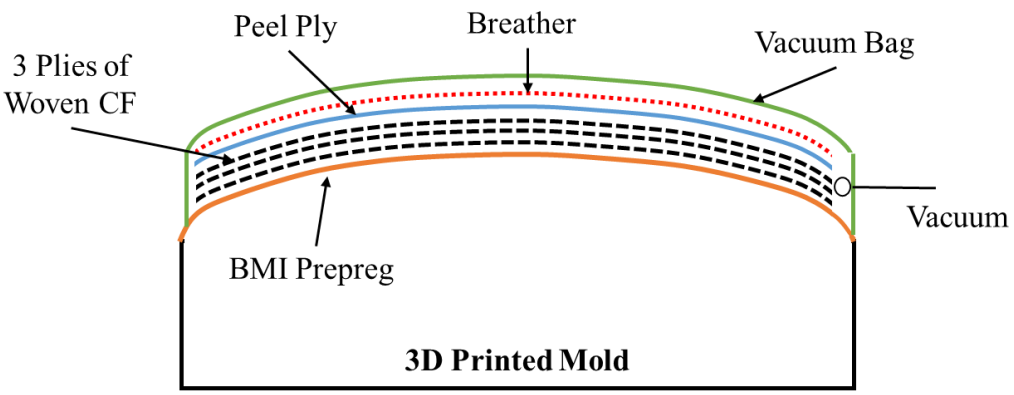

(a)

(b)

Figure 4.9: (a) Schematic of the Hand Lay-up process (b) Representative consolidated CF-huntsman epoxy part

There are two main reasons for the degradation of the mold; (a) friction between the material (fibers, resin) and mold surface when the excess resin is evacuated toward the vacuum port, and (b) exothermic reaction which generates heat during cross-linking (curing). Figure 4.10 shows the analysis of the final scan in comparison with baseline scan for dimensional variation. It was observed that the average deviation was + 0.14 mm / – 0.25 mm (+ 0.005” / - 0.010”) with standard deviation of – 0.18 mm (– 0.007”). Hassen et al. [39] studied effect of the degradation of the 20% weight CF reinforced ABS (20CF-ABS) substrate (manufactured using BAAM system) and standard tooling gel molding surface. The author produced 10 parts of CF-Elium Grade 150 - Arkema composite using vacuum assisted resin transfer molding (VARTM) process and observed + 0.029 mm/ - 0.031 mm degradation. There were several reasons for the higher degradation of CF-BMI mold surface as compared to tooling gel surface as (1) Elium is a thermoplastic resin system; however, Huntsman epoxy is a thermoset resin system. Thermoset resin undergoes crosslinking operation which leads to exothermic heat and viscosity of the Huntsman resin advances up to 100000 cP during gel formation [40]. Elium resin undergoes radical polymerization reaction from methylmethacrylate (MMA) monomer [41]. (2) CF-BMI surface was exposed for longer time (Huntsman epoxy curing time: 24 hours/part) than tooling gel surface (Elium curing time: 2 hours/part). (3) 20CF-ABS BAAM substrate was machined and polished before application of gel coating. This resulted in uniform distribution of coat and easy flow of Elium resin towards vacuum port. CF-BMI prepreg was bonded on the 50CF-PPS BAAM substrate without machining. As observed from Figure 4.7 – Step 2, 1096 epoxy layer was not uniform/smooth. These created resistance (extra friction) for the flow of Huntsman resin towards vacuum port. There are two options to improve the quality of CF-BMI molding surface (i) machining and polishing of 50CF-

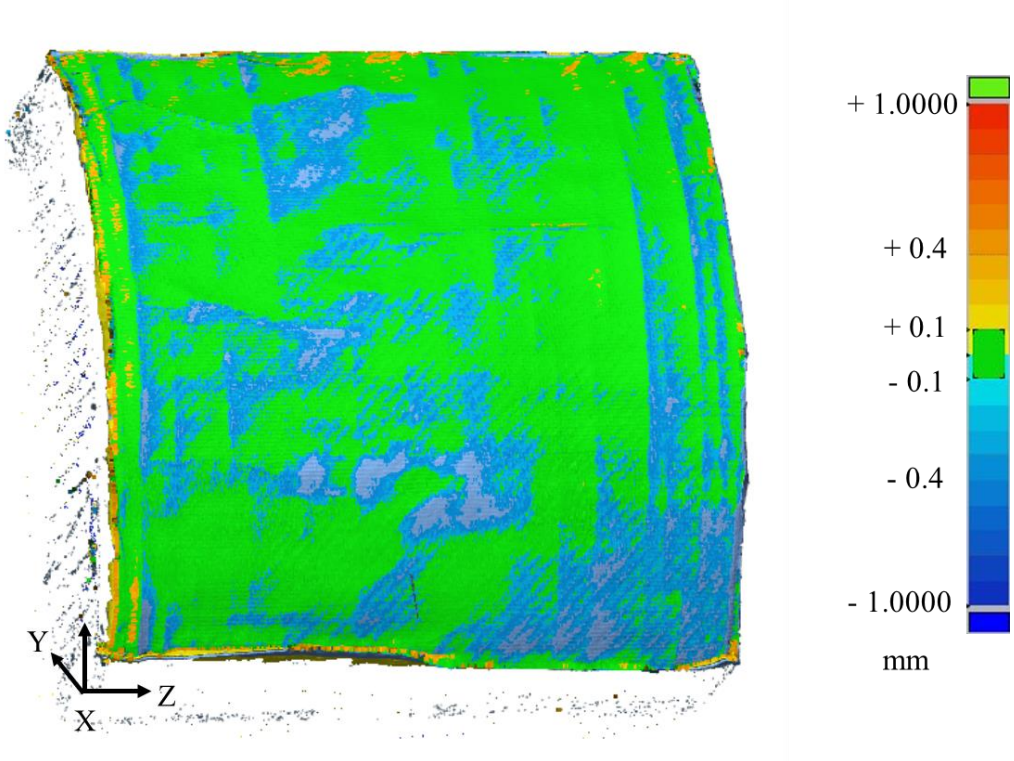

Figure 4.10: Degradation analysis of CF-BMI mold surface after fabrication of 7 hand lay-up parts

PPS substrate, (ii) increase uniformity and thickness of 1096 epoxy layer such that beads structure is completely covered.

From above experiments it can be concluded that the CF-BMI prepreg completely sealed the mold surface without exposing porosity and provided robust surface for composite parts fabrication.

4.8 COST ANALYSIS

The high deposition rate and pellets feedstock material of BAAM system significantly reduces the cost and time of composite mold production [42]. Also, the capability of BAAM to print outside-an-oven significantly reduces the energy intensity (manufacturing energy per kg of product) to 1.1 kW-hr/kg [43]. The mold substrate used in this study weighed 23 kg and the cost of 50CF-PPS was $44/kg (as of year 2020). The preprocessing as slicing the model, setting up the machine was 2 hours and the processing time to print the mold was approximately 2 hours. The post-printing activities as application of 1096 epoxy/micro-balloon layer on mold surface took 2 hours with the average labor cost of $50/hr; however, autoclave processing was conducted for 8 hours with total cost of $1200. The total cost of hybrid mold (CF-BMI skin and 50CF-PPS substrate) fabrication was less than $3000 and breakdown is given in the Table 4.3. Total mold weight and manufacturing time including 3D printing, application of epoxy/ micro-balloon layer and autoclave process, was 24 kg and less than 24 hours, respectively.

The weight of mold would be 210 kg (dimensions: 0.36 m × 0.36 m × 0.20 m and density: 8100 kg/m^3 [6]) if manufactured using Invar. The total cost of the material (Invar) is estimated to be $3780 at an average cost of $18/kg (as of year 2020). Traditional tool manufacturing techniques usually requires few weeks to several months extra amount of time as compared to BAAM to fabricate mold [39]. For a point of comparison, the mold used in this study would require a week

Table 4.3: Cost breakdown of hybrid 50CF-PPS and CF-BMI mold (cost is estimated based on Year 2020 information)

	Time/Material	Cost/unit	Final cost
Preprocessing of the BAAM system	2 hours	$50/hr	$100
50CF-PPS	23 kg	$44/kg	$1012
Mold Printing time	2 hours	$200/hr	$400
1096 Epoxy	0.45 kg	$110/kg	$50
Micro-balloon Fillers	0.2 kg	$55/kg	$11
CF-BMI prepreg	0.45 kg	$165/kg	$74
Application of epoxy and prepreg	2 hours	50/hr	$100
Autoclave Processing	8 hours	$150/hr	$1200
Total	----	----	**$2947**

(170 hours) to manufacture. The total labor cost would be $8500 at an average rate of $50/hr. Therefore, the total cost of the mold would be at least $12,000.

4.9 SUMMARY

A new hybrid mold system of 50CF-PPS substrate and CF-BMI prepreg skin was successfully fabricated and tested. Process optimization was conducted to improve bonding strength of 50CF-PPS and CF-BMI from 0.54 MPa to 4.79 MPa. Fabrication of substrate using BAAM significantly reduced lead time (< 24 hours) and cost (< $3000) of hybrid mold fabrication. The average deviation of + 0.005” / - 0.010” (+ 0.14 mm / – 0.25 mm) was noted after fabricating 7 parts of CF-Huntsman epoxy from hand lay-up process.

REFERENCES

1. Maravola, M., *Low coefficient of thermal expansion composite tooling manufactured via additive manufacturing technologies*. 2018, Youngstown State University.
2. Yeole, P., et al., *Characterization of textile-grade carbon fiber polypropylene composites.* Polymers and Polymer Composites, 2020: p. 0967391120930109.
3. Hausch, G., R. Bächer, and J. Hartmann, *Influence of thermomechanical treatment on the expansion behavior of invar and superinvar.* Physica B: Condensed Matter, 1990. **161**(1-3): p. 22-24.
4. van Schilfgaarde, M., I. Abrikosov, and B.J.N. Johansson, *Origin of the Invar effect in iron–nickel alloys.* 1999. **400**(6739): p. 46.
5. Jasthi, B.K., et al., *Thermal expansion coefficient and mechanical properties of friction stir welded invar (Fe-36% Ni).* 2009. **18**(7): p. 925-934.
6. Li, X.C., et al., *Mechanical and thermal expansion behavior of laser deposited metal matrix composites of Invar and TiC.* 2000. **282**(1-2): p. 86-90.
7. Stewart, R.J.r.p., *New mould technologies and tooling materials promise advances for composites.* 2010. **54**(3): p. 30-36.
8. Kunc, V., et al. *Investigation of in-autoclave additive manufacturing composite tooling*. in *CAMX Conference, Anaheim, CA*. 2016.
9. Hassen, A.A., et al. *Additive manufacturing of composite tooling using high temperature thermoplastic materials*. in *SAMPE Conference Proceedings, Long Beach, CA, May*. 2016.
10. Duty, C.E., T. Drye, and A. Franc, *Material development for tooling applications using big area additive manufacturing (BAAM)*. 2015, Oak Ridge National Lab.(ORNL), Oak Ridge, TN (United States). Manufacturing ….

11. Love, L.J., et al., *Feasibility of Using Additive Manufacturing to Produce Automotive Tooling*. 2018, Oak Ridge National Lab.(ORNL), Oak Ridge, TN (United States).

12. Kunc, V., et al. *Large Scale Additively Manufactured Tooling For Composites*. in *15th JAPAN International SAMPE Symposium and Exhibition. Japan*. 2017.

13. Ajinjeru, C., et al. *The influence of rheology on melt processing conditions of amorphous thermoplastics for big area additive manufacturing (BAAM)*. in *27th Annual International Solid Freeform Fabrication Symposium, Austin, TX*. 2016.

14. Kim, P., et al., *Analysis on Part Distortion and Residual Stress in Big Area Additive Manufacturing with Carbon Fiber-Reinforced Thermoplastic using Dehomogenization Technique*. 2019, Oak Ridge National Lab.(ORNL), Oak Ridge, TN (United States).

15. Seokpum Kim, P.Y., Ahmed Hassen, Vipin Kumar, Vlastimil Kunc, Uday Vaidya, *Effect of Infill Patterns on Heating for Additively Manufactured Compression Molds*, in *SAMPE Conference Proceeding*. 2020: Seattle, WA.

16. Yeole, P., et al., *Mechanical Characterization of High-Temperature Carbon Fiber-Polyphenylene Sulfide Composites for Large Area Extrusion Deposition Additive Manufacturing.* Additive Manufacturing, 2020: p. 101255.

17. Engwall, D.L., et al., *Hybrid lay-up tool*. 2001, Google Patents.

18. *Tooling*, in *CompositesWorld*. 3/23/2016.

19. Li, N., et al., *A comparative experiment for the analysis of microwave and thermal process induced strains of carbon fiber/bismaleimide composite materials.* 2015. **106**: p. 15-19.

20. Kumar, V., et al., *Replacing Metal-Based Lightning Strike Protection Layer of CFRPS by 3D Printed Electronically Conductive Polymer Layer*. 2019, Oak Ridge National Lab.(ORNL), Oak Ridge, TN (United States).

21. Iredale, R.J., C. Ward, and I.J.P.i.P.S. Hamerton, *Modern advances in bismaleimide resin technology: a 21st century perspective on the chemistry of addition polyimides.* 2017. **69**: p. 1-21.

22. Yeole, P., *Fiber metal laminate with thickness reinforcement*. 2015, The University of Alabama at Birmingham.

23. Sangnal Matt Durandhara Murthy, V., *Improving the Adhesion of Glass/Polypropylene (Glass/PP) and High-Density Polyethylene (HDPE) Surfaces by Open Air Plasma Treatment.* 2017.

24. Hefer, A.W., A. Bhasin, and D.N. Little, *Bitumen surface energy characterization using a contact angle approach.* Journal of Materials in Civil Engineering, 2006. **18**(6): p. 759-767.

25. Kwok, D.Y. and A.W. Neumann, *Contact angle measurement and contact angle interpretation.* Advances in colloid and interface science, 1999. **81**(3): p. 167-249.

26. Van Oss, C., *Interfacial forces in aqueous media. 1994.* New York: Marcel Decker Inc, 2005.

27. Della Volpe, C. and S. Siboni, *Some reflections on acid–base solid surface free energy theories.* Journal of Colloid and Interface Science, 1997. **195**(1): p. 121-136.

28. Lam, C., et al., *Study of the advancing and receding contact angles: liquid sorption as a cause of contact angle hysteresis.* Advances in colloid and interface science, 2002. **96**(1-3): p. 169-191.

29. Murthy, V.S.M.D. and U. Vaidya, *Improving the adhesion of glass/polypropylene (glass-PP) and high-density polyethylene (HDPE) surfaces by open air plasma treatment.* International Journal of Adhesion and Adhesives, 2019. **95**: p. 102435.

30. Morrison, J.A. and G.B. Merrill, *Methodology and tooling arrangements for strengthening a surface bond in a hybrid ceramic matrix composite structure*. 2010, Google Patents.

31. Yeole, P., H. Ning, and A.A. Hassen, *Development and characterization of a polypropylene matrix composite and aluminum hybrid material.* Journal of Thermoplastic Composite Materials, 2019: p. 0892705719843974.

32. Corpration, F.D., *1096 High Temp Epoxy Surface Coat*.

33. *Glass Microspheres*, F.G.D. Corporation, Editor.

34. Uddin, N. and U.J.J.o.C.f.C. Vaidya, *Ballistic testing of polymer composites to manufacture emergency safe house shelters.* 2005. **9**(4): p. 369-375.

35. Uddin, N. and U. Vaidya, *Ballistic testing of polymer composites to manufacture emergency safe house shelters.* Journal of Composites for Construction, 2005. **9**(4): p. 369-375.

36. Bossi, R. and V. Giurgiutiu, *Nondestructive testing of damage in aerospace composites*, in *Polymer Composites in the Aerospace Industry*. 2015, Elsevier. p. 413-448.

37. Jamir, M.R., M.S. Majid, and A. Khasri, *Natural lightweight hybrid composites for aircraft structural applications*, in *Sustainable Composites for Aerospace Applications*. 2018, Elsevier. p. 155-170.

38. Airtech's Dahlpac, M., *Show preview: COMPOSITES EUROPE 2012.* 2012.

39. Hassen, A.A., et al., *The durability of large-scale additive manufacturing composite molds.* CAMX 2016, 2016: p. 26-29.

40. Macosko, C.W., *Rheological changes during crosslinking.* British polymer journal, 1985. **17**(2): p. 239-245.

41. Kazemi, M., et al., *Mechanical properties and failure modes of hybrid fiber reinforced polymer composites with a novel liquid thermoplastic resin, Elium®*. Composites Part A: Applied Science and Manufacturing, 2019. **125**: p. 105523.

42. Kunc, V., et al. *Large Scale Additively Manufactured Tooling For Composites*. in *Proceedings of 15th Japan International SAMPE Symposium and Exhibition*. 2017.

43. Post, B., et al. *The economics of big area additive manufacturing*. in *Proceedings of the 27th Annual International Solid Freeform Fabrication Symposium, Austin, TX, USA*. 2016.

VITA

Pritesh Yeole was born in India. He obtained his Bachelor of Technology degree in Metallurgical Engineering from College of Engineering, Pune, India in 2011. Upon completion of his undergraduate studies, Pritesh moved to the United States of America to pursue a Master of Science degree in Materials Science and Engineering at University of Alabama at Birmingham. With the goal of pursing a PhD degree, Pritesh joined the Mechanical, Aerospace and Biomedical Engineering Department at the University of Tennessee, Knoxville in August 2015. He joined Dr. Uday Vaidya's group to conduct research in the area of advanced composites, in collaboration with IACMI – the Composites Institute and the Manufacturing Demonstration Facility (MDF) at Oak Ridge National Laboratory. Pritesh's primary research focus has been on the assessment of additively manufactured composite molds.